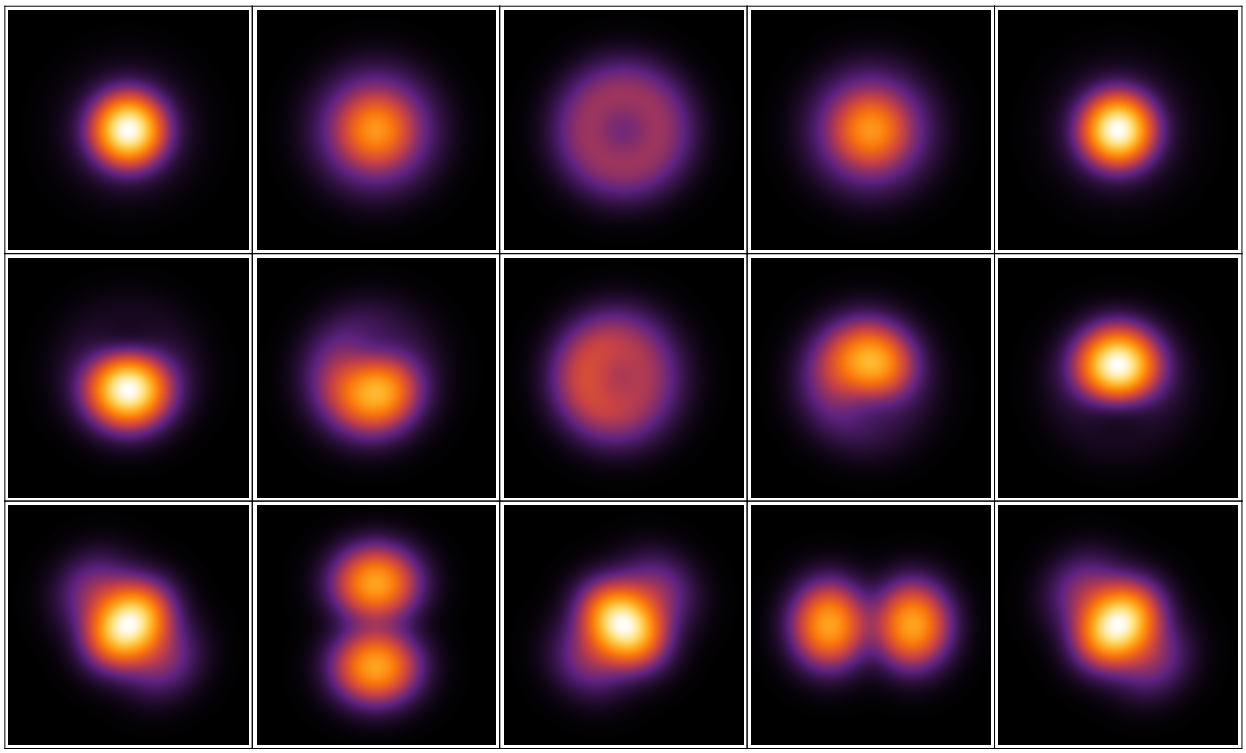

Rotating Two-Dimensional Mesoscopic Fermi Gases and Nonrelativistic Conformal Invariance

Master's thesis in Physics

VIKTOR BEKASSY

DEPARTMENT OF PHYSICS

CHALMERS UNIVERSITY OF TECHNOLOGY
Gothenburg, Sweden 2023
www.chalmers.se

Master's thesis 2023

Rotating Two-Dimensional Mesoscopic Fermi Gases and Nonrelativistic Conformal Invariance

VIKTOR BEKASSY

CHALMERS
UNIVERSITY OF TECHNOLOGY

Department of Physics
Chalmers University of Technology
Gothenburg, Sweden 2023

Rotating Two-Dimensional Mesoscopic Fermi Gases and
Nonrelativistic Conformal Invariance
VIKTOR BEKASSY

© VIKTOR BEKASSY, 2023.

Supervisor: Johannes Hofmann, Department of Physics
Examiner: Johannes Hofmann, Department of Physics

Master's Thesis 2023
Department of Physics
Chalmers University of Technology
SE-412 96 Gothenburg
Telephone +46 31 772 1000

Cover: A visualization of the Fermi gas density for two particles. Time runs horizontally and different rows correspond to different superposition of states.

Typeset in LaTeX
Printed by Chalmers Reproservice
Gothenburg, Sweden 2023

Rotating Two-Dimensional Mesoscopic Fermi Gases and
Nonrelativistic Conformal Invariance
VIKTOR BEKASSY
Department of Physics
Chalmers University of Technology

Abstract

Experiments on ultracold atoms offer the exciting possibility of probing quantum gases with exceptional accuracy based on recently developed techniques. Interactions are tunable, and the effective dimensionality of the gas is adjustable, hence making the ability to prepare these cold quantum gases an appealing opportunity to test theoretical predictions. This thesis presents the consequences of a joint scale and conformal invariance in rotating mesoscopic two-dimensional Fermi gases at weak interactions; a previously overlooked system since quantum anomaly was assumed to break scale and conformal invariance. With degenerate perturbation theory, the energy spectrum for mesoscopic particle ensemble is computed, thus providing concrete evidence for the conformal tower structure of a nonrelativistic conformally invariant interacting system. Furthermore, the conformal symmetry predicts the hyperradial distribution function of the many-body wave functions in a closed analytical form, which has been confirmed using Metropolis Monte Carlo sampling. We argue that our results could directly be testable with current experiments on mesoscopic Fermi gases.

Keywords: Two-dimensional mesoscopic Fermi gases, nonrelativistic conformal invariance, many-body quantum mechanics.

Acknowledgements

I would like to express my gratitude to the supervisor and examiner of this thesis, Johannes, not only for his great support and guidance throughout the project but also for making the project possible.

Viktor Bekassy, Gothenburg, June 2023

Contents

1

Introduction

In physics, symmetries and conservation laws are important concepts. Some familiar examples are invariance under time translations, which imply the conservation of energy, or invariance under space translation, which imply the conservation of momentum. The two examples mentioned above are examples of continuous symmetries with conservation laws that follow from the Noether theorem [1]. Another familiar example of symmetries is found in solids where atoms arrange themselves in a periodic manner forming a crystal with discrete symmetry [2].

In condensed matter physics, an important symmetry is scale invariance, which arises for example near a second-order phase transition [3, 4]. However, scale invariance can exist in certain interacting many-body systems without being close to a transition point. A famous example is the unitary Fermi gas in atomic physics, which is so strongly interacting (diverging scattering length) that details of the interaction drop out [5, 6]. Hence, rescaling of time and position coordinates by $(t, \mathbf{r}) \to (\lambda^2 t, \lambda \mathbf{r})$ changes the Hamiltonian $H \to H/\lambda^2$ and leaves the Schrödinger equation and the action invariant. The consequences are for example a homogeneous equation of state [7, 8] and a vanishing bulk viscosity [9, 10].

As is discussed in this thesis, another example where scale invariance is present is the two-dimensional interacting Fermi gases, realized experimentally with ultracold atoms [11–13]. Interactions in ultracold atoms are modeled by a delta function, which upon a rescaling of position coordinates changes as $\delta^{(d)}(\lambda \mathbf{r}) \to \lambda^{-d} \delta^{(d)}(\mathbf{r})$ [14]. Thus, at first sight, a special situation arises in two dimensions $d = 2$ because the interaction scales in the same way as the kinetic energy $H_{\text{kin}} \to H_{\text{kin}}/\lambda^2$. Even in a harmonic trap that explicitly breaks scale invariance, $H_{\text{trap}} \to \lambda^2 H_{\text{trap}}$, the properties of the gas are still constrained. The reason is that scale invariance implies an additional symmetry under special conformal transformations $(t, \mathbf{r}) \to (t, \mathbf{r})/(1+\lambda t)$ and the generator of the transformation takes the same form as the harmonic potential [15, 16].

The Hamiltonian is thus part of a nonrelativistic symmetry algebra which is investigated and explored in this thesis. The symmetry implies a one-to-one correspondence between free-space eigenstates at zero energy and certain states in a harmonic trap called primary states [5, 17]. These primary states are the foundation of conformal energy towers which are obtained by center-of-mass and breathing mode excitations, the latter having an excitation energy of exactly twice the harmonic oscillator energy. This means that if one knows the primary states of the

theory, the entire energy spectrum is known. Furthermore, the microscopic origin of the nonrelativistic symmetry is a factorization of the many-body wave function [5, 6]. The symmetry predicts a hyperradial distribution of the many-body wave function in closed analytical form.

However, the story of interactions in two-dimensional interacting Fermi gases is slightly more complicated. A delta function interaction in dimension $d > 1$ actually requires renormalization which depends on an additional energy scale that breaks scale and conformal invariance in two dimensions. This is an example of a quantum anomaly, where a classical symmetry is broken in the corresponding quantum theory [18, 19]. The literature on the subject has indeed been focused on how the conformal invariance is subtly broken by quantum anomaly at stronger interaction [20–28]. However, as was argued by the author and the supervisor of this thesis in a previous work on two-dimensional interacting Fermi gases [29], a conformal window still exists at weak interactions where scaling violations are negligible [14, 30].

In this thesis, it is shown that rotating two-dimensional Fermi gases at weak interactions also possess a nonrelativistic conformal invariance. The rotation gives rise classically to a Coriolis force yielding a Hamiltonian that is equivalent to the Lorentz force of a charged particle in a uniform magnetic field, resembling the physics of the quantum Hall effect. With exact diagonalization and many-body degenerate perturbation theory, a protocol to detect the primary states and reveal their conformal tower structure in the energy spectrum for mesoscopic particle ensembles in a rotating trap is established. Furthermore, the hyperradial distribution of the many-body wave function is computed and confirmed with Monte Carlo simulations. We argue that the results of this thesis are testable experimentally in ultracold atomic gases by sampling the many-body wave function with recently developed single-particle imaging techniques [12, 13, 31].

The ultracold atomic gases modeled in this thesis consist of electrically neutral atoms trapped by lasers [11–13]. The electric fields of the lasers induce dipoles in the atoms, consequently attracting the atoms to the laser focus where the field is strongest. Since displacement away from the focus is small, the potential is modeled as a harmonic trap. Furthermore, these are quantum gases, meaning that the size of the wave functions estimated by the de Broglie wavelength is comparable to the interparticle distance [14]. What makes ultracold atomic gases Fermi gases is that they are composed of fermions that adhere to the Pauli principle. Experimentally, two hyperfine states of ^{6}Li atoms, which are composite fermionic, are commonly trapped [11–13]. These hyperfine states are treated as spin components $\sigma = \uparrow, \downarrow$, and the thesis considers N-particle configurations with an equal number of both spin components for even N, and one excess spin for odd N.

The thesis is structured as follows: First, in Sec. 2.1 and 2.2, the theoretical framework of single-particle and fermionic many-body quantum mechanics is established respectively. Second, in Sec. 2.3, interactions in ultracold atomic gases are described and the conformal window is motivated. Next, in Sec. 2.4 the nonrelativistic con-

formal symmetry algebra is discussed and the primary states and the conformal towers are introduced. Furthermore, in Sec. 2.5, the separation of the many-body wave function and the hyperradial distribution is discussed. Then, in Sec. 2.6 and 2.7 we discuss how one can observe and excite center-of-mass and breathing mode excitations. Having discussed the necessary theory in Ch. 2, the protocol to detect primary states and their conformal towers with exact diagonalization is described in Sec. 3.1 and 3.2. The Monte Carlo simulations of the many-body wave function are described in Sec. 3.3 before the results in Ch. 4.

2

Theory

The framework used in this thesis to discuss nonrelativistic conformal invariance in rotating mesoscopic Fermi gases is many-body quantum mechanics. For this purpose, the theory section starts by introducing single-particle quantum mechanics - the building block of many-body quantum mechanics. First, the two-dimensional harmonic oscillator is introduced in Sec. 2.1.1. The effect of rotating the gas is consecutively discussed in Sec. 2.1.2. Rotation gives rise to a Coriolis force which is mathematically equivalent to the Lorentz force of a charged in a magnetic field, hence analogous to quantum hall physics. Second, the language of fermionic many-body theory is introduced in Sec. 2.2. Then, interactions in Fermi gases are discussed in Sec. 2.3, from which the full interacting many-body Hamiltonian is introduced in Sec. 2.3.2.

Having familiarized ourselves with fermionic many-body theory, Sec. 2.4 then discusses the nonrelativistic symmetry algebra. The nonrelativistic symmetry predicts primary states and their conformal towers, which are discussed in Sec. 2.4.4. Further, the microscopic origin of the symmetry is a separation in the many-body wavefunction which is discussed in Sec. 2.5. There, the hyperradial distribution predicted in closed analytical form by the symmetry is introduced.

The theory section then discusses how breathing mode and center-of-mass excitations can be visualized in the density of the gas in Sec. 2.6. Last, in order to observe such excitations, one must excite the gas by perturbing the system in different ways. This is discussed in Sec. 2.7.

2.1 Single-Particle Quantum Mechanics

The time evolution of a quantum-mechanical state in the Schrödinger picture is determined by the Schrödinger equation

$$i\hbar\frac{d}{dt}|\psi(t)\rangle = H|\psi(t)\rangle, \tag{2.1}$$

where H is the Hamiltonian of the system and $|\psi(t)\rangle$ is a general vector in a Hilbert space [32]. For a time-independent Hamiltonian, the formal solution to the Schrödinger equation is

$$|\psi(t)\rangle = e^{-iHt/\hbar}|\psi(0)\rangle. \tag{2.2}$$

However, one can expand a general state in terms of the eigenstates of the Hamiltonian, obtained from the solution of the stationary Schrödinger equation $H|\psi_n\rangle = \varepsilon_n|\psi_n\rangle$. Assuming a discrete energy spectrum, equation (2.2) takes the form

$$|\psi(t)\rangle = \sum_n e^{-i\varepsilon_n t/\hbar}|\psi_n\rangle, \tag{2.3}$$

where the summation starts at the lowest energy eigenstate, i.e. the ground state.

2.1.1 The Two-Dimensional Harmonic Oscillator

The single-particle Hamiltonian of the two-dimensional (2D) quantum harmonic oscillator takes the form

$$H = \frac{p^2}{2\mathcal{M}} + \frac{1}{2}\mathcal{M}\omega^2(x^2+y^2) = -\frac{\hbar^2}{2\mathcal{M}}\left(\frac{\partial^2}{\partial x^2} + \frac{\partial^2}{\partial y^2}\right) + \frac{1}{2}\mathcal{M}\omega^2(x^2+y^2), \tag{2.4}$$

where $\mathcal{M}$ is the particle mass and ω the characteristic angular frequency of the oscillator. Because the harmonic trap only depends on the distance away from the trap center and is radially symmetric, it is convenient to work in polar coordinates

$$H = \frac{p^2}{2\mathcal{M}} + \frac{1}{2}\mathcal{M}\omega^2 r^2 = -\frac{\hbar^2}{2\mathcal{M}}\left(\frac{1}{r}\frac{\partial}{\partial r}r\frac{\partial}{\partial r} + \frac{1}{r^2}\frac{\partial^2}{\partial\varphi^2}\right) + \frac{1}{2}\mathcal{M}\omega^2 r^2, \tag{2.5}$$

where $r = \sqrt{x^2+y^2}$ is the distance away from the trap center and $\varphi = \arctan(y/x)$ the angle measured from the x-axis. Solving the stationary Schrödinger equation gives single-particle energy eigenstates $\{|\psi_{n,m}\rangle\}$ parametrized by two quantum numbers n ($n \in \mathbb{N}_0$) and m ($m \in \mathbb{Z}$), with energy

$$\varepsilon_{n,m} = \hbar\omega(2n + |m| + 1), \tag{2.6}$$

and position-space projection

$$\langle \mathbf{r}|\psi_{n,m}\rangle = \psi_{n,m}(r,\varphi) = \frac{1}{\ell_{ho}} \cdot \sqrt{\frac{n!}{(n+|m|)!\pi}} \left(\frac{r}{\ell_{ho}}\right)^{|m|} e^{-\frac{1}{2}(r/\ell_{ho})^2} L_n^{|m|}\left(r^2/\ell_{ho}^2\right) e^{im\varphi}, \tag{2.7}$$

where $\ell_{ho} = \sqrt{\hbar/\mathcal{M}\omega}$ is the characteristic oscillator length, and $L_n^m(x)$ a generalized Laguerre polynomial. In this basis, the energy eigenstates are simultaneous eigenstates of the out-of-plane angular momentum operator $L_z = xp_y - yp_x = -i\hbar\partial/\partial\varphi$ with eigenvalue m. Note that the l^{th} single-particle energy level is $(l+1)$-fold degenerate with angular momentum $m = -l, -l+2, ..., l$.

2.1.2 The Rotating 2D Harmonic Oscillator

By rotating the trap around the z-axis (out-of-plane direction) with a frequency Ω (>0), the Hamiltonian in the rotating frame changes from Eq. (2.4) of the two-dimensional harmonic oscillator to

$$H \to H - \Omega L_z = \frac{p^2}{2\mathcal{M}} + \frac{1}{2}\mathcal{M}\omega^2 r^2 - \Omega L_z, \tag{2.8}$$

where $L_z = xp_y - yp_x = -i\hbar\partial/\partial\varphi$ is the out-of-plane angular momentum operator. That this Hamiltonian produces the correct equations of motion can be checked in the Heisenberg picture, where operators have time dependence

$$\frac{dA}{dt} = \frac{1}{i\hbar}[A, H], \tag{2.9}$$

where A is assumed to not have any explicit time-dependence in the Schrödinger picture and H is given in Eq. (2.8). Using Heisenberg's equation of motion in Eq. (2.9) for the position $\mathbf{r} = (x, y)$ in the rotating frame with rotation $\boldsymbol{\Omega} = \Omega\hat{\mathbf{z}}$ gives

$$\frac{d\mathbf{r}}{dt} = \frac{1}{i\hbar}[\mathbf{r}, H] = \frac{\mathbf{p}}{\mathcal{M}} - \boldsymbol{\Omega} \times \mathbf{r} = \mathbf{v}, \tag{2.10}$$

where $\mathbf{p} = (p_x, p_y)$, $\mathbf{v} = (v_x, v_y)$ are momentum and velocity respectively in the rotating frame. Similarly using Eq. (2.9) for the momentum $\mathbf{p}$ yields

$$\frac{d\mathbf{p}}{dt} = \frac{1}{i\hbar}[\mathbf{p}, H] = -\mathcal{M}\omega^2\mathbf{r} - \boldsymbol{\Omega} \times \mathbf{p} = \mathbf{F} - \boldsymbol{\Omega} \times \mathbf{p}, \tag{2.11}$$

where the trapping force $\mathbf{F} = -\mathcal{M}\omega^2\mathbf{r}$ has been introduced. Now defining the acceleration in the rotating frame as $\mathbf{a} = d\mathbf{v}/dt$ and using Eqs. (2.10), (2.11) gives

$$\begin{aligned} \mathbf{a} = \frac{d\mathbf{v}}{dt} &= \frac{1}{\mathcal{M}}\frac{d\mathbf{p}}{dt} - \boldsymbol{\Omega} \times \frac{d\mathbf{r}}{dt} = \frac{1}{\mathcal{M}}\left(\mathbf{F} - \boldsymbol{\Omega} \times \mathbf{p}\right) - \boldsymbol{\Omega} \times \mathbf{v} \\ &= \frac{\mathbf{F}}{\mathcal{M}} - \frac{1}{\mathcal{M}}\boldsymbol{\Omega} \times (\mathcal{M}\mathbf{v} + \mathcal{M}\boldsymbol{\Omega} \times \mathbf{r}) - \boldsymbol{\Omega} \times \mathbf{v} \\ &= \frac{\mathbf{F}}{\mathcal{M}} - 2\boldsymbol{\Omega} \times \mathbf{v} - \boldsymbol{\Omega} \times (\boldsymbol{\Omega} \times \mathbf{r}). \end{aligned} \tag{2.12}$$

This is indeed the equation of motion of an object with mass $\mathcal{M}$ in a rotating frame of reference with constant rotation frequency $\boldsymbol{\Omega} = \Omega\hat{\mathbf{z}}$ and where $\mathbf{r}, \mathbf{v}$ are measured relative to the rotating frame. We can recognize the Coriolis force $-2\mathcal{M}\boldsymbol{\Omega} \times \mathbf{v}$, and the centrifugal force $-\mathcal{M}\boldsymbol{\Omega} \times (\boldsymbol{\Omega} \times \mathbf{r}) = \mathcal{M}\Omega^2\mathbf{r}$ pushing the object outwards.

Now, since the eigenstates of the two-dimensional harmonic oscillator in Eq. (2.7) are eigenstates of the angular momentum operator as well, these wave functions can be used as a basis of the rotating harmonic trap. However, the single-particle energy levels change and become

$$\epsilon_{n,m} = \hbar\omega(2n + |m| + 1) - \hbar\Omega m. \tag{2.13}$$

This means that single-particle energy levels with (negative) positive angular momentum m, i.e. angular momentum in the (opposite) direction of rotation, are (raised) lowered in energy. The degeneracy of the single-particle energy levels is lifted by rotation, except for $\Omega/\omega = j/k$ with $j, k \in \mathbb{N}$, for which new degeneracies emerge. Figure 2.1 shows the evolution of single-particle energies as the rotation frequency is increased. However, note that if $\Omega > \omega$ the spectrum would not be bounded from below since states with successively higher m would keep lowering

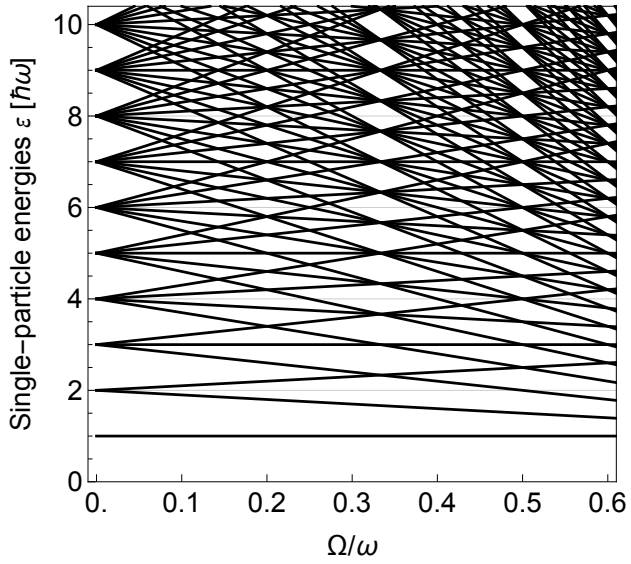

Figure 2.1: Single-particle energies $\varepsilon_{n,m} = \hbar\omega(2n + |m| + 1) - \hbar\Omega m$ as a function of rotation frequency Ω. The degeneracy without rotation, where the l^{th} level is $(l + 1)$-fold degenerate, is split and new degeneracies emerge for $\Omega/\omega = j/k$ with $j, k \in \mathbb{N}$.

the energy. To see this, it is instructive to rewrite the Hamiltonian in Eq. (2.8) in terms of a vector potential $\mathbf{A} = \mathcal{M}\boldsymbol{\Omega} \times \mathbf{r}$ as

$$H = \frac{p^2}{2\mathcal{M}} + \frac{1}{2}\mathcal{M}\omega^2 r^2 - \Omega L_z = \frac{(\mathbf{p} - \mathbf{A})^2}{2\mathcal{M}} + \frac{1}{2}\mathcal{M}(\omega^2 - \Omega^2)r^2, \tag{2.14}$$

where the physical interpretation of $\Omega > \omega$ becomes clear: the centrifugal force $\mathcal{M}\Omega^2 r$ must not exceed the trapping force $-\mathcal{M}\omega^2 r$, resulting in the condition $\Omega \leq \omega$. Furthermore, note that Eq. (2.14) is mathematically equivalent to that of a unit charged ($e = 1$) particle in a uniform magnetic field $\mathbf{B} = 2\mathcal{M}\Omega\hat{\mathbf{z}}$ confined in a trap with spring constant $\mathcal{M}(\omega^2 - \Omega^2)$. This equivalence originates from the mathematical equivalence of the Coriolis force and the Lorentz force of a charged particle in a magnetic field. If $\Omega = \omega$, the particle is no longer confined and the Hamiltonian is that of a free, charged particle in a magnetic field - the starting point in describing the Quantum Hall effect. In this case, the single-particle energy levels are the famous Landau levels which are macroscopically degenerate and illustrated in Fig. 2.2.

2.2 Fermionic Many-Body Quantum Mechanics

In quantum mechanics, identical particles are indistinguishable and the theory of many-body systems must reflect this. This means that for fermions, the many-body wave function $|\Psi\rangle$ is anti-symmetric under the exchange of two identical particles. A consequence of this is the famous Pauli principle, which states that two identical fermions cannot occupy the same quantum-mechanical state simultaneously [32]. Thus, even for a non-interacting system of fermions, their motion will be correlated and they will tend to avoid one another. This can for example be seen in the

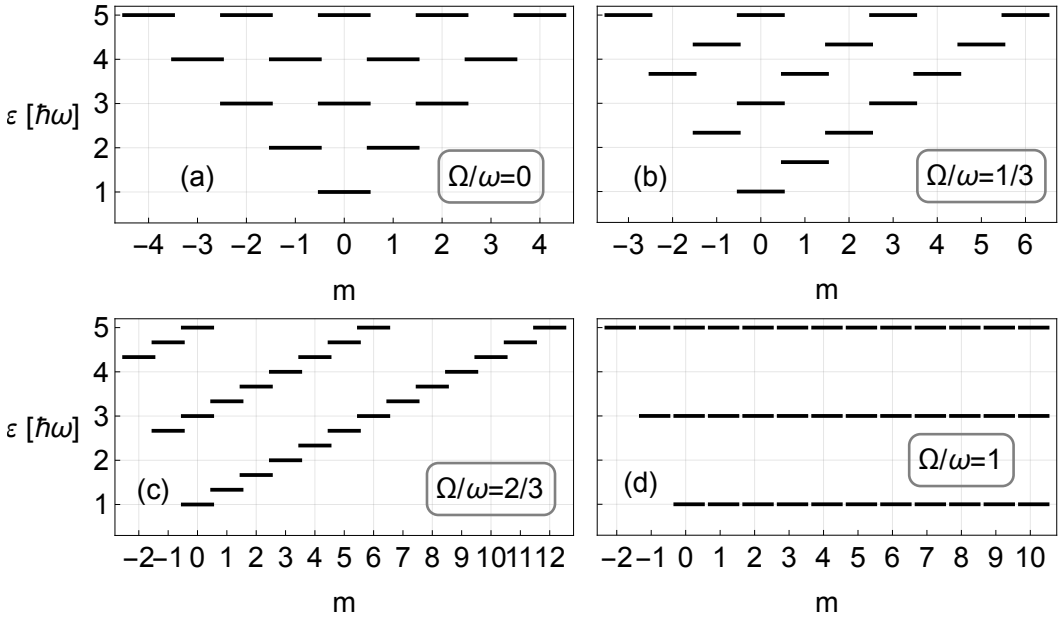

Figure 2.2: (a) Single-particle energy levels of the non-rotating trap. (b), (c) Single-particle energy levels of the rotating trap for rotation frequencies $\Omega/\omega = 1/3$ and $\Omega/\omega = 2/3$ respectively. In (d), the rotation frequency is equal to the trapping frequency and the energy levels become infinitely degenerate, forming Landau levels.

pair correlation function which has a node at the origin in the relative coordinate. Furthermore, as interactions are taken into account fascinating collective phenomena arise, such as superconductivity, the quantum Hall effect, charge density waves in solids, and collective excitations in nuclei, atoms, or molecules.

2.2.1 The Many-body Wave Function

This section seeks to determine the stationary states of many identical fermions through the stationary Schrödinger equation

$$H|\Psi\rangle = E|\Psi\rangle, \tag{2.15}$$

such that eigenstates of the Hamiltonian of the mesoscopic Fermi gas can be determined. For N identical fermions, each fermion is placed in a set of available orthonormal single-particle states, e.g. the eigenstates of the single-particle Hamiltonian $\{|\psi_i\rangle\}$:

$$\langle\psi_j|\psi_k\rangle = \int d^d r\, \psi_j^*(\mathbf{r})\psi_k(\mathbf{r}) \cdot \langle\sigma_j|\sigma_k\rangle = \delta_{jk}\delta_{\sigma_j\sigma_k}, \tag{2.16}$$

where d denotes the spatial dimension and the second factor is the scalar product between spin states (e.g. $\sigma = \pm 1/2$ for electrons) [33]. Because of the Pauli principle, N identical fermions must be placed into N different single-particle states (see Fig. 2.3 for examples of two components) $|\psi_{\lambda_1}\rangle$, $|\psi_{\lambda_2}\rangle$,...,$|\psi_{\lambda_N}\rangle$, and such a many-body state is an example of a so-called Fock-state

$$|\Psi^{\text{Fock}}(\lambda_1, \lambda_2..., \lambda_N)\rangle = |\psi_{\lambda_1}\rangle \otimes |\psi_{\lambda_2}\rangle \cdots \otimes |\psi_{\lambda_N}\rangle, \tag{2.17}$$

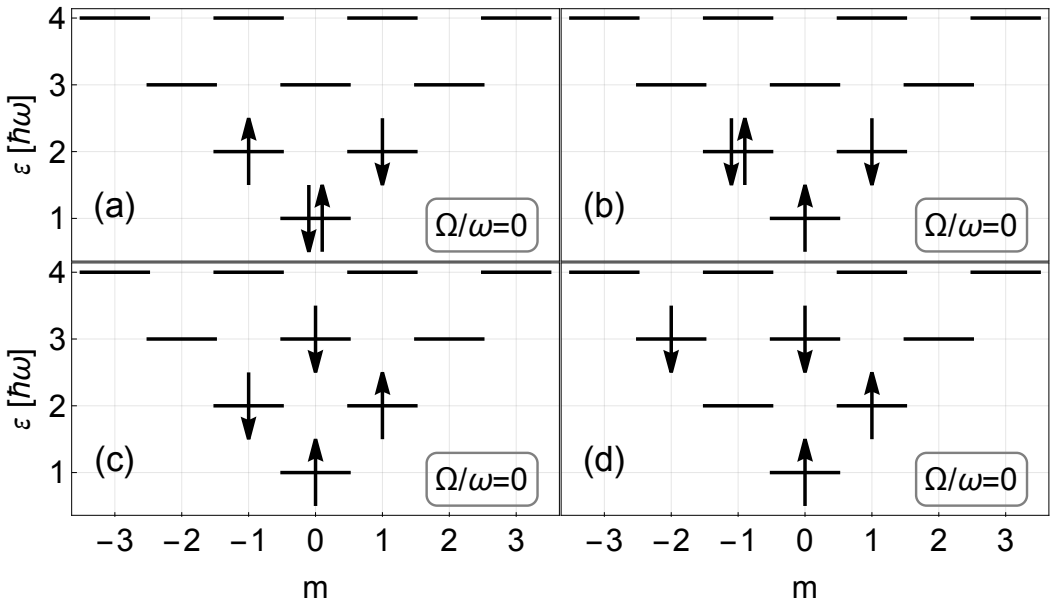

Figure 2.3: (a)-(d) Illustration of placing $N = 4$ fermions in single-particle energy eigenstates $|\psi_{n,m}\rangle$ with energy $\varepsilon_{n,m} = \hbar\omega(2n + |m| + 1)$ for a non-rotating trap. Arrows indicate spin projection $\sigma = \pm 1/2$. The Pauli exclusion principle implies that every single-particle state can at most be occupied once by an arrow pointing in the same direction. In occupation number representation, (a) could be $|1, 1, 1, 0, 0, 1, 0, 0, 0, 0, 0...\rangle$, (b): $|1, 0, 1, 1, 0, 1, 0, 0, 0, 0, 0...\rangle$, (c): $|1, 0, 0, 1, 1, 0, 0, 0, 0, 1, 0...\rangle$, and (d): $|1, 0, 0, 0, 1, 0, 0, 1, 0, 1, 0...\rangle$, where it is important to be consistent with the ordering due to the anti-symmetry requirement. In the examples above the following order was employed, from left: 1) lowest single-particle energy level $\epsilon_{n,m}$ and spin projection $\sigma = +1/2$ followed by $\sigma = -1/2$. 2) For degenerate single-particle energy levels, order according to increasing angular momentum m. Explicitly writing out the first few terms: $(\varepsilon_{0,0} \uparrow), (\varepsilon_{0,0} \downarrow), (\varepsilon_{0,-1} \uparrow), (\varepsilon_{0,-1} \downarrow), (\varepsilon_{0,1} \uparrow), (\varepsilon_{0,1} \downarrow), \ldots$.

with space-spin projection

$$\left\langle \mathbf{x}_1, \mathbf{x}_2, \ldots \mathbf{x}_N | \Psi^{\text{Fock}}(\lambda_1, \lambda_2, \ldots, \lambda_N) \right\rangle = \prod_{j=1}^{N} \psi_{\lambda_j}(\mathbf{x}_j), \tag{2.18}$$

where $\mathbf{x}_j$ is the space-spin coordinate $\mathbf{x}_j = (\mathbf{r}_j, \sigma_j)$ and $\mathbf{r}_j$ and σ_j denote position and spin of particle j. The Fock space describes a quantum many-body system of N indistinguishable particles [33]. However, due to the anti-symmetry requirement, one must consider linear combinations of Fock-states

$$|\Psi(n_1, n_2, \ldots)\rangle = \frac{1}{\sqrt{N!}} \sum_{p \in S_N} \text{sign}(p)\, |\Psi^{\text{Fock}}(\lambda_1, \lambda_2, \ldots \lambda_N)\rangle, \tag{2.19}$$

where the factor $1/\sqrt{N!}$ is there to proper normalize the state, and S_N is the permutation group of N: the set of all permutations of N objects and $\text{sign}(p) = \pm 1$ if the permutation p is even or odd. Integers n_i denote the number of times a single-particle state $|\psi_i\rangle$ is occupied, and the states $(\lambda_1, \lambda_2, \ldots, \lambda_N)$ is a particular choice of

placing N fermions, consistent with the occupation numbers $\mathcal{N} = (n_1, n_2, \ldots)$. Note that $n_i = 0, 1$ due to the Pauli principle, and the many-body states in Eq. (2.19) are uniquely specified by a set of occupation numbers $\mathcal{N} = (n_1, n_2, \ldots)$ called the occupation number representation. Some examples of the occupation number representation are illustrated in Fig. 2.3. These anti-symmetric many-body states $|\Psi(\mathcal{N})\rangle$ can conveniently be expressed through the so-called Slater determinant using Eqs. (2.18) and (2.19)

$$\langle \mathbf{x}_1, \mathbf{x}_2, ..., \mathbf{x}_N | \Psi(\mathcal{N})\rangle = \frac{1}{\sqrt{N!}} \begin{vmatrix} \psi_{\lambda_1}(\mathbf{x}_1) & \psi_{\lambda_2}(\mathbf{x}_1) & \ldots & \psi_{\lambda_N}(\mathbf{x}_1) \\ \psi_{\lambda_1}(\mathbf{x}_2) & \psi_{\lambda_2}(\mathbf{x}_2) & \ldots & \psi_{\lambda_N}(\mathbf{x}_2) \\ \cdot & \cdot & \cdot & \cdot \\ \cdot & \cdot & \cdot & \cdot \\ \cdot & \cdot & \cdot & \cdot \\ \psi_{\lambda_1}(\mathbf{x}_N) & \psi_{\lambda_2}(\mathbf{x}_N) & \ldots & \psi_{\lambda_N}(\mathbf{x}_N) \end{vmatrix}. \tag{2.20}$$

Such a state is indeed anti-symmetric: exchanging two particles means swapping two columns of the Slater matrix which results in a minus sign, and if the occupancy is $n_i > 1$, two or more columns are identical and the wave function vanishes. Furthermore, the states in Eq. (2.19) form an orthonormal basis of the Fock space

$$\langle \Psi(\mathcal{N}') | \Psi(\mathcal{N})\rangle = \prod_j \delta_{n_j n'_j}, \tag{2.21}$$

where $\mathcal{N} = (n_1, n_2, \ldots)$ and $\mathcal{N}' = (n'_1, n'_2, \ldots)$ denote two sets of occupation numbers. Introducing fermionic creation and annihilation operators

$$\{c_{i\sigma}, c_{j\sigma'}\} = 0, \quad \left\{c^\dagger_{i\sigma}, c^\dagger_{j\sigma'}\right\} = 0, \quad \left\{c_{i\sigma}, c^\dagger_{j\sigma'}\right\} = \delta_{ij}\delta_{\sigma\sigma'}, \tag{2.22}$$

where $\{A, B\} = AB + BA$ is the anti-commutator, and defining the vacuum state as being annihilated by all annihilation operators $c_{i,\sigma}|0\rangle = 0$ and normalized $\langle 0|0\rangle = 1$, one can construct any fermionic many-body state in occupation number representation $|\Psi(\mathcal{N})\rangle$

$$|\Psi(\ldots n_{\Lambda_1} \ldots n_{\Lambda_2} \ldots n_{\Lambda_N} \ldots)\rangle = c^\dagger_{\Lambda_1} c^\dagger_{\Lambda_2} \cdots c^\dagger_{\Lambda_N} |0\rangle. \tag{2.23}$$

Here $c^\dagger_{\Lambda_i}$ creates a fermion in state $\Lambda_i = (\lambda_i, \sigma_i)$, and n_{Λ_i} indicate only those occupation numbers that are non-zero. Note that the order of creation operators must always be consistent. One usually adopts the convention that particles are created and annihilated at the first position (to the very left) in Eq. (2.23) and subsequently ordered in the correct order, picking up a certain number of (-1) factors as a consequence of the anti-commutation relations in Eq. (2.22). In the description of Fig. 2.3 an example of ordering is illustrated. With this in mind, the action of an annihilation operator on a many-body state is illustrated below. The action can be split into two cases. Case one: $\Lambda_a \notin \{\Lambda_i\}_{i=1}^N$

$$c_{\Lambda_a}|\Psi(\mathcal{N}) = c_{\Lambda_a} \prod_{i=1}^N c^\dagger_{\Lambda_i}|0\rangle = (-1)^N \prod_{i=1}^N c^\dagger_{\Lambda_i}(c_{\Lambda_a}|0\rangle) = 0, \tag{2.24}$$

where the anti-commutator relations in Eq. (2.22) and the definition of the vacuum state were used. Case two: $\Lambda_a \in \{\Lambda_i\}_{i=1}^N$

$$\begin{aligned} c_{\Lambda_a}|\Psi(\mathcal{N})\rangle &= c_{\Lambda_a}\prod_{i=1}^{N} c_{\Lambda_i}^\dagger|0\rangle = (-1)^{q_a} c_{\Lambda_a} c_{\Lambda_a}^\dagger \prod_{\substack{i=1\\ i\neq a}}^{N} c_{\Lambda_i}^\dagger|0\rangle \\ &= (-1)^{q_a}\prod_{\substack{i=1\\ i\neq a}}^{N} c_{\Lambda_i}^\dagger|0\rangle - (-1)^{q_a} c_{\Lambda_a}^\dagger c_{\Lambda_a}\prod_{\substack{i=1\\ i\neq a}}^{N} c_{\Lambda_i}^\dagger|0\rangle \\ &= (-1)^{q_a}\prod_{\substack{i=1\\ i\neq a}}^{N} c_{\Lambda_i}^\dagger|0\rangle, \end{aligned} \tag{2.25}$$

where for the last equality sign on the first row we have $q_a = a-1$, i.e. the number of times the anti-commutation relations in Eq. (2.22) must be used to bring $c_{\Lambda_a}^\dagger$ to the first position. In going from the second to the third line, the result from case 1 in Eq. (2.24) was used on the second term. A more compact way of writing and incorporating both cases is

$$c_{\Lambda_a}|\Psi(\mathcal{N})\rangle = (-1)^{q_a} n_{\Lambda_a}\prod_{\substack{i=1\\ i\neq a}}^{N} c_{\Lambda_i}^\dagger|0\rangle = (-1)^{q_a} n_{\Lambda_a}|\Psi(n_1,...,n_{\Lambda_a}\to 0, n_{\Lambda_a+1,...})\rangle, \tag{2.26}$$

where $n_{\Lambda_a} = 1, 0$ depending on whether the single particle state $\Lambda_a = (\lambda_a, \sigma_a)$ is occupied or not. The action of $c_{\Lambda_a}^\dagger$ on this state can now be evaluated

$$c_{\Lambda_a}^\dagger c_{\Lambda_a}|\Psi(\mathcal{N})\rangle = (-1)^{q_a} n_{\Lambda_a} c_{\Lambda_a}^\dagger \prod_{\substack{i=1\\ i\neq a}}^{N} c_{\Lambda_i}^\dagger|0\rangle = (-1)^{2q_a} n_{\Lambda_a}\prod_{i=1}^{N} c_{\Lambda_i}^\dagger|0\rangle = n_{\Lambda_a}|\Psi(\mathcal{N})\rangle, \tag{2.27}$$

where Eq. (2.26) was used in the first step, and in the second step, the anti-commutation relation in Eq. (2.22) was used q_a times in order to place $c_{\Lambda_a}^\dagger$ back in the correct order. Hence, $n_{\Lambda_a} = c_{\Lambda_a}^\dagger c_{\Lambda_a}$ counts the number of fermions in state Λ_a.

2.2.2 Operators in occupation number representation

Having established the many-body wave function in an occupation number representation $|\Psi(\mathcal{N})\rangle$, single-particle and two-particle operators are subsequently introduced below. This allows expressing many-body operators in terms of single-particle matrix elements. A single-particle operator becomes

$$F = \sum_{j=1}^{N} f(\mathbf{x}_j) \to \sum_{i,j}\langle\psi_i|f|\psi_j\rangle c_i^\dagger c_j, \tag{2.28}$$

where the single-particle matrix element is

$$\langle\psi_i|f|\psi_j\rangle = \int d^d r \psi_i^*(\mathbf{r}) f(\mathbf{r})\psi_j(\mathbf{r})\langle\sigma_i|f(\sigma)|\sigma_j\rangle, \tag{2.29}$$

and $\{|\psi_i\rangle\}$ form a basis of single-particle spin-orbital states. Likewise, for two-particle operators

$$G = \frac{1}{2}\sum_{\substack{j,k=1\\ j\neq k}}^{N} g\left(\mathbf{x}_j, \mathbf{x}_k\right) \rightarrow \frac{1}{2}\sum_{i,j,k,l=1} \langle\psi_i, \psi_j|g|\psi_k, \psi_l\rangle c_i^\dagger c_j^\dagger c_l c_k, \tag{2.30}$$

where it is important to note the opposite order of the annihilation operators with respect to the two-particle matrix element, and where

$$\begin{aligned}\langle\psi_i, \psi_j|g|\psi_k, \psi_l\rangle = &\int d^d r \int d^d r' \psi_i^*\left(\mathbf{r}\right)\psi_j^*\left(\mathbf{r}'\right) g\left(\mathbf{r}, \mathbf{r}'\right)\psi_k\left(\mathbf{r}\right)\psi_l\left(\mathbf{r}'\right)\\ &\times \langle\sigma_i, \sigma_j|g(\sigma, \sigma')|\sigma_k, \sigma_l\rangle.\end{aligned} \tag{2.31}$$

Thus, one can express a system of N non-interacting fermions in a rotating trap with the single-particle Hamiltonian from Eq. (2.8) according to Eq. (2.28) as

$$\begin{aligned}H^{(0)} &= \sum_{j=1}^{N} h(\mathbf{x}_j) = \sum_{\sigma}\sum_{j=1}^{N_\sigma}\left(-\frac{\hbar^2}{2\mathcal{M}}\nabla_{i\sigma}^2 + \frac{1}{2}\mathcal{M}\omega^2 r_{i\sigma}^2 + i\hbar\Omega\partial_{\varphi_{i\sigma}}\right)\\ &= \sum_{\sigma}\sum_{i}\varepsilon_i c_{i\sigma}^\dagger c_{i\sigma},\end{aligned} \tag{2.32}$$

where $c_{i\sigma}^\dagger$ creates a fermion with spin projection σ in a single-particle energy eigenstate $i = \{n_i, m_i\}$ with energy $\varepsilon_i = \hbar\omega\left(2n_i + |m_i| + 1 - m_i\Omega/\omega\right)$. Note that by choosing the single-particle energy eigenstates from Eq. (2.7), the non-interacting Hamiltonian in Eq. (2.32) of N fermions is diagonal and $n_{i\sigma} = c_{i\sigma}^\dagger c_{i\sigma}$ simply counts the number of fermions in single-particle state (i, σ). Furthermore, the non-interacting energy becomes the sum of the energies of occupied single-particle states

$$E_N^{(0)} = \sum_{\sigma}\sum_{j=1}^{N_\sigma}\varepsilon_{\lambda_j}. \tag{2.33}$$

Interactions between fermions can now be taken into account through two-particle operators, which will be motivated in the following section.

2.3 Interactions in Ultracold Atomic Gases

The experimentally realizable ultracold gases considered in this thesis are dilute with respect to a characteristic interaction range ℓ_c. This means that the distance between particles is much larger than the interaction range, or equivalently that the mean number density in 3D ρ_{3D} satisfies [6]

$$\rho_{3D}\ell_c^3 \ll 1. \tag{2.34}$$

For two neutral atoms interacting through a van der Waals force, the potential in their relative coordinate can be modeled as spherically symmetric and having a strongly repulsive core and an attractive tail

$$V(r) = \begin{cases} -C_6/r^6 & \text{if } r > r_c \\ \infty & \text{if } r \leqslant r_c \end{cases}, \tag{2.35}$$

where r_c is of the order of an atomic dimension and C_6 is the Van der Waals coefficient. This potential does not describe short-range interactions between atoms realistically, where e.g. bound states may develop, but at temperatures of the ultracold gases, $\sim$ μK, or equivalently low energies, it captures the main features of scattering [14]. From the interaction potential, one can define a characteristic interaction range $\ell_c = (2\mathcal{M}_r C_6/\hbar^2)^{1/4}$, the distance at which the kinetic energy of the relative motion with reduced mass $\mathcal{M}_r = \mathcal{M}_1\mathcal{M}_2/(\mathcal{M}_1 + \mathcal{M}_2)$ equals the interaction energy. Computing ℓ_c for alkali-metal atoms that are used in experiments, one obtains typically a length on the order of several nm. Further, the interparticle distance is $\sim$ μm, obtained from a typical mean number density $\rho_{3D} \sim 10^{12}$ cm^{-3} [34]. Hence, Eq. (2.34) is fulfilled and the intuitive picture is that scattering of more than two atoms within a volume ℓ_c^3 is negligible. Interactions between atoms in ultracold gases should thus be describable in terms of the scattering amplitude f_k of two atoms, where k is the relative momentum.

A second important length scale is the spatial extent of the wave function of a particle. According to quantum mechanics, it can be estimated by the de Broglie wavelength $\lambda_{dB} = \sqrt{2\pi\hbar^2/mk_BT}$. If it is computed for alkali-metal atoms at temperatures T$\sim$ μK, one obtains $\sim$ 1 μm, which is of the order of the interparticle spacing and much larger than the characteristic interaction length $\lambda_{dB} \gg \ell_c$. Finer details of the interaction potential are therefore less important and it is commonplace to replace the true atomic interaction potential with a more convenient contact interaction[1]

$$V(\mathbf{r}) = g\delta^{(3)}(\mathbf{r}), \tag{2.36}$$

i.e. a delta function which reproduces the correct low energy $k\ell_c \ll 1$ scattering amplitude f_k with interaction strength g [35]. At low energies, scattering in states with angular momentum $l \neq 0$ ($l = 1, 2, ...$) in the relative motion experience an effective centrifugal barrier of strength $E_c \approx \hbar^2 l^2/(\mathcal{M}_r\ell_c^2)$. For small l and typical atomic masses, an equivalent temperature $E_c/k_B \approx 1$ mK is obtained, below which scattering in states with the lowest angular momentum l is usually dominant (compare to μK in experiments with ultracold atoms to see that this is always fulfilled). Due to the Pauli principle, this corresponds to s-wave ($l = 0$) scattering for two fermions in a singlet state, and p-wave ($l = 1$) scattering for two fermions in a triplet state where s-wave scattering is forbidden. Thus, at the lowest energies, identical fermions act as if they were non-interacting. Gases at temperatures below mK, where collisions with the lowest angular momentum dominate, define the regime of ultracold atoms [14]. The s-wave scattering amplitude is determined by the corresponding phase shift $\delta_0(k)$, which in the limit of the lowest energies $k \to 0$ is completely specified by a single parameter a_{3D}, the scattering length [32]

$$f(k) = \frac{a_{3D}}{k\cot\delta_0(k) - ik} \xrightarrow[k\to 0]{} -\frac{a_{3D}}{1 + ika_{3D}}. \tag{2.37}$$

[1]The correct contact interaction is actually a regularized delta function $\delta^{(3)}_{reg}(\mathbf{r}) = \delta^{(3)}(\mathbf{r})\frac{\partial}{\partial r}r$ to ensure self-adjointness (hermicity in the finite-dimensional case) of the Hamiltonian. However, for functions that are regular at the origin $r = 0$, which will be the case in this thesis, one can simply use equation (2.36) [35].

Hence, the contact interaction $V(\mathbf{r})$ for two ultracold atoms in equation (2.36) is completely determined by the scattering length, and the interaction strength at low energies is [14]

$$g = \frac{4\pi\hbar^2 a_{3D}}{2\mathcal{M}_r} \tag{2.38}$$

The scattering length a_{3D}, and consequently the interaction strength, is tunable experimentally with a magnetic field by the phenomenon of Feshbach resonance [36]. For two ultracold atoms scattering, this generally relies on the coupling between a state of unbound atoms to a tightly bound molecular state. The difference in magnetic moments between these states allows for tuning of their relative energy, and when the incident energy of the unbound atoms matches that of the bound state, a resonance occurs. In other words, the two scattering atoms are temporarily trapped in a quasi-bound state, meaning stronger interactions, when the incident energy is closer to that of the bound molecular state energy. When the incident energy is far from the bound molecular state energy, the scattering length is small and the two unbound atoms interact weakly.

2.3.1 Interactions in two Dimensions

In two dimensions, one has the contact interaction

$$V(\mathbf{r}) = g\delta^{(2)}(\mathbf{r}), \tag{2.39}$$

however, a delta-function interaction in two dimensions requires renormalization (also needed in 3D beyond the perturbative limit) such that g is replaced by a scale-dependant coupling $g(\kappa) = 2\pi/\ln(1/\kappa a_{2D})$ [29]. Here, a_{2D} is the two-dimensional scattering length and κ a characteristic wave number such as the inverse de Broglie wavelength or the Fermi momentum. This is an example of a quantum anomaly where a symmetry in the classical theory is broken in the corresponding quantum theory: the bare coupling g parameter in Eq. (2.39) picks up an additional regulator scale κ such that divergences are canceled. Yet, in a quasi-2D regime where particles occupy the lowest state of an out-of-plane harmonic oscillator with oscillator length ℓ_z, the scattering length is [14, 37]

$$a_{2D} \sim \ell_z e^{-\sqrt{\pi/2}\frac{\ell_z}{a_{3D}}}. \tag{2.40}$$

It is an exponentially small function of a_{3D} in the case where $0 < a_{3D} \ll \ell_z$, allowing one to replace the interaction strength by a constant $g = \sqrt{8\pi}(a_{3D}/\ell_z)$ [29, 30, 37]. Hence, in the perturbative limit of weak interactions at low energies, which will be the case in this thesis, the interaction strength is independent of energy.

2.3.2 Interacting Many-Body Hamiltonian

In this thesis, two-component $\sigma = \uparrow, \downarrow$ fermions are considered with $N_\uparrow$ fermions in spin state $\uparrow$ and $N_\downarrow$ fermions in spin state $\downarrow$. We consider N-particle configurations with an equal number of both spin components for even N, and one excess spin for

odd N. The full 2D many-body Hamiltonian takes the form

$$H = \sum_{\sigma=\uparrow,\downarrow} \sum_{i=1}^{N_\sigma} \left(-\frac{\hbar^2}{2\mathcal{M}} \nabla_{i\sigma}^2 + \frac{\mathcal{M}\omega^2}{2} r_{i\sigma}^2 + i\hbar\Omega\partial_{\varphi_{i,\sigma}} \right) + g \sum_{i=1}^{N_\uparrow} \sum_{j=1}^{N_\downarrow} \delta^{(2)} \left(\mathbf{r}_{i\uparrow} - \mathbf{r}_{j\downarrow} \right), \quad (2.41)$$

where the interaction only takes place between fermions of opposite spin. As discussed above, this is due to the Pauli principle which at low energies only allows scattering of two fermions in a singlet state and can be seen mathematically by noting that if $\mathbf{r_{i\uparrow}} = \mathbf{r_{j\uparrow}}$, two rows of the Slater matrix in Eq. (2.20) become identical and the wave function vanishes. The above Hamiltonian can also be written in occupation number representation as

$$H = \sum_{\sigma=\uparrow,\downarrow} \sum_i \varepsilon_i c_{i\sigma}^\dagger c_{i\sigma} + g \sum_{i,j,k,l} w_{ijkl} c_{i\uparrow}^\dagger c_{j\downarrow}^\dagger c_{l\downarrow} c_{k\uparrow}, \quad (2.42)$$

where $i = \{n_i, m_i\}$ and

$$w_{ijkl} = \int d^2 r \psi_i^*(\mathbf{r}) \psi_j^*(\mathbf{r}) \psi_k(\mathbf{r}) \psi_l(\mathbf{r}), \quad (2.43)$$

with $\{\psi_i(\mathbf{r})\}$ the single-particle wave functions from Eq. (2.7). An important observation is that the interaction preserves angular momentum and connects at most many-body states that differ by two occupation numbers. This is discussed in more detail in Appendix A.1.

2.4 Nonrelativistic Conformal Symmetry Algebra

The interacting many-body Hamiltonian in Eq. (2.41) is part of a nonrelativistic conformal symmetry algebra. The symmetry puts strong constraints on the energy spectrum, where, if all so-called primary states are known, the entire energy spectrum is known by the use of three spectrum-generating operators. This section is structured as follows: First, generators of symmetry transformations are introduced in Sec. 2.4.1. Second, a spectrum-generating operator in the case of the simple harmonic oscillator is discussed in Sec. 2.4.2, after which the spectrum-generating operators of the non-relativistic conformal symmetry are introduced in Sec. 2.4.3. Then, primary states and conformal energy towers are defined in Sec. 2.4.4. Last, the Casimir operator of the conformal symmetry group and its properties are discussed in Sec. 2.4.5.

2.4.1 Generators

Before introducing the generators of scale and conformal transformations, some more familiar examples are given below. In quantum mechanics, a transformation such as time or space translation, is given by the action of some unitary (or anti-unitary in general) operator [1]. The generator of such a transformation is another operator that parameterizes an infinitesimal transformation. For infinitesimal space translations $(t, \mathbf{r}) \to (t, \mathbf{r} + d\mathbf{r})$ of all particle coordinates, the translation operator $\mathcal{U}_\mathbf{r}$ takes the form [32]

$$\mathcal{U}_\mathbf{r}(d\mathbf{r}) = 1 - \frac{\mathbf{P} \cdot d\mathbf{r}}{\hbar}, \quad (2.44)$$

where $\mathbf{P} = \sum_\sigma \sum_{i=1}^{N_\sigma} \mathbf{p}_{i\sigma}$ is the total momentum operator and $d\mathbf{r}$ an infinitesimal spatial displacement. We say that the momentum operator is the generator of space translations, and a finite space translation is obtained by compounding $N \to \infty$ infinitesimal translation with spatial displacement $\Delta r/N$, given by

$$\mathcal{U}_{\mathbf{r}}(\Delta\mathbf{r}) = \lim_{N \to \infty} \left(1 - \frac{\mathbf{P} \cdot \Delta\mathbf{r}}{N\hbar}\right)^N = \exp\left(-i\frac{\mathbf{P} \cdot \Delta\mathbf{r}}{\hbar}\right). \tag{2.45}$$

Similarly, the Hamiltonian H, and the out-of-plane total angular momentum $M_z = \sum_{\sigma=\uparrow\downarrow} \sum_{i=1}^{N_\sigma} L_{z,i\sigma}$, are the generators of time translations and in-plane rotations $(t, \mathbf{r}) \to (t + \Delta t, \mathbf{r})$, $(t, r, \varphi) \to (t, r, \varphi + d\varphi)$ respectively. Infinitesimally,

$$\mathcal{U}_t(dt) = 1 - i\frac{H dt}{\hbar}, \quad \mathcal{U}_\varphi(d\varphi) = 1 - i\frac{M_z d\varphi}{\hbar}, \tag{2.46}$$

where $\mathcal{U}_t(t)$ is the time evolution operator, and $\mathcal{U}_\varphi(\varphi)$ the in-plane rotation operator which take the form (for a time-independent Hamiltonian)

$$\mathcal{U}_t(t) = \exp\left(-i\frac{Ht}{\hbar}\right), \quad \mathcal{U}_\varphi(\varphi) = \exp\left(-i\frac{M_z\varphi}{\hbar}\right). \tag{2.47}$$

Now, introducing the generator D of dilatations

$$D = \frac{1}{2\hbar} \sum_{\sigma=\uparrow,\downarrow} \sum_{i=1}^{N_\sigma} (\mathbf{r}_{i\sigma} \cdot \mathbf{p}_{i\sigma} + \mathbf{p}_{i\sigma} \cdot \mathbf{r}_{i\sigma}) = -\frac{i}{2} \sum_{\sigma=\uparrow,\downarrow} \sum_{i=1}^{N_\sigma} (\mathbf{r}_{i\sigma} \cdot \nabla_{i\sigma} + \nabla_{i\sigma} \cdot \mathbf{r}_{i\sigma}), \tag{2.48}$$

it corresponds to rescaling time and position coordinates by a constant factor λ $(t, \mathbf{r}) \to (\lambda^2 t, \lambda\mathbf{x})$ [6, 16, 29]. The generator of special conformal transformations $(t, \mathbf{r}) \to (t, \mathbf{r})/(1 + \lambda t)$ is [15, 17, 29]

$$\tilde{C} = \sum_{\sigma=\uparrow\downarrow} \sum_{i=1}^{N_\sigma} \frac{r_{i\sigma}^2}{2}, \tag{2.49}$$

which takes the same form as the harmonic oscillator trap potential. As will become clear in Sec. 2.4.3, different parts of the interacting many-body Hamiltonian in Eq. (2.41) leave the action invariant under transformations generated by M_z, D, or C. Hence, these are symmetry transformations, and the interacting many-body Hamiltonian in Eq. (2.41) is part of a nonrelativistic symmetry algebra which is discussed in Sec. 2.4.3.

2.4.2 Spectrum-Generating Operators: Simple Harmonic Oscillator

Before considering spectrum-generating operators in the two-dimensional interacting Fermi gas, a familiar example is given here. The textbook example of a spectrum-generating operator is in the case of a one-dimensional harmonic oscillator

$$H_{1\mathrm{D}} = \frac{p^2}{2\mathcal{M}} + \frac{1}{2}\mathcal{M}\omega^2 x^2. \tag{2.50}$$

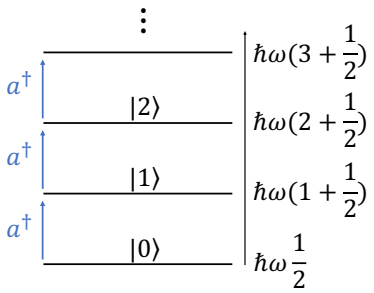

Figure 2.4: Illustration of the creation operator $a^\dagger$ generating a ladder for energy spectrum from the ground state $|0\rangle$ of the 1D harmonic oscillator, with an energy spacing of exactly $\hbar\omega$.

Introducing annihilation and creation operators ($\ell_{ho} = \sqrt{\hbar/\mathcal{M}\omega}$)

$$a = \frac{1}{\sqrt{2}}\left(\frac{\ell_{ho}p}{\hbar} - i\frac{x}{\ell_{ho}}\right), \tag{2.51}$$

$$a^\dagger = \frac{1}{\sqrt{2}}\left(\frac{\ell_{ho}p}{\hbar} + i\frac{x}{\ell_{ho}}\right), \tag{2.52}$$

where $[a, a^\dagger] = 1$, one can rewrite the Hamiltonian as

$$H_{1\mathrm{D}} = \hbar\omega(a^\dagger a + \frac{1}{2}). \tag{2.53}$$

The ground state is $|0\rangle$, defined as $a|0\rangle = 0$ and $\langle 0|0\rangle = 1$, with energy eigenvalue $H_{1\mathrm{D}}|0\rangle = \hbar\omega/2|0\rangle$. From the commutation relations of a,$a^\dagger$ with the Hamiltonian,

$$[H_{1\mathrm{D}}, a^\dagger] = \hbar\omega a^\dagger, \quad [H_{1\mathrm{D}}, a] = -\hbar\omega a, \tag{2.54}$$

we can see that $|0\rangle$ together with $a^\dagger$ generate the entire energy spectrum by raising the energy by exactly $\hbar\omega$

$$H_{1\mathrm{D}}a^\dagger|0\rangle = ([H_{1\mathrm{D}}, a^\dagger] + a^\dagger H_{1\mathrm{D}})|0\rangle = \hbar\omega(1+\frac{1}{2})a^\dagger|0\rangle. \tag{2.55}$$

A general normalized energy eigenstate, parametrized by a quantum number n, with energy $\hbar\omega(n+1/2)$ is then given by

$$|n\rangle = \frac{(a^\dagger)^n}{\sqrt{n!}}|0\rangle. \tag{2.56}$$

In summary, with the ground state $|0\rangle$, and the spectrum generating raising operator $a^\dagger$ and lowering operator a, a ladder for energy spectrum is obtained with spacing exactly $\hbar\omega$ as illustrated in Fig. 2.4. In the next section, spectrum-generating operators of the interacting many-body system will be introduced, but it is helpful to always keep in mind the example of the simple harmonic oscillator.

2.4.3 Spectrum-Generating Operators: 2D Interacting Fermi Gas

Having familiarized ourselves with a spectrum-generating operator in the previous section, we are now ready to consider spectrum-generating operators in the two-dimensional interacting Fermi gas. These are important because, with the primary states defined in the following section, one knows the entire energy spectrum of the system. Introducing some notation below

$$M_z = -i\hbar \sum_{\sigma=\uparrow,\downarrow} \sum_{i=1}^{N_\sigma} \partial_{\varphi_{i\sigma}}, \tag{2.57}$$

where M_z is the out-of-plane total angular momentum,

$$H_{\text{trap}} = \sum_{\sigma=\uparrow,\downarrow} \sum_{i=1}^{N_\sigma} \frac{\mathcal{M}\omega^2}{2} r_{i\sigma}^2 = \mathcal{M}\omega^2 \tilde{C}, \tag{2.58}$$

is the harmonic oscillator trap operator and $\tilde{C}$ is the generator of special conformal transformations $(t, \mathbf{r}) \to (t, \mathbf{r})/(1 + \lambda t)$ in Eq. (2.49), and

$$H_{\omega=0} = H - H_{\text{trap}} + \Omega M_z = \sum_{\sigma=\uparrow,\downarrow} \sum_{i=1}^{N_\sigma} \left(-\frac{\hbar^2 \nabla_{i\sigma}^2}{2\mathcal{M}} \right) + g \sum_{i=1}^{N_\uparrow} \sum_{j=1}^{N_\downarrow} \delta^{(2)} \left(\mathbf{r}_{i\uparrow} - \mathbf{r}_{j\downarrow} \right), \tag{2.59}$$

is the Hamiltonian of the interacting system without a trap and rotation, the full Hamiltonian in Eq. (2.41) can be written with three parts as

$$H = H_{\omega=0} - \Omega M_z + H_{\text{trap}}. \tag{2.60}$$

Note that $H_{\omega=0}$ is scale-invariant, i.e. if all coordinates are rescaled $\mathbf{r}_{i\sigma} \to \lambda \mathbf{r}_{i\sigma}$, it changes as $H_{\omega=0} \to H_{\omega=0}/\lambda^2$. The reason for this is the homogeneity of the delta function interaction $\delta^{(d)}(\lambda \mathbf{r}) = \delta(\mathbf{r})/\lambda^d$. This makes the two-dimensional weakly interacting Fermi gas a special case because for $d = 2$, the delta function interaction scales in the same way as the kinetic term $\nabla^2 \to \nabla^2/\lambda^2$. Furthermore, the scaling transformation $(t, \mathbf{r}) \to (\lambda^2 t, \lambda \mathbf{x})$ leaves the Schrödinger equation (Eq. (2.1)) invariant. This means that the full interacting many-body Hamiltonian H is part of a nonrelativistic symmetry algebra formed by a scale-invariant $H_{\omega=0}$, the generator of scale transformations D (Eq. (2.48)), the generator of special conformal transformations $\tilde{C}$ (Eq. (2.49)), and the generator of in-plane rotations M_z.

The conformal symmetry implies a one-to-one correspondence between free-space eigenstates at zero energy and particular states in a harmonic trap called primary states [5, 17]. Furthermore, the symmetry also generates a spectrum of breathing-mode excitations through the ladder operator $L^\dagger$ [5, 6, 38]

$$\begin{aligned} L^\dagger &= iD + \frac{H}{\hbar\omega} - \frac{2H_{\text{trap}}}{\hbar\omega} + \frac{\Omega M_z}{\hbar\omega} \\ &= iD + \frac{H_{\omega=0}}{\hbar\omega} - \frac{H_{\text{trap}}}{\hbar\omega}, \end{aligned} \tag{2.61}$$

where from the commutation relations

$$[D, M_z] = 0, \tag{2.62}$$
$$[H_{\omega=0}, H_{\text{trap}}] = -i(\hbar\omega)^2 D, \tag{2.63}$$
$$[D, H_{\text{trap}}] = -2iH_{\text{trap}}, \tag{2.64}$$
$$[D, H_{\omega=0}] = 2iH_{\omega=0}, \tag{2.65}$$

one has

$$\begin{aligned} \left[H, L^\dagger\right] &= +2\hbar\omega L^\dagger \\ [H, L] &= -2\hbar\omega L \\ \left[L^\dagger, L\right] &= -\frac{4}{\hbar\omega}(H + \Omega M_z) = -\frac{4}{\hbar\omega}(H_{\omega=0} + H_{\text{trap}}). \end{aligned} \tag{2.66}$$

Comparing these commutation relations to Eq. (2.54), one can see that $L^\dagger$ is a spectrum-generating operator that raises the energy by exactly twice the trapping frequency $2\hbar\omega$ (c.f. Fig. 2.4) in the two-dimensional weakly interacting Fermi gas.

Two more spectrum generating operators $Q_\pm^\dagger$ can be defined, with the center-of-mass momentum (total momentum) operator

$$\mathbf{P} = \sum_{\sigma=\uparrow,\downarrow} \sum_{i=1}^{N_\sigma} \mathbf{p}_{i\sigma}, \tag{2.67}$$

and total position operator

$$\mathbf{K} = \sum_{\sigma=\uparrow,\downarrow} \sum_{i=1}^{N_\sigma} \mathbf{r}_{i\sigma} = N\mathbf{C}, \tag{2.68}$$

where $\mathbf{C} = (1/N)\mathbf{K}$ denote the center-of-mass position, one has

$$\mathbf{Q} = \frac{1}{\sqrt{2}}\left(\frac{\ell_{ho}}{\hbar}\mathbf{P} - \frac{i}{\ell_{ho}}\mathbf{K}\right) = \frac{1}{\sqrt{2}}\left(\frac{\ell_{ho}}{\hbar}\mathbf{P} - \frac{i}{\ell_{ho}}N\mathbf{C}\right), \tag{2.69}$$

(c.f Eq. (2.51)) from which $Q_\pm$ are defined as

$$Q_\pm = Q_x \mp iQ_y. \tag{2.70}$$

These correspond to center-of-mass excitations, and from the commutation relations

$$[H, Q_\pm^\dagger] = +\hbar(\omega \mp \Omega)Q_\pm^\dagger, \quad [M_z, Q_\pm^\dagger] = \pm\hbar Q_\pm^\dagger, \tag{2.71}$$

$$[H, Q_\pm] = -\hbar(\omega \mp \Omega)Q_\pm, \quad [M_z, Q_\pm] = \mp\hbar Q_\pm, \tag{2.72}$$

$$[Q_+, Q_-] = 0, \quad [Q_\pm, Q_\mp^\dagger] = 0, \quad [Q_\pm, Q_\pm^\dagger] = 2N, \tag{2.73}$$

we see that $Q_+^\dagger$ creates excitations by increasing the energy with $\hbar(\omega - \Omega)$, while increasing the angular momentum in the direction of rotation $M \to M + 1$. The $Q_-^\dagger$ operator also creates excitations, but by increasing energy with $\hbar(\omega + \Omega)$, while decreasing angular momentum in the direction of rotation $M \to M - 1$. Note that the commutation relations are independent of interaction potential, thus holding

irrespective of scale invariance [39].

The three spectrum-generating operators, the breathing mode excitation $L^\dagger$, and center-of-mass excitations $Q_\pm^\dagger$, are linearly independent but do not commute

$$[L^\dagger, Q_\pm] = -2Q_\mp^\dagger \quad [L, Q_\pm^\dagger] = 2Q_\mp. \tag{2.74}$$

This means that eigenstates generated by $L^\dagger$ and $Q_+^\dagger Q_-^\dagger$ have finite overlap. For example, consider an eigenstate of the hamiltonian $H|\Psi\rangle = E|\Psi\rangle$, that further fulfill $L|\Psi\rangle = Q_+|\Psi\rangle = Q_-|\Psi\rangle = 0$, and new energy eigenstates $L^\dagger|\Psi\rangle$, $Q_+^\dagger Q_-^\dagger|\Psi\rangle$, both with energy $E + 2\hbar\omega$, and overlap

$$\begin{aligned}\langle\Psi|LQ_+^\dagger Q_-^\dagger|\Psi\rangle &= \langle\Psi|([L, Q_+^\dagger] + Q_+^\dagger L)Q_-^\dagger|\Psi\rangle = -2\langle\Psi|Q_-Q_-^\dagger|\Psi\rangle \\ &= -2\langle\Psi|([Q_-, Q_-^\dagger] + Q_-^\dagger Q_-)|\Psi\rangle = -4N\langle\Psi|\Psi\rangle,\end{aligned} \tag{2.75}$$

where Eq. (2.74) and $Q_+|\psi\rangle = 0$ was used for the second equality sign, and Eq. (2.73) and $Q_-|\Psi\rangle = 0$ for the last equality. Eq. (2.75) is indeed non-zero.

Breathing mode and center-of-mass excitation can be disentangled by defining an internal breathing mode operator R [5, 29, 40]

$$R^\dagger = L^\dagger - \frac{1}{2N}(Q_+^\dagger Q_-^\dagger + Q_-^\dagger Q_+^\dagger). \tag{2.76}$$

It is internal in the sense that $R^\dagger$ only acts on the internal hyperradius $\tilde{R} = \sqrt{\sum_{\sigma,i} |\mathbf{r}_{i\sigma} - \mathbf{C}|^2}$, where $\mathbf{C} = (1/N)\mathbf{K} = (1/N)\sum_{i\sigma} \mathbf{r}_{i\sigma}$ is the center-of-mass position (this will be discussed in more detail in Sec. 2.5). From the commutation relations

$$[H, R^\dagger] = 2\hbar\omega R^\dagger, \tag{2.77}$$

$$[H, R] = -2\hbar\omega R, \tag{2.78}$$

$$[R^\dagger, R] = -\frac{4}{\hbar\omega}(H + \Omega M_z) + \frac{1}{N}(Q_+Q_+^\dagger + Q_+^\dagger Q_+ + Q_-Q_-^\dagger + Q_-^\dagger Q_-), \tag{2.79}$$

we see that the internal breathing mode operator $R^\dagger$ is also a spectrum-generating operator and furthermore, it commutes with all $Q_\pm$ operators

$$[R, Q_\pm] = [R^\dagger, Q_\pm] = [R, Q_\pm^\dagger] = [R^\dagger, Q_\pm^\dagger] = 0, \tag{2.80}$$

hence only acting on the hyperradius.

2.4.4 Primary States and Conformal Towers

Having introduced the spectrum-generating operators, the internal breathing mode operator $R^\dagger$, and the center-of-mass operators $Q_\pm^\dagger$, we can now define the so-called primary states, from which the entire energy spectrum can be generated. Similarly to the ground state $|0\rangle$ for the simple harmonic oscillator in Sec. 2.4.2, one can define primary states $|P\rangle$, with energy $H|P\rangle = E_g|P\rangle$ and angular momentum

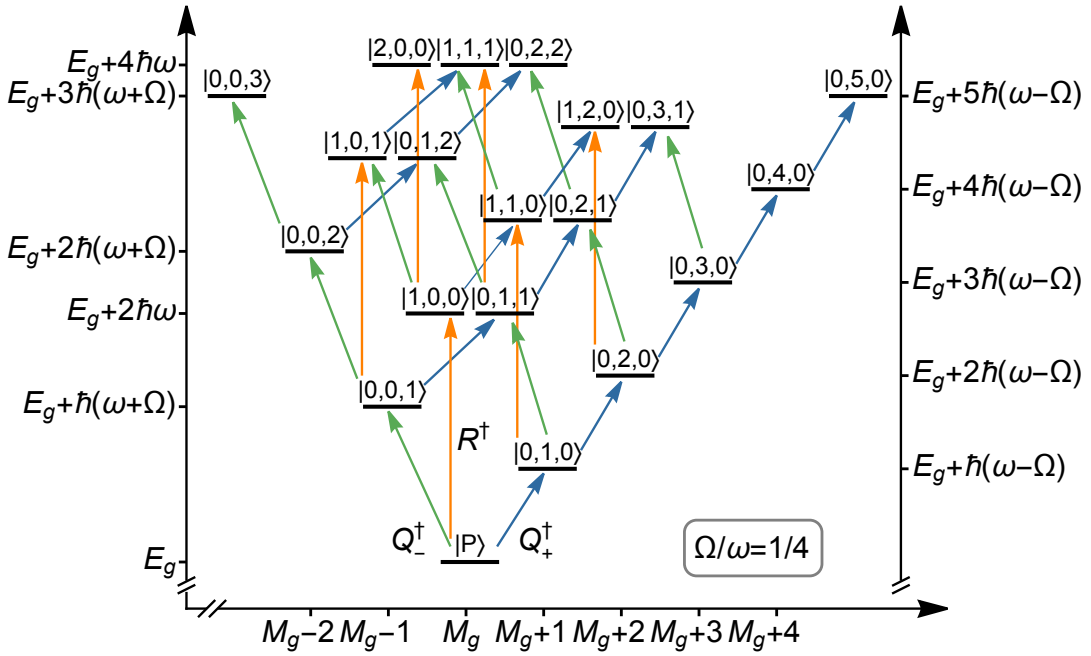

Figure 2.5: A conformal tower created from a primary state $|P\rangle$ with energy $H|P\rangle = E_g|P\rangle$ and total angular momentum $M_z|P\rangle = \hbar M_g|P\rangle$ for a rotation $\Omega/\omega = 1/4$. Blue arrows are center-of-mass excitations created by $Q_+^\dagger$ that increase the energy by $\hbar(\omega - \Omega)$ while changing the angular momentum by $+1$. Green arrows are center-of-mass excitations created by $Q_-^\dagger$ that increase the energy by $\hbar(\omega + \Omega)$ while changing the angular momentum by -1 Orange arrows are internal breathing mode excitations created by $R^\dagger$ that increase the energy by $2\hbar\omega$ while preserving the total angular momentum.

$M_z|P\rangle = \hbar M_g|P\rangle$ as being annihilated by the three spectrum generating operators $R, Q_\pm$

$$R|P\rangle = Q_+|P\rangle = Q_-|P\rangle = 0. \tag{2.81}$$

As illustrated in Fig 2.5, a primary state $|P\rangle$ with energy E_g and total angular momentum $\hbar M_g$ forms the ground step of a semi-infinite ladder, a conformal tower, where repeated excitations with $R^\dagger, Q_\pm^\dagger$ give the orthogonal set of non-primary excited states

$$|a, b, c\rangle_P = (R^\dagger)^a (Q_+^\dagger)^b (Q_-^\dagger)^c |P\rangle, \tag{2.82}$$

with energy

$$H|a, b, c\rangle_P = (E_g + \hbar\omega(2a + b(1 - \Omega/\omega) + c(1 + \Omega/\omega)\ )|a, b, c\rangle_P, \tag{2.83}$$

and total angular momentum

$$M_z|a, b, c\rangle_P = \hbar(M_g + b - c)|a, b, c\rangle_P. \tag{2.84}$$

Note that in Fig. 2.5, only one primary state and its conformal tower are shown, but there is actually an infinite number, as will become evident in the results section. However, the primary states and their ladders comprise the entire energy spectrum.

In other words, the primary and non-primary states form a complete set of the Hilbert space. The next section will introduce a Casimir operator such that different conformal towers can be distinguished.

2.4.5 Casimir Operator

In order to distinguish states within different conformal towers $|a, b, c\rangle_P$ and $|a', b', c'\rangle_{P'}$, the nonrelativistic conformal SO(2,1) (two-dimensional Lorentz group) symmetry Lie algebra is introduced

$$[T_1, T_2] = -iT_3, \quad [T_2, T_3] = iT_1, \quad [T_3, T_1] = iT_2, \tag{2.85}$$

where we can identify [29]

$$T_1 = \frac{1}{4}(R^\dagger + R), \tag{2.86}$$

$$T_2 = \frac{1}{4i}(R^\dagger - R), \tag{2.87}$$

$$T_3 = \frac{1}{2}\frac{(H + \Omega M_z)}{\hbar\omega} - \frac{1}{4N}(Q_+ Q_+^\dagger + Q_-^\dagger Q_-). \tag{2.88}$$

The reason for introducing the Lie algebra is that the Casimir element T of the group, which commutes with the Hamiltonian and gives a conserved quantity, can be obtained through

$$T = 4(T_3^2 - T_1^2 - T_2^2), \tag{2.89}$$

which is guaranteed to commute with all elements of the algebra T_1, T_2, and T_3 [6, 29]. Thus, T is constant within each conformal tower, which can be seen more easily from the commutation relations

$$[T, H] = 0, \quad [T, R] = 0, \quad [T, R^\dagger] = 0, \quad [T, Q_\pm] = 0, \quad [T, Q_\pm^\dagger] = 0. \tag{2.90}$$

Evaluating the expectation value of the Casimir operator for a primary state, to leading order in perturbation theory, gives

$$\langle P|T|P\rangle = \left(\frac{E_g^{(0)} + \hbar\Omega M_g}{\hbar\omega} - 1\right)\left(\frac{E_g^{(0)} + \hbar\Omega M_g}{\hbar\omega} - 3\right), \tag{2.91}$$

where $E_g^{(0)}$, M_g denotes the non-interacting contribution to the ground step energy and the total angular momentum of the ground step respectively, of a conformal tower. Note that the ground step energy without rotation is $E_{g,\Omega=0} = E_g^{(0)} + \hbar\Omega M_g$ and T can thus be seen to relate to the ground step energy without rotation $\Omega = 0$. Furthermore, the Casimir T is known [5, 6, 29, 38], but the results revealing the nonrelativistic conformal invariance in a rotating trap in Ch. 4 are new.

2.5 Separation of the Many-Body Wave Function

Now that the consequences of the nonrelativistic conformal symmetry on the energy spectrum have been discussed, this section will discuss the microscopic origin of the

symmetry. The origin is a factorization of the many-body wave function [5, 6, 29]

$$\Psi(\mathbf{r}_{1,\uparrow}, \dots \mathbf{r}_{1,\downarrow} \dots) = \Psi_{\text{c.m.}}(\mathbf{C}) \frac{F(\tilde{R})}{\tilde{R}^{N-2}} \phi(\mathbf{n}), \tag{2.92}$$

where $\Psi_{\text{c.m.}}(\mathbf{C})$ is the center-of-mass part (which factories for any Galilean-invariant interaction), $F(\tilde{R})$ the internal hyperradial part with internal hyperradius $\tilde{R} = \sqrt{\sum_{i\sigma} |\mathbf{r}_{i\sigma} - \mathbf{C}|^2}$, $\phi(\mathbf{n})$ a hyperangular part that depend on the remaining internal coordinates $\mathbf{n} = (\mathbf{r}_{i\uparrow} - \mathbf{C} \dots, \mathbf{r}_{i\downarrow} - \mathbf{C} \dots)/\tilde{R}$, and N is the particle number. One can see this by considering the Heisenberg equations of motion (Eq. (2.9)) for the center-of-mass momentum $\mathbf{P} = (P_x, P_y)$ in Eq. (2.67) and the center-of-mass position $\mathbf{C} = (C_x, C_y)$ in (2.68). Starting with $\mathbf{P}$, one has

$$\frac{d\mathbf{P}}{dt} = \frac{1}{i\hbar}[\mathbf{P}, H] = \frac{1}{i\hbar}[\mathbf{P}, H_{\text{trap}} - \Omega M_z] = -N\mathcal{M}\omega^2 \mathbf{C} - \boldsymbol{\Omega} \times \mathbf{P}, \tag{2.93}$$

where $[\mathbf{P}, H_{\omega=0}] = 0$ was used for the second equality, and $\boldsymbol{\Omega} = \Omega\hat{\mathbf{z}}$ is the out-of-plane rotation. Next consider $\mathbf{C}$

$$\frac{d\mathbf{C}}{dt} = \frac{1}{i\hbar}[\mathbf{C}, H] = \frac{1}{i\hbar}[\mathbf{C}, H_{\omega=0} - \Omega M_z] = \frac{\mathbf{P}}{N\mathcal{M}} - \boldsymbol{\Omega} \times \mathbf{C}, \tag{2.94}$$

where $[\mathbf{C}, H_{\text{trap}}] = 0$ was used for the second equality. Now note that Eq. (2.93) and (2.94) are identical to Eqs. (2.11) and (2.10) if one lets $\mathcal{M} \to N\mathcal{M}$. The center of mass of the rotating two-dimensional interacting Fermi gas thus behaves as a fictitious particle of mass $N\mathcal{M}$ trapped in a rotating harmonic potential

$$\begin{aligned} H_{\text{c.m.}} &= \frac{P^2}{2(N\mathcal{M})} + \frac{1}{2}(N\mathcal{M})\omega^2 C^2 - \Omega M_z^{(\text{c.m.})} \\ &= H_{\omega=0}^{(\text{c.m.})} + H_{\text{trap}}^{(\text{c.m.})} - \Omega M_z^{(\text{c.m.})}, \end{aligned} \tag{2.95}$$

where $M_z^{(\text{c.m.})} = C_x P_y - C_y P_x$ is the angular momentum of the center of mass, or the angular momentum of the fictitious particle of mass $N\mathcal{M}$. The notation $H_{\omega=0}^{(\text{c.m.})} = P^2/2(N\mathcal{M})$ now denote the center-of-mass Hamiltonian without a trap, and $H_{\text{trap}}^{(\text{c.m.})} = (N\mathcal{M})\omega^2 C^2/2$ the center-of-mass part of the harmonic trapping potential in Eq. (2.58). Hence, the center-of-mass momentum and center-of-mass position are only coupled among themselves. The reason is that the interaction potential cannot change the total momentum, and only acts on the internal coordinates $\mathbf{r}'_{i\sigma} = \mathbf{r}_{i\sigma} - \mathbf{C}$ relative to the center of mass

$$\delta^{(2)}(\mathbf{r}_{i\uparrow} - \mathbf{r}_{j\downarrow}) = \delta^{(2)}(\mathbf{r}'_{i\uparrow} + \mathbf{C} - (\mathbf{r}'_{j\downarrow} + \mathbf{C})) = \delta^{(2)}(\mathbf{r}'_{i\uparrow} - \mathbf{r}'_{j\downarrow}). \tag{2.96}$$

It is further instructive to see that the total angular momentum splits into two parts $M_z = M_z^{(\text{c.m.})} + M_z^{(I)}$, where I stands for internal. With internal momentum

$\mathbf{p}'_{i\sigma} = \mathbf{p}_{i\sigma} - \mathbf{P}/N$ relative to the center-of-mass position, we have

$$\begin{aligned} M_z &= \hat{\mathbf{z}} \cdot \sum_{\sigma=\uparrow\downarrow} \sum_i \mathbf{r}_{i\sigma} \times \mathbf{p}_{i\sigma} = \hat{\mathbf{z}} \cdot \sum_{\sigma=\uparrow\downarrow} \sum_i (\mathbf{r}'_{i\sigma} + \mathbf{C}) \times \left(\mathbf{p}'_{i\sigma} + \frac{\mathbf{P}}{N} \right) \\ &= \hat{\mathbf{z}} \cdot \left(\sum_{\sigma=\uparrow\downarrow} \sum_i \mathbf{r}'_{i\sigma} \times \mathbf{p}'_{i\sigma} + \left(\sum_{\sigma=\uparrow\downarrow} \sum_i \mathbf{r}'_{i\sigma} \right) \times \frac{\mathbf{P}}{N} + \mathbf{C} \times \left(\sum_{\sigma=\uparrow\downarrow} \sum_i \mathbf{p}'_{i\sigma} \right) + \mathbf{C} \times \mathbf{P} \right) \\ &= \hat{\mathbf{z}} \cdot \left(\sum_{\sigma=\uparrow\downarrow} \sum_i \mathbf{r}'_{i\sigma} \times \mathbf{p}'_{i\sigma} + \mathbf{C} \times \mathbf{P} \right) = M_z^{(I)} + M_z^{(\text{c.m.})}, \end{aligned} \tag{2.97}$$

where $\sum_{i\sigma} \mathbf{r}'_{i\sigma} = \sum_{i\sigma} \mathbf{p}'_{i\sigma} = 0$ was used in going to the last line. The internal and the center-of-mass coordinates commute

$$\begin{aligned} [\alpha'_{i\sigma}, P_\beta] &= [\alpha_{i\sigma}, P_\beta] - [C_\alpha, P_\beta] = i\hbar(\delta_{\alpha\beta} - \delta_{\alpha\beta}) = 0 \\ [(p_\alpha)'_{i\sigma}, C_\beta] &= [(p_\alpha)_{i\sigma}, C_\beta] - \frac{1}{N}[P_\alpha, C_\beta] = -\frac{i\hbar}{N}(\delta_{\alpha\beta} - \delta_{\alpha\beta}) = 0, \end{aligned} \tag{2.98}$$

where $\alpha, \beta = x, y$, which also means that operators A and B that only depend on one of the two commute

$$[A(\mathbf{r}'_{i\sigma}, \mathbf{p}'_{j\sigma'}), B(\mathbf{C}, \mathbf{P})] = 0. \tag{2.99}$$

Now, using that

$$\sum_{i\sigma} r_{i\sigma}^2 = \sum_{i\sigma} (\mathbf{r}_{i\sigma} - \mathbf{C})^2 + NC^2 = \sum_{i\sigma} r_{i\sigma}'^2 + NC^2 \tag{2.100}$$

and

$$\sum_{i\sigma} p_{i\sigma}^2 = \sum_{i\sigma} (\mathbf{p}_{i\sigma} - \mathbf{P}/N)^2 + P^2/N = \sum_{i\sigma} p_{i\sigma}'^2 + P^2/N, \tag{2.101}$$

we indeed see that the Hamiltonian Eq.(2.41) splits into a center-of-mass part $H_{\text{c.m}}$ (Eq. (2.95)) and an internal part H_I

$$\begin{aligned} H_I &= H - H_{\text{c.m.}} \\ &= \sum_{\sigma=\uparrow,\downarrow} \sum_{i=1}^{N_\sigma} \left(\frac{p_{i\sigma}'^2}{2\mathcal{M}} + \frac{\mathcal{M}\omega^2}{2} r_{i\sigma}'^2 \right) - \Omega M_z^{(I)} + g \sum_{i=1}^{N_\uparrow} \sum_{j=1}^{N_\downarrow} \delta^{(2)} \left(\mathbf{r}'_{i\uparrow} - \mathbf{r}'_{j\downarrow} \right) \\ &= H_{\omega=0}^{(I)} + H_{\text{trap}}^{(I)} - \Omega M_z^{(I)}, \end{aligned} \tag{2.102}$$

where $H_{\omega=0}^{(I)} = \sum_{i\sigma} p'^2/2\mathcal{M} + g \sum_{i=1}^{N_\uparrow} \sum_{j=1}^{N_\downarrow} \delta^{(2)}(\mathbf{r}'_{i\uparrow} - \mathbf{r}'_{j\downarrow})$ is the internal Hamiltonian without a trap, and $H_{\text{trap}}^{(I)} = \sum_{i\sigma} \mathcal{M}\omega^2 r'^2/2$ the internal part of the harmonic trapping potential in Eq. (2.58). Before further discussing the internal part, we can rewrite the center-of-mass part in terms of the $Q_\pm$ operators by using Eqs. (2.69) and (2.70) as

$$\begin{aligned} Q_+^\dagger Q_+ + Q_-^\dagger Q_- = 2(Q_x^\dagger Q_x + Q_y^\dagger Q_y) &= \frac{P^2}{(\hbar\omega)\mathcal{M}} + \frac{N}{(\hbar\omega)}(N\mathcal{M})\omega^2 C^2 - 2N \\ &= 2N \left(\frac{H_{\text{c.m.}} - \Omega M_z^{(\text{c.m.})}}{\hbar\omega} - 1 \right), \end{aligned} \tag{2.103}$$

or equivalently

$$H_{\text{c.m.}} = \hbar\omega + \frac{\hbar\omega}{2N}(Q_+^\dagger Q_+ + Q_-^\dagger Q_-) - \Omega M_z^{(\text{c.m.})}. \tag{2.104}$$

In a similar manner, one has

$$\begin{aligned} -Q_+^\dagger Q_+ + Q_-^\dagger Q_- &= -2i\left(Q_y^\dagger Q_x - Q_x^\dagger Q_y\right) = -\frac{2N}{\hbar}\left(C_x P_y - C_y P_x\right) \\ &= -\frac{2N}{\hbar\Omega}\Omega M_z^{(\text{c.m.})}, \end{aligned} \tag{2.105}$$

which together with (2.104) reads

$$H_{\text{c.m.}} = \hbar\omega + \frac{1}{2N}\left(\hbar(\omega-\Omega)Q_+^\dagger Q_+ + \hbar(\omega+\Omega)Q_-^\dagger Q_-\right). \tag{2.106}$$

If one further defines $q_\pm = Q_\pm/\sqrt{2N}$ such that $[q_\pm, q_\pm^\dagger] = 1$, Eqs. (2.106) and (2.105) become

$$H_{\text{c.m.}} = \hbar\omega + \hbar(\omega-\Omega)q_+^\dagger q_+ + \hbar(\omega+\Omega)q_-^\dagger q_- \tag{2.107}$$

$$M_z^{(\text{c.m.})} = \hbar(q_+^\dagger q_+ - q_-^\dagger q_-), \tag{2.108}$$

which can be compared to the simple harmonic oscillator in Eq. (2.53), meaning that the center-of-mass part of the Hamiltonian $H_{\text{c.m.}}$ is the sum of two independent simple harmonic oscillators. As was discussed in Sec. 2.4.3, the $Q_+^\dagger$ ($Q_-^\dagger$) operator indeed increases the angular momentum of the center-of-mass position by 1 in the (opposite) direction of rotation Ω while increasing energy by $\hbar(\omega-\Omega)$ ($\hbar(\omega+\Omega)$). This can be seen in Fig. 2.5 and also in the results Sec. 4.1 when looking at the density. The center-of-mass part of the many-body wave function in (2.92) is then determined through $Q_+^{b+1}|a,b,c\rangle_P = Q_-^{c+1}|a,b,c\rangle_P = 0$. The results separate in $\Psi_{\text{c.m.}}(\mathbf{C}) = \Psi_{\text{c.m.}}(C)\Phi(C_\varphi)$ for $C = \sqrt{\mathbf{C}\cdot\mathbf{C}}$ and $C_\varphi = \arctan(C_y/C_x)$. For $b \geq c$ (c.f. (2.7) when $\mathcal{M} \to N\mathcal{M}$) we have the individually normalized parts

$$\Phi(C_\varphi) = \frac{e^{i(b-c)C_\varphi}}{\sqrt{2\pi}}, \tag{2.109}$$

and

$$\Psi_{\text{c.m.}}(C) = \frac{1}{\ell_{ho}}\sqrt{\frac{2N^{1+b-c}c!}{b!}}\left(\frac{C}{\ell_{ho}}\right)^{b-c} e^{-NC^2/(2\ell_{ho})} L_c^{b-c}\left(NC^2/\ell_{ho}^2\right), \tag{2.110}$$

where $L_c^{(b-c)}$ is a generalized Laguerre polynomial, and N the particle number. For $c \geq b$ exchange c and b. As discussed above, the center-of-mass degrees of freedom are decoupled from the internal dynamics and different primary states ($a = b = c = 0$) and their breathing mode excitations ($a \neq 0$, $b = c = 0$) for a fixed particle number N must thus share the same center-of-mass distribution $\Psi_{\text{c.m.}}(\mathbf{C})$.

To discuss the internal part of the Hamiltonian, it is useful to rewrite the generator of dilatations D in Eq. (2.48) in terms of center-of-mass and internal coordinates

$$\begin{aligned} D &= \frac{1}{2\hbar}\sum_{\sigma=\uparrow,\downarrow}\sum_{i=1}^{N_\sigma}\left((\mathbf{r}'_{i\sigma}+\mathbf{C})\cdot\left(\mathbf{p}'_{i\sigma}+\frac{\mathbf{P}}{N}\right)+\left(\mathbf{p}'_{i\sigma}+\frac{\mathbf{P}}{N}\right)\cdot(\mathbf{r}'_{i\sigma}+\mathbf{C})\right) \\ &= \frac{1}{2\hbar}\sum_{\sigma=\uparrow,\downarrow}\sum_{i=1}^{N_\sigma}(\mathbf{r}'_{i\sigma}\cdot\mathbf{p}'_{i\sigma}+\mathbf{p}'_{i\sigma}\cdot\mathbf{r}'_{i\sigma})+\frac{1}{2\hbar}(\mathbf{C}\cdot\mathbf{P}+\mathbf{P}\cdot\mathbf{C}) = D_I + D_{\text{c.m.}}, \end{aligned} \tag{2.111}$$

where $\sum_{i\sigma}\mathbf{r}'_{i\sigma} = \sum_{i\sigma}\mathbf{p}'_{i\sigma} = 0$ was used in going to the second line. Furthermore, note that one can write

$$\begin{aligned} \frac{1}{2N}\left(Q_+^\dagger Q_-^\dagger + Q_-^\dagger Q_+^\dagger\right) &= \frac{1}{N}\left(\left(Q_x^\dagger\right)^2+\left(Q_y^\dagger\right)^2\right) \\ &= \frac{i}{2\hbar}(\mathbf{C}\cdot\mathbf{P}+\mathbf{P}\cdot\mathbf{C})+\frac{P^2}{2(\hbar\omega)(N\mathcal{M})}-\frac{(N\mathcal{M})\omega^2C^2}{2(\hbar\omega)} \\ &= iD_{\text{c.m.}}+\frac{H^{(\text{c.m.})}_{\omega=0}}{(\hbar\omega)}-\frac{H^{(\text{c.m.})}_{\text{trap}}}{(\hbar\omega)}, \end{aligned} \tag{2.112}$$

with $D_{\text{c.m.}}$ denoting the center-of-mass part of the dilatation operator in Eq. (2.111), and $H^{(\text{c.m.})}_{\omega=0}$ and $H^{(\text{c.m.})}_{\text{trap}}$ parts of the center-of-mass Hamiltonian in Eq. (2.95). Thus, one can rewrite the internal breathing mode operator $R^\dagger$ in Eq. (2.76) using Eqs. (2.61), (2.111) and (2.112) as

$$\begin{aligned} R^\dagger &= L^\dagger - \frac{1}{2N}\left(Q_+^\dagger Q_-^\dagger + Q_-^\dagger Q_+^\dagger\right) \\ &= iD+\frac{H_{\omega=0}}{\hbar\omega}-\frac{H_{\text{trap}}}{\hbar\omega}-\left(iD_{\text{c.m.}}+\frac{H^{(\text{c.m.})}_{\omega=0}}{\hbar\omega}-\frac{H^{(\text{c.m.})}_{\text{trap}}}{\hbar\omega}\right) \\ &= iD_I+\frac{H^{(I)}_{\omega=0}}{\hbar\omega}-\frac{H^{(I)}_{\text{trap}}}{\hbar\omega}, \end{aligned} \tag{2.113}$$

to see that $R^\dagger$ indeed only acts on the internal coordinates. It is further useful to note that Eqs. (2.62)-(2.65) hold if one lets $D \to D_I$, $H_{\omega=0} \to H^{(I)}_{\omega=0}$, $H_{\text{trap}} \to H^{(I)}_{\text{trap}}$. Hence, one can rewrite Eqs. (2.77)-(2.79) as

$$[H_I, R^\dagger] = 2\hbar\omega R^\dagger, \tag{2.114}$$

$$[H_I, R] = -2\hbar\omega R, \tag{2.115}$$

$$[R^\dagger, R] = -\frac{4}{\hbar\omega}(H_I+\Omega M_z^{(I)}) = -\frac{4}{\hbar\omega}H_{I,\Omega=0}, \tag{2.116}$$

where we have introduced the notation $H_{I,\Omega=0} = H_I + \Omega M_z^{(I)}$ to denote the internal Hamiltonian without rotation (i.e. no angular momentum $M_z^{(I)}$). The use of this notation will shortly be useful, but first, we rewrite the generator T_3 in Eq. (2.88)

of the SO(2,1) group as

$$\begin{aligned} T_3 &= \frac{1}{2}\frac{(H+\Omega M_z)}{\hbar\omega} - \frac{1}{4N}\left(Q_+Q_+^\dagger + Q_-^\dagger Q_-\right) \\ &= \frac{1}{2}\frac{(H+\Omega M_z)}{\hbar\omega} - \frac{1}{4N}\left(2N + Q_+^\dagger Q_+ + Q_-^\dagger Q_-\right) \\ &= \frac{1}{2}\frac{(H+\Omega M_z)}{\hbar\omega} - \frac{1}{4N}\left(2N + 2N\left(\frac{H_{\text{c.m.}}+\Omega M_z}{\hbar\omega} - 1\right)\right) \\ &= \frac{1}{2}\frac{(H_I+\Omega M_z^{(I)})}{\hbar\omega} = \frac{1}{2}\frac{H_{I,\Omega=0}}{\hbar\omega}, \end{aligned} \tag{2.117}$$

where Eq. (2.73) was used in going to the second line, and Eq. (2.103) in going to the third line. Using Eq. (2.117) above for T_3 and computing the Casimir in Eq. (2.89), one obtains

$$\begin{aligned} T = 4(T_3^2 - T_2^2 - T_1^2) &= \frac{(H_I+\Omega M_z)^2}{(\hbar\omega)^2} - \frac{1}{2}\left(RR^\dagger + R^\dagger R\right) \\ &= \frac{H_{I,\Omega=0}^2}{(\hbar\omega)^2} - \frac{1}{2}\left(RR^\dagger + R^\dagger R\right). \end{aligned} \tag{2.118}$$

Evaluating the Casimir in this notation for a primary state $|P\rangle$ yields

$$\begin{aligned} T|P\rangle &= \frac{(H_I+\Omega M_z)^2}{(\hbar\omega)^2}|P\rangle - \frac{1}{2}\left([R,R^\dagger] + 2R^\dagger R\right)|P\rangle \\ &= \left(\frac{(E_{g,I}+\hbar\Omega M_g)^2}{(\hbar\omega)^2} - 2\frac{(E_{g,I}+\Omega\hbar M_g)}{(\hbar\omega)}\right)|P\rangle \\ &= \frac{(E_{g,I}+\hbar\Omega M_g)}{(\hbar\omega)}\left(\frac{(E_{g,I}+\hbar\Omega M_g)}{(\hbar\omega)} - 2\right)|P\rangle, \end{aligned} \tag{2.119}$$

where Eq. (2.116) was used in going to the second line, and $E_{g,I}$ denote the internal energy of a primary state. Compare Eq. (2.119) to (2.91) and note that the internal energy is $E_{g,I} = (E_g - \hbar\omega)$ with E_g denoting the energy of a primary state according to $H|P\rangle = E_g|P\rangle$. Also note that $(E_{g,I} + \hbar\Omega M_g)$ is the internal ground step energy without rotation $\Omega = 0$. Following [5, 6], we invert Eq. (2.119) (for $N > 1$, $E_g^{(0)} \geq 2\hbar\omega$) in order to obtain the ground step operator $H_{g,\Omega=0}$

$$H_{g,\Omega=0} = \hbar\omega + \hbar\omega\sqrt{T+1}, \tag{2.120}$$

relating a primary state to its energy without rotation $H_{g,\Omega=0}|P\rangle = (E_{g,I} + \hbar\Omega M_g)|P\rangle$. Since the Casimir T is constant within each conformal ladder (see Sec. 2.4.5), so is $H_{g,\Omega=0}$ ($[H_I, H_{g,\Omega=0}] = [R, H_{g,\Omega=0}] = [R^\dagger, H_{g,\Omega=0}] = 0$). Furthermore, one can express the Casimir T in terms of the ground step operator

$$T = \frac{H_{g,\Omega=0}}{(\hbar\omega)^2}\left(H_{g,\Omega=0} - 2\hbar\omega\right). \tag{2.121}$$

It is now instructive to introduce the rescaled internal breathing mode operators $R^\dagger$ and R

$$r = \sqrt{\frac{\hbar\omega}{2(H_{I,\Omega=0}+H_{g,\Omega=0})}}R, \quad r^\dagger = R^\dagger\sqrt{\frac{\hbar\omega}{2(H_{I,\Omega=0}+H_{g,\Omega=0})}}, \tag{2.122}$$

such that $[r, r^\dagger] = 1$. To see this, note that one can rewrite $RR^\dagger$ as

$$\begin{aligned} RR^\dagger &= \frac{1}{2}\left(RR^\dagger + R^\dagger R\right) + \frac{2H_{I,\Omega=0}}{\hbar\omega} = \frac{H_{I,\Omega=0}^2}{(\hbar\omega)^2} - T + \frac{2H_{I,\Omega=0}}{\hbar\omega} \\ &= \frac{(H_{I,\Omega=0} + H_{g,\Omega=0})}{(\hbar\omega)^2}\left(H_{I,\Omega=0} - H_{g,\Omega=0} + 2\hbar\omega\right), \end{aligned} \tag{2.123}$$

where Eq. (2.116) was used for the first equality, Eq. (2.118) for the second equality, and Eq. (2.121) in going to the last line. In a completely analogous way, one has

$$R^\dagger R = \frac{(H_{I,\Omega=0} - H_{g,\Omega=0})}{(\hbar\omega)^2}\left(H_{I,\Omega=0} + H_{g,\Omega=0} - 2\hbar\omega\right) \tag{2.124}$$

Hence, $rr^\dagger$ can be written as

$$\begin{aligned} rr^\dagger &= \frac{\hbar\omega}{2}\left(H_{I,\Omega=0} + H_{g,\Omega=0}\right)^{-1/2} RR^\dagger \left(H_{I,\Omega=0} + H_{g,\Omega=0}\right)^{-1/2} \\ &= \frac{1}{2\hbar\omega}\left(H_{I,\Omega=0} - H_{g,\Omega=0}\right) + 1, \end{aligned} \tag{2.125}$$

where Eq. (2.123) was used in going to the second line. For $r^\dagger r$, the situation is somewhat more complicated. Before evaluating $r^\dagger r$, we introduce the relations for operators A and B

$$\frac{1}{A} = \int_0^\infty e^{-sA} ds, \tag{2.126}$$

and the Baker-Hausdorff lemma [32]

$$e^A B e^{-A} = \sum_{n=0}^{\infty} \frac{G_n}{n!}, \tag{2.127}$$

with $G_0 = B$ and for $n > 1$ $G_n = [A, G_{n-1}]$. Evaluating $r^\dagger r$ now yield

$$\begin{aligned} r^\dagger r &= \frac{\hbar\omega}{2} R^\dagger \left(H_{I,\Omega=0} + H_{g,\Omega=0}\right)^{-1} R = \frac{\hbar\omega}{2}\int_0^\infty ds\, R^\dagger e^{-s(H_{I,\Omega=0}+H_{g,\Omega=0})} R \\ &= \frac{\hbar\omega}{2}\int_0^\infty ds\, e^{-s(H_{I,\Omega=0}+H_{g,\Omega=0})}\left(e^{sH_{I,\Omega=0}} R^\dagger e^{-sH_{I,\Omega=0}}\right) R \\ &= \frac{\hbar\omega}{2}\int_0^\infty ds\, e^{-s(H_{I,\Omega=0}+H_{g,\Omega=0}-2\hbar\omega)} R^\dagger R \\ &= \frac{\hbar\omega}{2}\left(H_{I,\Omega=0} + H_{g,\Omega=0} - 2\hbar\omega\right)^{-1} R^\dagger R = \frac{1}{2\hbar\omega}\left(H_{I,\Omega=0} - H_{g,\Omega=0}\right), \end{aligned} \tag{2.128}$$

where Eq. (2.126) was used for the second equality, and Eq. (2.127) together with $[H_{I,\Omega=0}, R^\dagger] = 2\hbar\omega R^\dagger$ in going to the third line, and Eq. (2.124) for the last equality. Thus, we see that

$$[r, r^\dagger] = rr^\dagger - r^\dagger r = \frac{1}{2\hbar\omega}\left(H_{I,\Omega=0} - H_{g,\Omega=0}\right) + 1 - \frac{1}{2\hbar\omega}\left(H_{I,\Omega=0} - H_{g,\Omega=0}\right) = 1. \tag{2.129}$$

We are now in a position to express the internal Hamiltonian in terms of the ground step operator $H_{g,\Omega=0}$ and the rescaled internal breathing mode operator r as

$$H_I = H_{g,\Omega=0} - \Omega M_z^{(I)} + 2\hbar\omega r^\dagger r = \hbar\omega + \hbar\omega\sqrt{T+1} - \Omega M_z^{(I)} + 2\hbar\omega r^\dagger r, \tag{2.130}$$

and one can see that $r^\dagger$ (or $R^\dagger$) indeed create internal excitations at energy $2\hbar\omega$ (c.f. to Eq. (2.53)). Using Eqs. (2.130) and (2.107), the total Hamiltonian of the rotating two-dimensional interacting Fermi gas can be expressed as

$$\begin{aligned} H &= H_I + H_{\text{c.m.}} \\ &= 2\hbar\omega + \hbar\omega\sqrt{T+1} - \Omega M_z^{(I)} + 2\hbar\omega r^\dagger r + \hbar(\omega-\Omega)q_+^\dagger q_+ + \hbar(\omega+\Omega)q_-^\dagger q_-, \end{aligned} \tag{2.131}$$

and the total angular momentum as

$$M_z = M_z^{(I)} + M_z^{(\text{c.m.})} = M_z^{(I)} + \hbar(q_+^\dagger q_+ - q_-^\dagger q_-). \tag{2.132}$$

Creating an energy eigenstate $|a,b,c\rangle_P$ with the rescaled operators r and $q_\pm$ now produce a state $|a,b,c\rangle_P = (r^\dagger)^a (q_+^\dagger)^b (q_-^\dagger)^c |P\rangle$ that obey

$$r^\dagger r |a,b,c\rangle_P = a|a,b,c\rangle_P, \tag{2.133}$$

$$q_+^\dagger q_+ |a,b,c\rangle_P = b|a,b,c\rangle_P, \tag{2.134}$$

$$q_-^\dagger q_- |a,b,c\rangle_P = c|a,b,c\rangle_P. \tag{2.135}$$

Such a state has energy $E = E_{\text{c.m.}} + E_I$, with

$$E_{\text{c.m.}} = \hbar\omega + \hbar(\omega-\Omega)b + \hbar(\omega+\Omega)c, \tag{2.136}$$

and

$$E_I = \hbar\omega + \hbar\omega\sqrt{\langle T\rangle + 1} - \hbar\Omega M_g + 2\hbar\omega a = E_g - \hbar\omega + 2\hbar\omega a, \tag{2.137}$$

where $E_g = 2\hbar\omega + \sqrt{\langle T\rangle + 1} - \hbar\Omega M_g$ is the ground step energy such that

$$E = E_I + E_{\text{c.m.}} = E_g + 2\hbar\omega a + \hbar(\omega-\Omega)b + \hbar(\omega+\Omega)c, \tag{2.138}$$

in accordance with Eq. (2.83). The angular momentum is

$$\langle M_z\rangle = \hbar(M_g + b - c), \tag{2.139}$$

also in accordance with Eq. (2.84). Hence, from the Hamiltonian in Eq. (2.131), and the above discussion, one can see that the properties of a primary state are completely determined by the internal dynamics. The energy is determined by the Casimir $\langle T\rangle$ (Eq. (2.91) to leading order in perturbation theory) and the ground step (internal) angular momentum M_g.

The hyperradial part $F(\tilde{R})$ of the many-body wave function in Eq. (2.92) for a state can now be determined by $R^{a+1}|a,b,c\rangle_P = 0$ which yields [5, 6, 29]

$$F(\tilde{R}) = \frac{1}{\ell_{ho}}\sqrt{\frac{2a!}{\Gamma(s+a+1)}}\left(\frac{\tilde{R}}{\ell_{ho}}\right)^s e^{-\tilde{R}^2/(2\ell_{ho})} L_a^s\left(\tilde{R}^2/\ell_{ho}^2\right), \tag{2.140}$$

where Γ is the gamma function, and $L_a^{(s)}$ a generalized Laguerre polynomial. Furthermore, $s = \sqrt{\langle T\rangle + 1}$, with $\langle T\rangle$ being the expectation of the Casimir operator

in Eq. (2.89). Note that s also parametrize the non-interacting ground step energy without rotation as $E^{(0)}_{g,\Omega=0} = E^{(0)}_g + \hbar\Omega M_g = \hbar\omega(s+2)$ (see Eq. (2.131)), or the non-interacting internal energy without rotation as $E^{(0)}_I + \hbar\Omega M_g = \hbar\omega(s+1)$ (in Eq. (2.130)), where M_g is the ground step (internal) angular momentum. The hyperradial distribution is normalized according to

$$\int d\tilde{R}\tilde{R}F(\tilde{R})^2 = 1. \tag{2.141}$$

Furthermore, observe that the hyperradial distribution in Eq. (2.140) only depends on the Casimir $\langle T\rangle$, or the ground step energy E_g, and the number of breathing mode excitations a. To leading order in perturbation theory, this means that states originating from primary states at the same non-interacting energy level without rotation $E^{(0)}_{g,\Omega=0}$, with an equal number of breathing mode excitations a must share the same distribution, completely independent of the number of the center-of-mass excitations b and c!

We argue that the hyperradial distribution $F(\tilde{R})$ and the microscopic origin of the conformal symmetry is testable experimentally in ultracold atomic gases by sampling the many-body wave function with recently developed single-particle imaging techniques [12, 13, 31]. By taking many snapshots of the particle configurations and subtracting the center-of-mass position, the hyperradial coordinate can be computed and histograms should reveal the hyperradial distribution. In this thesis, the hyperradial distribution is computed with Monte Carlo simulations discussed in Sec. 3.3, and the results confirming the predictions in (2.140) can be seen in the Sec. 4.3.

2.6 Density: Observing Excitations

Having discussed the consequences of nonrelativistic conformal symmetry on the system, this section will discuss how it can be observed experimentally in the density [41].

The density operator in position space is

$$n(\mathbf{r}) = \sum_{i=\uparrow,\downarrow}\sum_{i=1}^{N_\sigma}\delta^{(2)}(\mathbf{r}_{i\sigma} - \mathbf{r}), \tag{2.142}$$

which can be written in occupation number representation

$$n = \sum_{\sigma=\uparrow\downarrow}\sum_{i,j}\psi^*_i(\mathbf{r})\psi_j(\mathbf{r})c^\dagger_{i\sigma}c_{j\sigma}, \tag{2.143}$$

where $i = \{n_i, m_i\}$ and the single-particle wave functions $\psi_i(\mathbf{r})$ are given in Eq. (2.7). Now, to observe a time dependence in the density one cannot look at an energy eigenstate $H|\Psi_s\rangle = E_s|\Psi_s\rangle$ alone since it is stationary: using Eq. (2.2),

$$\langle n(\mathbf{r})\rangle = \langle\Psi_s(t)|n|\Psi_s(t)\rangle = \langle\Psi_s|e^{iE_st/\hbar}ne^{-iE_st/\hbar}|\Psi\rangle = \langle\Psi_s|n|\Psi\rangle. \tag{2.144}$$

However, considering a superposition of stationary states instead, such as the ground state $H|\Psi_{\rm gs}\rangle = E_{\rm gs}|\Psi_{\rm gs}\rangle$ and the first excited state with the internal breathing mode operator $HR^\dagger|\Psi_{\rm gs}\rangle = (E_{\rm gs}+2\hbar\omega)R^\dagger|\Psi_{\rm gs}\rangle$, the density will pick up a time dependence. Denoting $|\Psi_{R^\dagger}\rangle = R^\dagger|\Psi_{\rm gs}\rangle$ and $|\Psi\rangle = |\Psi_{\rm gs}\rangle + |\Psi_{R^\dagger}\rangle$, one has

$$\begin{aligned}\langle n(\mathbf{r},t)\rangle &= \langle\Psi(t)|n|\Psi(t)\rangle = \left(\langle\Psi_{R^\dagger}|e^{2i\omega t} + \langle\Psi_{\rm gs}|\right) e^{iE_{\rm gs}t/\hbar} n e^{-iE_{\rm gs}t/\hbar}(|\Psi_{\rm gs}\rangle + e^{-2i\omega t}|\Psi_{R^\dagger}\rangle) \\ &= \langle\Psi_{\rm gs}|n|\Psi_{\rm gs}\rangle + \langle\Psi_{R^\dagger}|n|\Psi_{R^\dagger}\rangle + 2\cos(2\omega t)\,\langle\Psi_{R^\dagger}|n|\Psi_{\rm gs}\rangle,\end{aligned} \tag{2.145}$$

where we have used that n is a Hermitian operator in going to the second line. Thus, the density will be time dependent and periodic with a period of π/ω. As is illustrated in the results in Sec. 4.1, this corresponds to the undamped breathing mode oscillations of the gas at a frequency exactly twice the trapping frequency 2ω. An identical calculation can be made but considering the first excited states with the center-of-mass excitations $Q_\pm^\dagger$. Denoting $|\Psi_{Q_\pm^\dagger}\rangle = Q_\pm^\dagger|\Psi_{\rm gs}\rangle$ and $|\Psi\rangle = |\Psi_{\rm gs}\rangle + |\Psi_{Q_\pm^\dagger}\rangle$, one has

$$\begin{aligned}\langle n(\mathbf{r},t)\rangle &= \langle\Psi(t)|n|\Psi(t)\rangle \\ &= \langle\Psi_{\rm gs}|n|\Psi_{\rm gs}\rangle + \langle\Psi_{Q_\pm^\dagger}|n|\Psi_{Q_\pm^\dagger}\rangle + 2\cos((\omega\mp\Omega)t)\,\langle\Psi_{Q_\pm^\dagger}|n|\Psi_{\rm gs}\rangle,\end{aligned} \tag{2.146}$$

where now the time dependence has a period of $2\pi/(\omega-\Omega)$. This corresponds to stirring the center-of-mass position of the gas in either the direction of the rotation Ω (Q_+) or the opposite direction (Q_-). The next section will further discuss how such superpositions can be prepared experimentally.

2.7 Inducing Transition Between States

This section will discuss how transitions between states can be induced by modulating parameters that are experimentally accessible.

According to Fermi's golden rule, the transition rate between two states is proportional to the transition matrix element [32]

$$\Gamma^{f\leftarrow i} = |\langle f|\Gamma|i\rangle|^2, \tag{2.147}$$

where $|i\rangle$, $|f\rangle$ denote the initial and final state respectively, and Γ is the transition matrix due to an applied perturbation. Furthermore, since this thesis calculates all energy eigenstates exactly to first order in perturbation theory, we can also look at the density $\langle n(\mathbf{r},t)\rangle$ of the excited state $|\Psi_\Gamma\rangle$, induced by the transition matrix Γ

$$|\Psi_\Gamma\rangle = \Gamma|i\rangle = \sum_j \langle\Psi_j|\Gamma|i\rangle|\Psi_j\rangle = \sum_k \langle f_k|\Gamma|i\rangle|f_k\rangle, \tag{2.148}$$

where a complete set $1 = \sum_j |\Psi_j\rangle\langle\Psi_j|$ was inserted to the left of Γ, and $\sum_k |f_k\rangle$ only denotes states that have non-zero overlap with $\Gamma|i\rangle$. Since one prepares the ground state with N particles experimentally [11–13], we will only show results for an initial ground state $|i\rangle = |\Psi_{\rm gs}\rangle$. However, the calculations that follow are valid for any initial state.

2.7.1 Anisotropic Frequency Perturbation

One way to induce a transition between states is to experimentally perturb the trapping frequency anisotropically ω_x (or ω_y), which before the perturbation is isotropic with $\omega_x = \omega_y = \omega$. The resulting transition matrix Γ_{ω_x} is

$$\Gamma_{\omega_x} = H_{\omega_x \to \omega + \delta\omega_x} - H = \delta\omega_x \omega \mathcal{M} \sum_{\sigma=\uparrow,\downarrow} \sum_{i=1}^{N_\sigma} x_{i\sigma}^2 + \mathcal{O}(\delta\omega_x^2), \tag{2.149}$$

where H is the Hamiltonian in Eq. 2.41, and we will ignore higher-order terms $\mathcal{O}(\delta\omega_x^2)$. This perturbation corresponds to inducing a so-called scissors mode in the gas [42, 43], as can be seen in the oscillations of the gas in the results section 4.4.1. In occupation number representation, Eq. (2.149) is a single-particle operator that reads

$$\Gamma_{\omega_x} = \sum_{\sigma} \sum_{i,j} \langle \psi_i | \gamma_{\omega_x} | \psi_j \rangle c_{i\sigma}^\dagger c_{j\sigma} \tag{2.150}$$

with single-particle matrix elements

$$\langle \psi_i | \gamma_{\omega_x} | \psi_j \rangle = \hbar\delta\omega_x \int_0^{2\pi} d\varphi \int r dr \, \psi_i^*(r,\varphi) \frac{r^2}{4} \left(e^{i\varphi} + e^{-i\varphi} \right)^2 \psi_i(r,\varphi), \tag{2.151}$$

where we have rewritten $x = r(e^{i\varphi} + e^{-i\varphi})/2$ in polar coordinates. Using the single-particle wave function in Eq. (2.7) and carrying out the angular integration gives three non-zero possibilities: $m_i = m_j$, $m_i = m_j + 2$, or $m_i = m_j - 2$. In other words, Γ_{ω_x} only connect states with equal total angular momentum $\Delta M = 0$ or differing by two $\Delta M = \pm 2$. Details of the analytical expression for the single-particle matrix elements in Eq. (2.151) can be found in appendix A.2. Here, we only summarize the result:

An anisotropic perturbation Γ_{ω_x} in the trapping frequency $\delta\omega_x$ can only leave the angular momentum unchanged $\Delta M = 0$ or change it by $\Delta M = \pm 2$. If we consider a non-degenerate ground state, we find that when Γ_{ω_x} leaves angular momentum unchanged, $\Delta M = 0$, it will only connect the ground state to either itself or to states at the non-interacting excitation level $\Delta E_N^{(0)} = 2\hbar\omega$ (see Eq. (2.33)). Further, when Γ_{ω_x} changes angular momentum by $\Delta M = 2$, it connects the non-degenerate ground state to states at the non-interacting excitation level $\Delta E^{(0)} = 2\hbar(\omega - \Omega)$. Similarly, changing $\Delta M = -2$ connects to $\Delta E^{(0)} = 2\hbar(\omega + \Omega)$, but also to $\Delta E^{(0)} = 2\hbar\Omega$.

2.7.2 Trap Center Perturbation

Another way to induce transitions between states is to experimentally perturb the trap center δx_0, resulting in a transition matrix Γ_{x_0}

$$\Gamma_{x_0} = H_{x_0 \to x_0 - \delta x_0} - H = \delta x_0 w^2 \mathcal{M} \sum_{\sigma=\uparrow,\downarrow} \sum_{i=1}^{N_\sigma} x_{i\sigma} + \mathcal{O}(\delta x_0^2) \tag{2.152}$$

where H is the Hamiltonian in Eq. 2.41, and we will ignore higher-order terms $\mathcal{O}(\delta x_0^2)$. Equation (2.152) is a single-particle operator that reads in occupation

number representation

$$\Gamma_{x_0} = \sum_\sigma \sum_{i,j} \langle \psi_i | \gamma_{x_0} | \psi_j \rangle c^\dagger_{i\sigma} c_{j\sigma} \tag{2.153}$$

with single-particle matrix elements

$$\langle \psi_i | \gamma_{x_0} | \psi_j \rangle = \hbar\omega \frac{\delta x_0}{\ell_{ho}} \int_0^{2\pi} d\varphi \int r dr\, \psi_i^*(r,\varphi) \frac{r}{2} \left(e^{i\varphi} + e^{-i\varphi} \right) \psi_i(r,\varphi), \tag{2.154}$$

where we have rewritten $x = r(e^{i\varphi} + e^{-i\varphi})/2$ in polar coordinates. Again, using the single-particle wave function in Eq. (2.7) and carrying out the angular integral give only two non-zero possibilities: $m_i = m_j \pm 1$. In other words, Γ_{ω_x} only connects states that differ by one unit of angular momentum $\Delta M = \pm 1$. Details of the analytical expression for the single-particle matrix elements in Eq. (2.154) can be found in appendix A.3. However, if we consider a ground state, we see that Γ_{x_0} only connects to states with $\Delta E^{(0)} = 2\hbar(\omega \mp \Omega)$.

Another interesting property of Γ_{x_0} is that Eq. (2.152) can be rewritten in terms of center-of-mass operators $Q_\pm$ using Eqs. (2.69) and (2.70) as

$$\Gamma_{x_0} = \delta x_0 w^2 N \mathcal{M} C_x = \hbar\omega \frac{\delta x_0}{\ell_{ho}} \frac{i}{\sqrt{2}} \left(Q_x - Q_x^\dagger \right) = \hbar\omega \frac{\delta x_0}{\ell_{ho}} \frac{i}{2\sqrt{2}} \left(Q_+ + Q_+^\dagger + Q_- + Q_-^\dagger \right), \tag{2.155}$$

which means that Γ_{x_0} will only act on the center of mass, in particular only connect states within the same conformal tower (see Fig. 2.5)!

2.7.3 Isotropic Trap Frequency Perturbation

A third way of inducing transitions between states is to experimentally perturb the trapping frequency isotropically $\omega \to \omega + \delta\omega$. This results in a transition matrix Γ_ω

$$\Gamma_\omega = H_{\omega \to \omega + \delta\omega} - H = 2\delta\omega\omega\mathcal{M} \sum_{\sigma=\uparrow,\downarrow} \sum_{i=1}^{N_\sigma} r_{i\sigma}^2 + \mathcal{O}(\delta\omega_x^2), \tag{2.156}$$

where H is the Hamiltonian in Eq. (2.41), and we ignore higher order terms $\mathcal{O}(\delta\omega^2)$. This perturbation corresponds to inducing breathing modes in the gas [41, 44], as can be seen in the oscillations of the gas in the results Sec. 4.4.3. Equation (2.156) is a single-particle operator and reads in occupation number representation,

$$\Gamma_\omega = \sum_\sigma \sum_{i,j} \langle \psi_i | \gamma_\omega | \psi_j \rangle c^\dagger_{i\sigma} c_{j\sigma} \tag{2.157}$$

with single-particle matrix elements

$$\langle \psi_i | \gamma_\omega | \psi_j \rangle = \hbar\delta\omega \int_0^{2\pi} d\varphi \int r dr\, \psi_i^*(r,\varphi) r^2 \psi_i(r,\varphi). \tag{2.158}$$

Yet again, using the single-particle wave function in Eq. (2.7) and carrying out the angular part gives only one non-zero possibility: $m_i = m_j$. In other words, Γ_ω

conserve angular momentum $\Delta M = 0$. The result of the matrix elements in Eq. (2.158) is stated below

$$\begin{aligned}\langle\psi_i|\gamma_{\delta\omega}|\psi_j\rangle = (\hbar\delta\omega)2\delta_{m_i,m_j}\Big((2n_i+|m_i|+1)\delta_{n_i,n_j} \\ -\sqrt{(n_i+|m_i|+1)(n_i+1)}\delta_{n_i,n_j-1} \\ -\sqrt{n_i(n_i+|m_i|)}\delta_{n_i,n_j+1}\Big).\end{aligned} \tag{2.159}$$

If we consider a non-degenerate ground state, we see that Γ_{ω_x} only connects to states with $\Delta E^{(0)} = 2\hbar\omega$, or with itself, $\Delta E^{(0)} = 0$. Again, another interesting property of Γ_ω is that Eq. (2.152) can be rewritten in terms of center-of-mass operators $Q_\pm$, and the internal breathing mode operator R using Eq. (2.61) and (2.76) as

$$\begin{aligned}\Gamma_\omega &= 2\frac{\delta\omega}{\omega}H_{\text{trap}} = \frac{\delta\omega}{\omega}(H+\Omega M_z) - \frac{\hbar\delta\omega}{2}\left(L^\dagger + L\right) \\ &= \frac{\delta\omega}{\omega}(H+\Omega M_z) - \frac{\hbar\omega}{2}\left(R^\dagger + R + \frac{1}{N}\left(Q_+Q_- + Q_-^\dagger Q_+^\dagger\right)\right),\end{aligned} \tag{2.160}$$

meaning that Γ_ω excites both internal breathing modes, and one center-of-mass excitation in each direction such that angular momentum is conserved. Furthermore, since it is composed of the Hamiltonian H, the total angular momentum M_z, and the spectrum-generating operators, Γ_ω will only connect states within the same conformal tower (see Fig. 2.5 again)!

2.7.4 Interaction Strength Perturbation

The last way of inducing transitions between states discussed in this thesis is to perturb the interaction strength $g \to g + \delta g$.

$$\Gamma_g = H_{g\to g+\delta g} - H = \delta g \sum_{i=1}^{N_\uparrow}\sum_{i=1}^{N_\downarrow}\delta^{(2)}(\mathbf{r}_{i\uparrow} - \mathbf{r}_{i\downarrow}), \tag{2.161}$$

which is the interaction part of the Hamiltonian in Eq. (2.41). It is a two-particle operator in occupation number representation and its matrix elements are discussed in appendix A.1. However, Γ_g conserves angular momentum and, in contrast to the other transition matrices introduced previously, connects states at arbitrary non-interacting energy levels. Yet, we know from Sec. 2.4.3 and 2.5 that the interaction operator only affects the internal dynamics. This means that Γ_g connects states to internal breathing mode excitations, but also states between different conformal towers.

3
Methods

The methods section will first discuss how the energy eigenstates of the interacting many-body Hamiltonian are computed exactly within degenerate perturbation theory. Next, once the eigenstates can be computed, the classification process of primary states and their conformal towers $|a, b, c\rangle_P$ according to Eq. (2.82) will be discussed, such that the nonrelativistic conformal invariance can be confirmed. Last, Metropolis Monte Carlo simulations of the many-body wave function are discussed in order to confirm the analytical prediction of the hyperradial distribution.

3.1 Exact Diagonalistion With Degenerate Perturbation Theory

Here, the diagonalization procedure using degenerate perturbation theory is discussed. Since the conformal symmetry is only expected to hold for weak interactions due to quantum anomaly as discussed in Sec. 2.3.1, leading order perturbation theory in the interaction strength g suffices.

In an ultracold environment, fermions occupy the lowest-energy single-particle states possible, where every state is maximally occupied by one identical fermion due to the Pauli principle. The rotating two-dimensional harmonic oscillator has degenerate single-particle levels for $\Omega/\omega \in j/k$,$j, k \in \mathcal{N}$, as discussed in Sec. 2.1.2. This means that even the ground state is degenerate, except for closed-shell configurations. For a non-rotating trap, where the l^{th} level is $(l + 1)$-fold degenerate, these closed-shell configurations are $N = 2, 6, 12, 20, ...$, where we have included the two spin components in the consideration. A degenerate ground state for $N = 8$ and $\Omega = 1/2$ is illustrated in Fig. 3.1. To leading order in degenerate perturbation theory, one collects all states $\{|\Psi_k\rangle\}$ with equal noninteracting energy $E_N^{(0)}$ in (2.33) (see Fig. 3.1 for an example), and diagonalizes the interacting Hamiltonian in Eq. (2.41) [32]

$$H_{kl} = \langle\Psi_k|H|\Psi_l\rangle, \tag{3.1}$$

from which one obtains the first-order energy corrections $E_N^{(1)} \sim \mathcal{O}(g)$ with energy eigenvalues

$$E_N = E_N^{(0)} + E_N^{(1)}. \tag{3.2}$$

Now, to this order in perturbation theory, the scale invariance discussed in section 2.4.3 follows from the homogeneity of the delta function $\delta^{(2)}(\lambda\mathbf{r}) = \delta(\mathbf{r})/\lambda^2$ in the matrix elements in Eq. (3.1). Note, however, that the second-order correction to

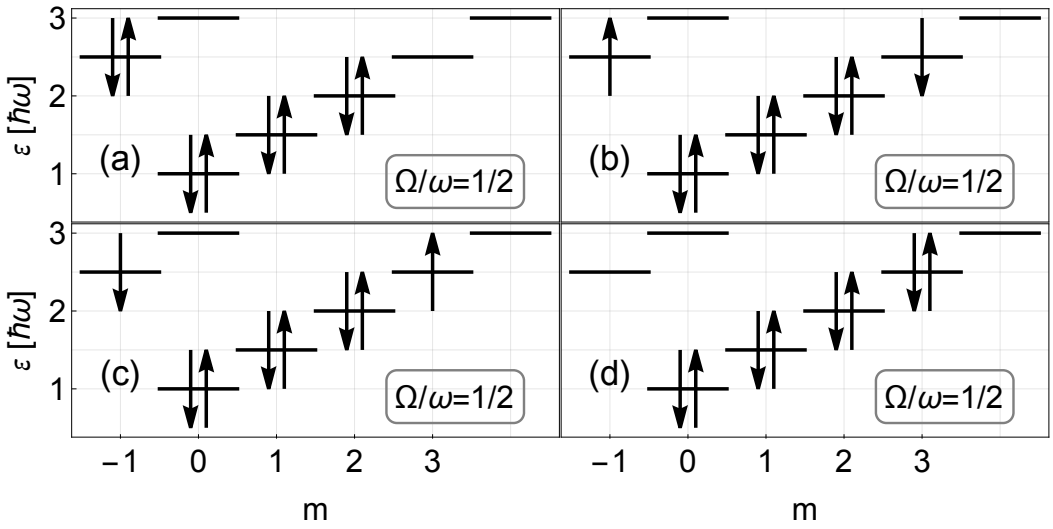

Figure 3.1: (a)-(d) Illustration of the four-fold degenerate ground state for $N = 8$ and $\Omega = 1/2$. Arrows indicate the spin projection $\sigma = \pm 1/2$.

the energy includes a diverging sum which leads to an energy cutoff dependence that breaks scale invariance [32].

We compute the eigenstates within degenerate perturbation theory in two ways. One way includes the Casimir operator from Eq. (2.89) which disentangles states belonging to different conformal towers originating from different non-interacting energy level $E_N^{(0)}$. However, this is computationally demanding because to compute the Casimir at non-interacting energy level $E_N^{(0)}$, one must compute $R^\dagger$ at level $E_N^{(0)} + 2\hbar\omega$ and $Q_\pm^\dagger$ at level $E_N^{(0)} + 2(\hbar\omega \mp \Omega)$. The reason is that the Casimir operator T includes products in the form of $RR^\dagger$ and the matrix elements of the individual operators are obtained by inserting a completeness relation $\sum_i |\Psi_i\rangle\langle\Psi_i|$ between them. Then the first operator $R^\dagger$ will act on a state $|\Psi_k\rangle$ with energy $E_N^{(0)}$, connecting it to states at level $E_N^{(0)} + 2\hbar\omega$, after which R acts on the state $R^\dagger|\Psi_k\rangle$ connecting it back to states at level $E_N^{(0)}$. The dimensionality of the degenerate subspace becomes large quickly with excitation level and particle number.

We further include the following commuting operators in the diagonalization: the total angular momentum M_z in Eq (2.57), the Casimir operator T in Eq. (2.89), and the total spin operator

$$S^2 = \sum_{i\sigma}^{N_\sigma} (\mathbf{S}_{i\sigma})^2 = \sum_{i\sigma}\sum_{j\sigma'} \mathbf{S}_{i\sigma} \cdot \mathbf{S}_{j\sigma'}, \tag{3.3}$$

which in occupation number representation takes the form [33]

$$S^2 = \frac{1}{2}\sum_{i\sigma} n_{i\sigma} + \frac{1}{4}\sum_{i,j} (n_{i\uparrow} - n_{i\downarrow})(n_{j\uparrow} - n_{j\downarrow}) - \sum_{i,j} c_{i\uparrow}^\dagger c_{j\downarrow}^\dagger c_{i\downarrow} c_{j\uparrow}. \tag{3.4}$$

The matrix that is diagonalized is thus $\tilde{H}$ with elements

$$\tilde{H}_{kl} = \langle\Psi_k|\alpha H + \beta M_z + \gamma S^2 + \epsilon T|\Psi_l\rangle, \tag{3.5}$$

where $\alpha, \beta, \gamma, \epsilon$ are numbers chosen such that $\tilde{H}_{kl}$ do not have accidentally repeated eigenvalues. In this way, the eigenvectors obtained are simultaneously eigenvectors of H with eigenvalue E_N in Eq. (3.2), M_z with eigenvalue $\hbar M$, S^2 with eigenvalue $S(S+1)$, and T with eigenvalue in Eq. (2.91).

The second way we compute the energy eigenstates, which speeds up the diagonalization, is to set $\epsilon = 0$ in (3.5). In this way, the Casimir operator is not computed and diagonalization only includes operators that are computed at level $E_N^{(0)}$. Now the problem is that states between different conformal towers are not disentangled, which will be discussed in the following section.

3.2 Classifying Primary States and Their Conformal Towers

This section discusses how we classify the states $|a,b,c\rangle_P$ with P denoting the primary state $|P\rangle$ of a conformal tower (see Fig. 2.5) with the quantum numbers (a,b,c) that denote the internal breathing mode and center-of-mass excitations according to Eq. (2.82).

The diagonalization procedure described in the previous section provides us with eigenstates of the Hamiltonian H in Eq. (2.41), the total spin S^2 in Eq. (3.3), the total angular momentum M_z in Eq. (2.57), and of the Casimir T in Eq. (2.89) depending on if it is included or not. In either case, since multiple states may share the same eigenvalues of H, S^2, M_z, and T, the eigenspace of some eigenvalues is degenerate. An example is given below:

- Consider $|1,0,0\rangle_P$=$R^\dagger|P\rangle$ and $|0,1,1\rangle_P$=$Q_+^\dagger Q_-^\dagger|P\rangle$, both originating from the same primary state (see Fig. 2.5). This means that

$$H|1,0,0\rangle_P = (E_g + 2\hbar\omega)|1,0,0\rangle_P, \tag{3.6}$$
$$M_z|1,0,0\rangle_P = \hbar M_g|1,0,0\rangle_P, \tag{3.7}$$
$$S^2|1,0,0\rangle_P = S_g(S_g+1)|1,0,0\rangle_P, \tag{3.8}$$
$$T|1,0,0\rangle_P = \left(\frac{E_g^{(0)} + \hbar\Omega M_g}{\hbar\omega} - 1\right)\left(\frac{E_g^{(0)} + \hbar\Omega M_g}{\hbar\omega} - 3\right)|1,0,0\rangle_P, \tag{3.9}$$

  where E_g ($E_g^{(0)}$), M_g and S_g denote the (non-) interacting energy, angular momentum, and spin of the primary state $|P\rangle$. Here we have used that that $Q_\pm^\dagger$ and $R^\dagger$ cannot change the spin, and the Casimir T is evaluated to leading order in perturbation theory according to Eq. (2.91). Likewise for $|0,1,1\rangle_P$

$$H|0,1,1\rangle_P = (E_g + 2\hbar\omega)|0,1,1\rangle_P, \tag{3.10}$$
$$M_z|0,1,1\rangle_P = \hbar M_g|0,1,1\rangle_P, \tag{3.11}$$
$$S^2|0,1,1\rangle_P = S_g(S_g+1)|0,1,1\rangle_P, \tag{3.12}$$
$$T|0,1,1\rangle_P = \left(\frac{E_g^{(0)} + \hbar\Omega M_g}{\hbar\omega} - 1\right)\left(\frac{E_g^{(0)} + \hbar\Omega M_g}{\hbar\omega} - 3\right)|0,1,1\rangle_P, \tag{3.13}$$

meaning that $|1,0,0\rangle_P$ and $|0,1,1\rangle_P$ together span a degenerate eigenspace of Eq. (3.5). Thus, any linear combination of the two is an eigenvector of the matrix in Eq. (3.5) with the same eigenvalue.

The reason why this is important is because of the way we classify a state $|a,b,c\rangle_P$. Consider an eigenvector $|\Psi_1\rangle$ of the matrix in Eq. (3.5), then the numbers (a,b,c) are assigned through

$$R^{a+1}|\Psi_1\rangle = 0, \quad Q_+^{b+1}|\Psi_1\rangle = 0, \quad Q_-^{c+1}|\Psi_1\rangle = 0. \tag{3.14}$$

Referring to the example above, since some eigenvalues are degenerate, a state $|\Psi_1\rangle = \alpha_1|1,0,0\rangle_P + \alpha_2|0,1,1\rangle_P$ for any coefficients α_1, α_2 is also an eigenvector. The classification according to Eq. (3.14) would in this case give

$$R^2|\Psi_1\rangle = 0, \quad Q_+^2|\Psi_1\rangle = 0, \quad Q_-^2|\Psi_1\rangle = 0, \tag{3.15}$$

resulting in $|1,1,1\rangle_P$, which is wrong. For this reason, we employ the following procedure in obtaining the correct eigenstates:

First, notice that all eigenstates at the lowest non-interacting energy level $E_N^{(0)}$ for any number of particles N are primary states. Thus, in the case when the Casimir T is included in the diagonalization in Eq. (3.5), we can compute the eigenstates at excitation level lv as follows:

- Compute the eigenstates of the matrix in Eq. (3.5) at the lowest energy level, i.e. excitation level= 0.
- Excite all the eigenstates obtained in the previous step up to excitation level lv with $R^\dagger$ and $Q_\pm^\dagger$. Collect these excited non-primary states.
- Compute the eigenstates of the matrix in Eq. (3.5) at the next excitation level= 1. However, this time, only collect those states that give $(a,b,c) = (0,0,0)$ according to Eq. (3.14), i.e. the primary states at this excitation level. Excite only these primary states to excitation level lv with $R^\dagger$ and $Q_\pm^\dagger$. Collect the resulting non-primary states. Repeat this step up to excitation level=$lv-1$.
- At this point, all non-primary states have been computed. Now, compute the eigenstates of the matrix in Eq. (3.5) at the excitation level lv. Collect those states that give $(a,b,c) = (0,0,0)$ according to Eq. (3.14), i.e. the primary states at excitation level= lv.

That this procedure computes the correct eigenstates can be checked by computing the overlap $\langle\Psi'_m|\Psi_k\rangle$ between eigenstates $\{|\Psi_k\rangle\}$ obtained by the procedure above, and eigenstates $\{|\Psi'_m\}$ obtained by only diagonalizing the matrix in Eq. (3.5). The results give δ_{km}, except for the eigenstates that are degenerate in eigenvalues, which have finite overlap between only each other. The eigenvalues of each state $|a,b,c\rangle_P$

are then computed with the expectation values

$$E_N = \langle H \rangle \tag{3.16}$$
$$M = \langle M_z \rangle / \hbar \tag{3.17}$$
$$S = -\frac{1}{2} + \sqrt{\langle S^2 \rangle + \frac{1}{4}} \tag{3.18}$$
$$t = \langle T \rangle, \tag{3.19}$$

where t denote the expectation value of the Casimir operator.

In the case when the Casimir T is not included, different conformal towers are not disentangled. Referring again to the example given earlier, it may happen that $|1,0,0\rangle_P$, $|0,1,1\rangle_P$ and $|0,0,0\rangle_{P'}$ all share eigenvalues for H, M_z, and S^2 (T not included this time). Thus, an eigenvector $|\Psi_1\rangle = \alpha_1|1,0,0\rangle_P + \alpha_2|0,1,1\rangle_P + \alpha_3|0,0,0\rangle_{P'}$, for any coefficients $\alpha_1, \alpha_2, \alpha_3$ is also an eigenvector. Here $|P'\rangle$ has energy $E'_g = E_g + 2\hbar\omega$, but identical $M'_g = M_g$ and $S'_g = S_g$. This would result in $|1,1,1\rangle_{P'}$ according to (3.14), which is wrong. Thus the procedure to compute the eigenstates at excitation level lv must be modified. We first compute the primary states at excitation level lv as follows:

- At excitation levels $= 0, 1, ..., lv - 1$, compute the eigenvectors of the matrix in Eq. (3.5).
- Excite all the states obtained in the previous step to excitation level lv with $R^\dagger$ and $Q^\dagger_\pm$. Create a matrix with the excited non-primary states $\{|NP_i\rangle\}$

$$Y = \begin{bmatrix} | & | & \\ NP_1 & NP_2 & \dots \\ | & | & \end{bmatrix}. \tag{3.20}$$

- Compute the eigenstates of the matrix in Eq. (3.5) at excitation level $= lv$. Only collect those states that give $(a, b, c) = (0, 0, 0)$ according to Eq. (3.14), i.e. the primary states at this excitation level.
- If not all primary states have been obtained (one can count how many should exist at a given excitation level recursively), add the primary states $\{|P_i\rangle\}$ from the previous step to the matrix of excited non-primary states

$$Y = \begin{bmatrix} | & | & & | & | & \\ NP_1 & NP_2 & \dots & P_1 & P_2 & \dots \\ | & | & & | & | & \end{bmatrix}. \tag{3.21}$$

- Collect all the remaining states at excitation level lv that share eigenvalues. For the number of states $\{|\Psi_i\rangle\}$, $i = 1, 2, \dots, l$, that share an eigenvalue, compute a superposition

$$|\psi\rangle = \sum_{i=1}^{l} \alpha_i |\Psi_i\rangle \tag{3.22}$$

for unknown coefficients α_i. Determine the coefficients by computing the kernel of the matrix Y in Eq. (3.21)

$$Y|\psi\rangle = 0. \tag{3.23}$$

Such a state $|\psi\rangle$ is in the kernel of all non-primary states and the primary state already found, i.e. another primary state. Collect this state and add it as another column in Y in Eq. (3.21).

- Repeat the above step until all primary states at lv have been found.

From the above procedure, the eigenstates at energy level lv are found by first finding the primary states at levels $0, 1, \ldots, lv$. Then all non-primary states are obtained by exciting the primary states to excitation lv with the use of $R^\dagger, Q_\pm^\dagger$. Again, that this procedure computes the correct eigenstates can be checked by computing the overlap $\langle \Psi'_m | \Psi_k \rangle$ between eigenstates $\{|\Psi_k\rangle\}$ obtained by the procedure above, and eigenstates $\{|\Psi'_m\}$ obtained by only diagonalizing the matrix in Eq. (3.5). The results give δ_{km}, except for the eigenstates that are degenerate in eigenvalues, which have finite overlap between only each other. The eigenvalues of each state $|a, b, c\rangle_P$ are then computed as

$$E_N = \langle H \rangle \tag{3.24}$$

$$M = \langle M_z \rangle / \hbar \tag{3.25}$$

$$S = -\frac{1}{2} + \sqrt{\langle S^2 \rangle + \frac{1}{4}} \tag{3.26}$$

$$t = \left(\frac{E_g^{(0)} + \hbar\Omega M_g}{\hbar\omega} - 1 \right) \left(\frac{E_g^{(0)} + \hbar\Omega M_g}{\hbar\omega} - 3 \right), \tag{3.27}$$

where t denotes the expectation value of the Casimir operator and $E_g^{(0)}$, M_g denote the non-interacting energy and the total angular momentum of the primary state $|P\rangle$ of the conformal tower.

3.3 Monte Carlo Simulations

At this point, we know how to obtain all primary states and the non-primary states. We are thus in a position to sample the many-body wave function in order to confirm the hyperradial distribution in Eq. (2.140) that nonrelativistic conformal symmetry predicts. The method used is Metropolis importance sampling. It can be adapted to provide the center-of-mass distribution as well and is described below.

For a given state $|a, b, c\rangle_P$ obtained from the diagonalization described in the previous section with particle number N, we determine the center-of-mass distribution $\Psi_{\text{c.m.}}(C)$ in Eq. (2.110) and the hyperradial distribution $F(\tilde{R})$ in Eq. (2.140) by sampling the perturbative many-body wave function $|\Psi_{a,b,c}(\mathbf{r}_{1\uparrow}, \cdots, \mathbf{r}_{1\downarrow}, \cdots)|^2$ and creating histograms of the coordinates C and $\tilde{R}$. The many-body wavefunction $|\Psi_{a,b,c}(\mathbf{r}_{1\uparrow}, \cdots, \mathbf{r}_{1\downarrow}, \cdots)|^2$ is generally a superposition of Slater determinants in Eq. (2.20), with coefficients determined from the diagonalization described in the previous section. The Metropolis algorithm used proceeds as follows

1) Choose N random initial position $\mathbf{r}_{1\uparrow}, \ldots, \mathbf{r}_{1\uparrow}, \ldots$ within a radius of $1.5\ell_{ho}$ from the trap center. Denote the current particle configuration $\mathbf{X} = (\mathbf{r}_{1\uparrow}, \ldots, \mathbf{r}_{1\uparrow}, \ldots)$. Calculate the number $|\Psi_{a,b,c}(\mathbf{X})|^2$.

2) Choose a particle with position $\mathbf{r}_{i\sigma}$ randomly and propose a new particle configuration $\mathbf{r}'_{i\sigma} = \mathbf{r}_{i\sigma} + \mathbf{r}$. Here $\mathbf{r}$ denotes a move in a random direction $\theta \in [0, 2\pi]$ by a random distance $r \in [0, \delta]$, where δ is the variance of the step size in each Metropolis iteration it. Denote the new particle configuration with the i^{th} particle position changed $\mathbf{X}' = (\dots, \mathbf{r}'_{i\sigma} = \mathbf{r}_{i\sigma} + \mathbf{r}, \dots)$ Calculate the new value of $|\Psi_{a,b,c}(\mathbf{X}')|^2$.
3) Compute the ratio

$$\xi = \frac{|\Psi_{a,b,c}(\mathbf{X}')|^2}{|\Psi_{a,b,c}(\mathbf{X})|^2}. \tag{3.28}$$

4) Choose a random number $\xi' \in [0, 1]$ and determine whether to accept or reject the new particle configuration $\mathbf{X}'$

$$\begin{cases} \text{Accept} & \text{if } \xi > \xi' \\ \text{Reject} & \text{otherwise.} \end{cases} \tag{3.29}$$

5) If the new particle configuration is accepted, update the current configuration $\mathbf{X} = \mathbf{X}'$. If rejected, keep the current particle configuration $\mathbf{X} = \mathbf{X}$.
6) Step 2)→5) is one Metropolis iteration, referred to as one it. If it is larger than the number of warm-up iterations, referred to as eq, do 7), or else repeat steps 2)→6).
7) Here histograms of $\Psi_{\text{c.m.}}(C)$ in Eq. (2.110), and the hyperradial distribution $F(\tilde{R})$ in Eq. (2.140) are computed. From the current particle configuration $\mathbf{X} = (\mathbf{r}_{i\uparrow}, \dots, \mathbf{r}_{i\downarrow}, \dots)$, compute the center-of-mass coordinate

$$C = \sqrt{\mathbf{C} \cdot \mathbf{C}} = \sqrt{\left(\sum_{\sigma=\uparrow,\downarrow} \sum_{i=1}^{N_\sigma} \mathbf{r}_{i\sigma} \right)^2} \tag{3.30}$$

and the hyperradius

$$\tilde{R} = \sqrt{\sum_{\sigma=\uparrow,\downarrow} \sum_{i=1}^{N_\sigma} (\mathbf{r}_{i\sigma} - \mathbf{C})^2}. \tag{3.31}$$

Store the C and $\tilde{R}$ coordinates in the corresponding bin of binsize ΔC and $\Delta\tilde{R}$ respectively. Repeat steps 2)→7).

The values used in the above described algorithm was: $\delta = 0.7\ell_{ho}$ for the variance of the step size, $eq = 10^4$ for the warm-up steps, and $\Delta C = \Delta\tilde{R} = 0.05\ell_{ho}$ for the bin sizes. Then, when the algorithm was ran for $N = 2$, the Metropolis iterations $it = 10^6 + 10^4$ was used, whereas for $N = 6$, $it = 4 \cdot 10^5 + 10^4$.

4

Results

The results section begins by first illustrating the density such that the internal breathing mode and the center-of-mass excitations can be seen, as discussed in Sec. 2.6. Second, the results of the energy spectrum and the conformal towers will be shown for various particle numbers N and rotation frequencies Ω. Then, the hyperradial distribution in Eq. (2.140) predicted by the nonrelativistic conformal symmetry together with the corresponding center-of-mass distribution in (2.110) will be shown together with Monte Carlo simulations, as discussed in Sec. 3.3. Last, the results of induced transitions by different ways of perturbing the system experimentally (see Sec. 2.7) are shown. Throughout the results section, the dimensionless attractive interaction strength $g\ell_{ho}^2/\hbar\omega = -1$ is used.

4.1 Density Calculations

In this section, we illustrate the internal breathing mode and center-of-mass excitations. For illustrative purposes, $N = 2$ particles and rotation frequency $\Omega = 0$ have been chosen. In Fig. 4.1 we show an equal superposition of the ground state and the first excited state with $R^\dagger$, according to Eq. (2.145). Note that the density oscillates, looking as if the gas breathes, with exactly twice the trapping frequency 2ω. In Fig. 4.2 we show an equal superposition of the ground state and the first excited state with $Q_+^\dagger$ (top), or $Q_-^\dagger$ (bottom), according to Eq. (2.146). Note that the center-of-mass excitations correspond to stirring the gas in the direction of rotation ($Q_+^\dagger$) with frequency exactly $(\omega - \Omega)$, and in the opposite direction of rotation ($Q_-^\dagger$) with frequency exactly $(\omega + \Omega)$.

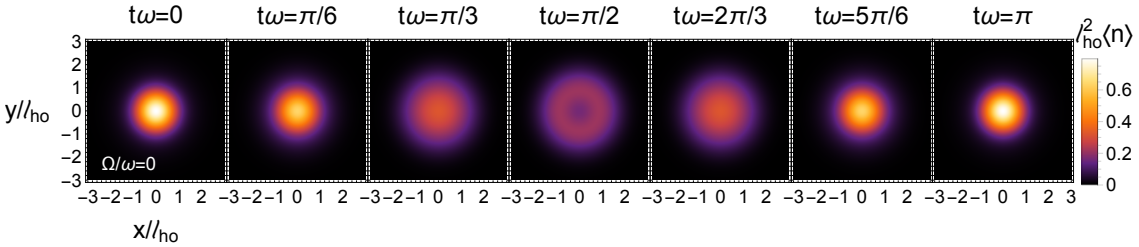

Figure 4.1: Density $\langle n \rangle$ for $N = 2$ and frequency $\Omega = 0$ of the state $e^{-iHt/\hbar}(|gs\rangle + R^\dagger|gs\rangle)$ according to Eq. (2.145). Notice that the frequency of the internal breathing mode is exactly twice the trapping frequency 2ω.

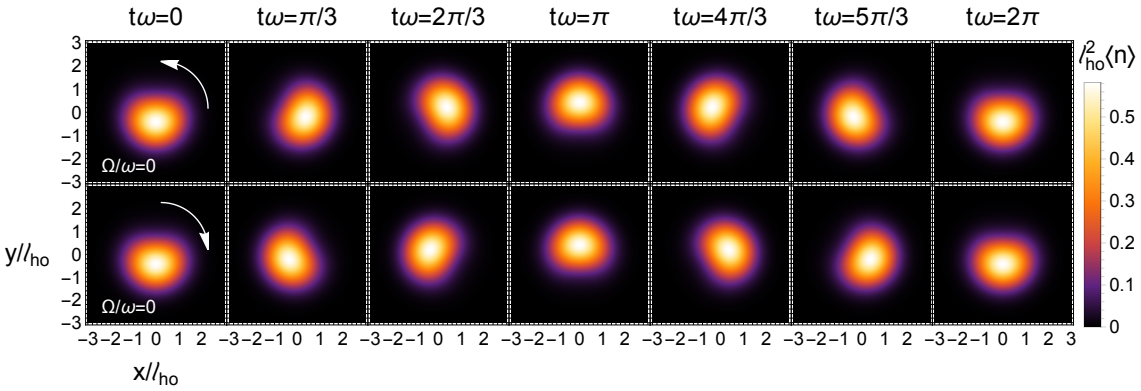

Figure 4.2: Density $\langle n \rangle$ for $N = 2$ and $\Omega = 0$ of the state $e^{-iHt/\hbar}(|gs\rangle + Q_{\pm}^{\dagger}|gs\rangle)$. The top row is the superposition with $Q_{+}^{\dagger}$, corresponding to stirring the gas in the direction of rotation (see white arrow). The bottom row is the superposition with $Q_{-}^{\dagger}$, corresponding to stirring the gas in the opposite direction of rotation (see white arrow). For no rotation frequency $\Omega = 0$, the gas rotates at a frequency of exactly ω in both cases, but in different directions.

4.2 Conformal Towers

Here, the results of the energy spectrum which is built by conformal towers (see Sec. (2.4)) are shown. Although the conformal tower structure is predicted by the nonrelativistic conformal symmetry, the position of the primary states is not, and obtained by the diagonalization routine described in Sec. 3.1 and 3.2. We show the results for $N = 2$ particles in Fig. 4.3 because the conformal tower structure is most easily seen there. Furthermore, the energy spectrum for $N = 6$ and $N = 12$ particles is also shown in Fig. 4.4 and 4.5.

In Fig. 4.3, the results of the energy spectrum for $N = 2$ at different rotation frequencies Ω are shown. The states are colored according to their Casimir $\langle T \rangle$ (see Sec. 2.4.5). The conformal tower structure can clearly be seen (c.f. Fig. 2.5), but note that the Casimir only relates to the ground step energy without rotation $E_{g,\Omega=0}^{(0)} = E_{g}^{(0)} + \hbar\Omega M_g$. Hence, multiple conformal towers have the same color coding. Note that the effect of increasing the rotation frequency Ω is to shift states with angular momentum $M > 0$ ($M < 0$) to lower (higher) energies.

For Fig. 4.4 and 4.5 however, only primary and nonprimary states are distinguished for clarity. Note that the effect of increasing the rotation frequency Ω is more pronounced here. It can be seen that the ground state (which always is a primary state) as a function of rotation frequency will change. As can be seen in Fig. 4.4, the ground state has no angular momentum $M = 0$ for no rotation, and at $\Omega = \omega/2$ the ground state has angular momentum $M = 6$. Similarly in Fig. 4.5, the ground state has no angular momentum $M = 0$ for no rotation, and at $\Omega = 2\omega/5$ the ground state has angular momentum $M = 10$, and at $\Omega = 2\omega/5$, $M = 18$. The conformal tower structure as in Fig. 2.5 is indeed present.

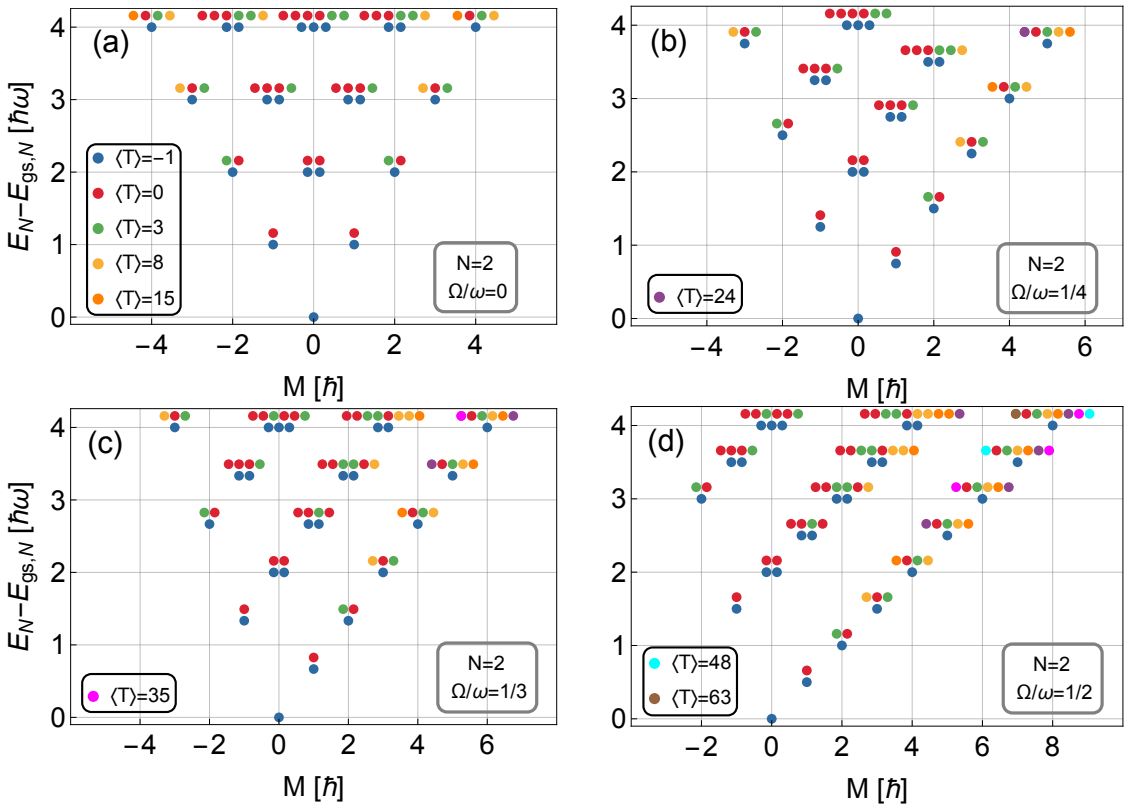

Figure 4.3: Excitation spectrum for $N = 2$ particles ordered by angular momentum at rotation frequencies $\Omega = 0$, $\Omega = \omega/4$, $\Omega = \omega/3$, and $\Omega = \omega/2$ respectively. The color coding is consistent in all figures and overlapping points are moved horizontally for clarity. One can count the number of states according to Fig. 2.5 and see that the conformal tower structure indeed is present. Note that the Casimir $\langle T \rangle$ to leading order in perturbation theory (see Eq. (2.91)) only depends on the ground step energy without rotation $E^{(0)}_{g,\Omega=0} = E^{(0)}_g + \hbar\Omega M_g$, meaning that multiple conformal towers share the same $\langle T \rangle$. Furthermore, note that the effect of rotation $\Omega > 0$ is to lower (raise) states with $M > 0$ ($M < 0$) in energy.

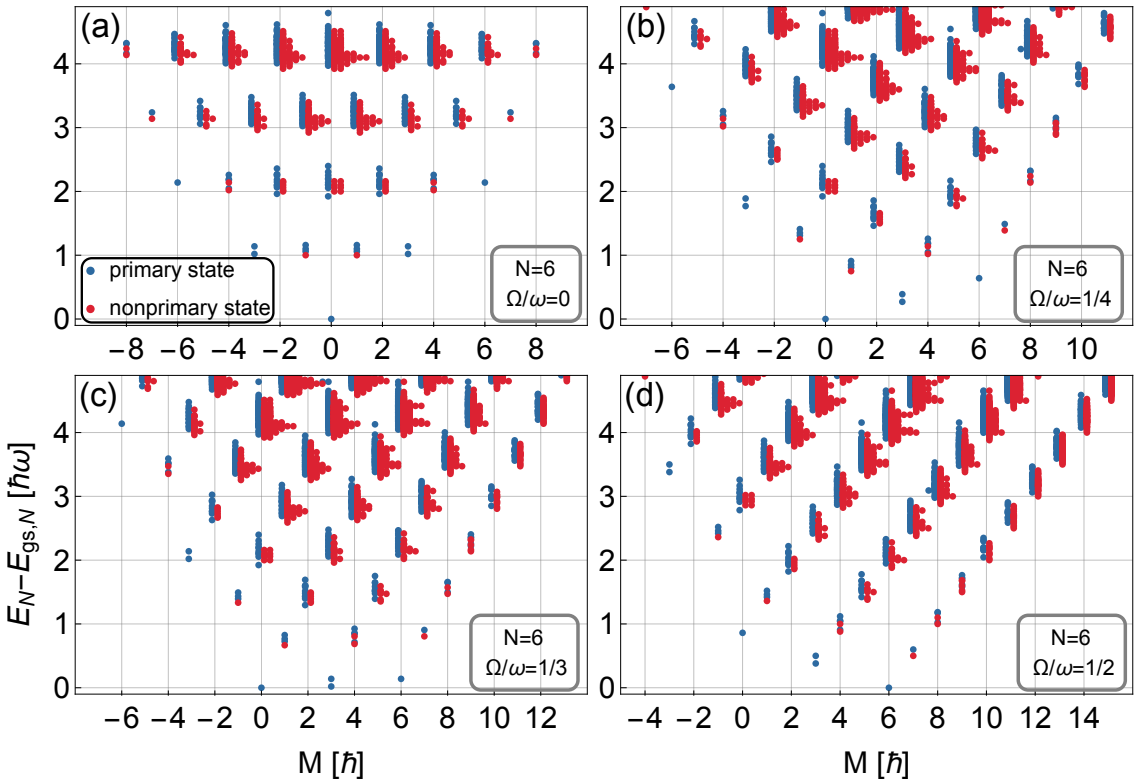

Figure 4.4: Excitation spectrum for $N = 6$ particles ordered by angular momentum at rotation frequencies $\Omega = 0$, $\Omega = \omega/4$, $\Omega = \omega/3$, and $\Omega = \omega/2$ respectively. Blue points represent primary states and red points nonprimary states. The color coding is consistent in all figures and overlapping points are moved horizontally for clarity. Furthermore, note that upon rotation the angular momentum of the ground state change from $M = 0$ in (a) (b),(c) to $M = 6$ in (d).

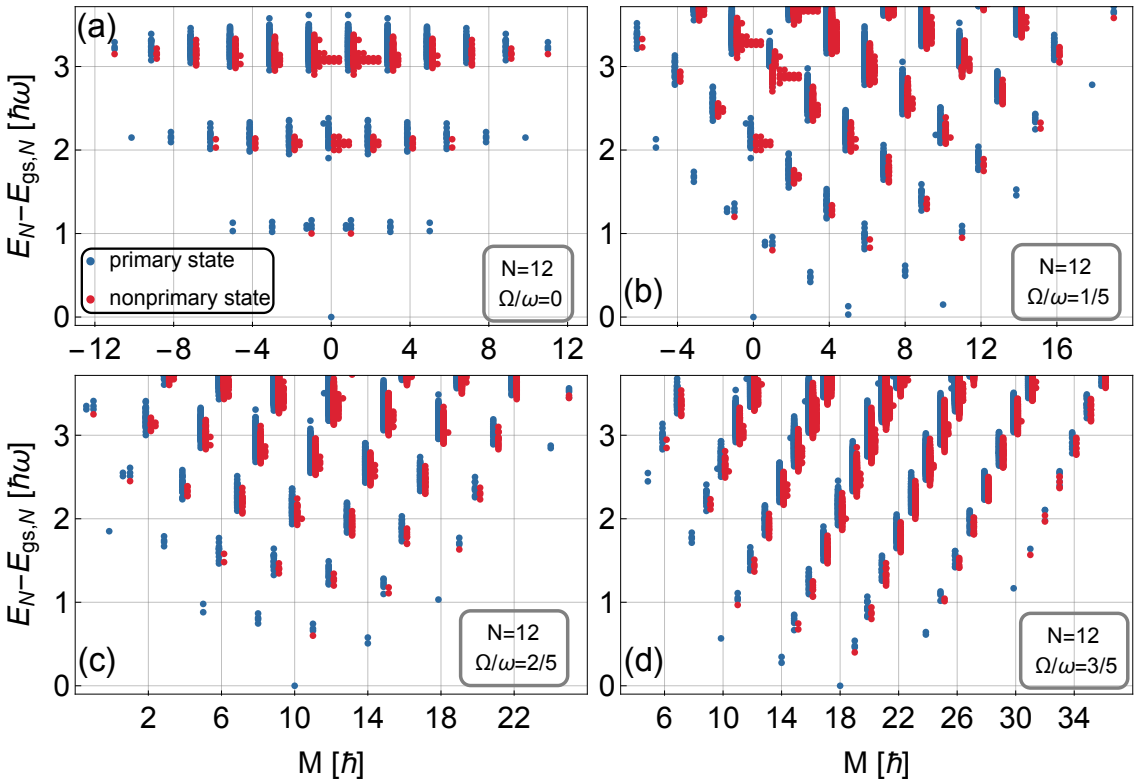

Figure 4.5: Excitation spectrum for $N = 12$ particles ordered by angular momentum at rotation frequencies $\Omega = 0$, $\Omega = \omega/5$, $\Omega = 2\omega/5$, and $\Omega = 3\omega/5$ respectively. Blue points represent primary states and red points nonprimary states. The color coding is consistent in all figures and overlapping points are moved horizontally for clarity. Furthermore, note that upon rotation the angular momentum of the ground state change from $M = 0$ in (a) and (b) to $M = 10$ in (c), and $M = 18$ in (d).

4.3 Hyperradial and Center-Of-Mass Distribution

In this section, the results of the Monte Carlo simulations discussed in Sec. 3.3 of the hyperradial distribution $F(\tilde{R})$ in Eq. (2.140) and the center-of-mass distribution $\Psi_{\text{c.m.}}(C)$ in Eq. (2.110) are shown. First, the results for $N = 2$ are shown where excitation levels up to $E_{gs}^{(0)} + 4\hbar\omega$ are included, whereas for $N = 6$ excitation levels only up to $E_{gs}^{(0)} + 2\hbar\omega$ are shown. This is for clarity such that one can compare the energy spectrum to the distributions in a color coding that match the two. Note that from Fig. 4.6 and 4.9, it can be seen that states with an equal number of internal breathing mode excitations a, derived from primary states at the same excitation level without rotation $E_{g,\Omega=0}^{(0)} = E_g^{(0)} + \hbar\Omega M_g$ (i.e. same s, or $\langle T \rangle$, in Eq. (2.140)) share the same hyperradial distribution $F(\tilde{R})$.

4.3.1 $N = 2$

Here, the results of sampling the hyperradial distribution $F(\tilde{R})$ in Eq. (2.140) with Monte Carlo simulations for $N = 2$ particles and no rotation $\Omega = 0$ are shown in Fig. 4.6. Note that the hyperradial distribution $F(\tilde{R})$ of the lowest 70 energy eigenstates collapse onto just 9 different curves, and the Monte Carlo simulations perfectly intersect the analytical predictions that the nonrelativistic conformal symmetry implies in Eq. (2.140). States with an equal number of internal breathing mode excitations a derived from primary states at the same excitation level without rotation $E_{gs,\Omega=0}^{(0)} = E_{gs}^{(0)} + \Omega M_{gs}$ (i.e. same s, or $\langle T \rangle$, in Eq. (2.140)) share the same hyperradial distribution $F(\tilde{R})$.

In Fig. 4.7, the results of sampling the center-of-mass distribution $\Psi_{\text{c.m.}}(C)$ in Eq. (2.110) with Monte Carlo simulations for $N = 2$ and no rotation $\Omega = 0$ are shown. Again, note that the center-of-mass distribution $\Psi_{\text{c.m.}}(C)$ of the lowest 70 energy eigenstates collapse onto just 9 different curves and the Monte Carlo simulations perfectly intersect the analytical prediction in Eq. (2.110). Note that all states with $b = c = 0$, i.e. all primary states and pure internal breathing mode excitations share the same center-of-mass distribution. Furthermore, states where $\{\max(b, c), |b - c|\}$ are the same also share the same distribution.

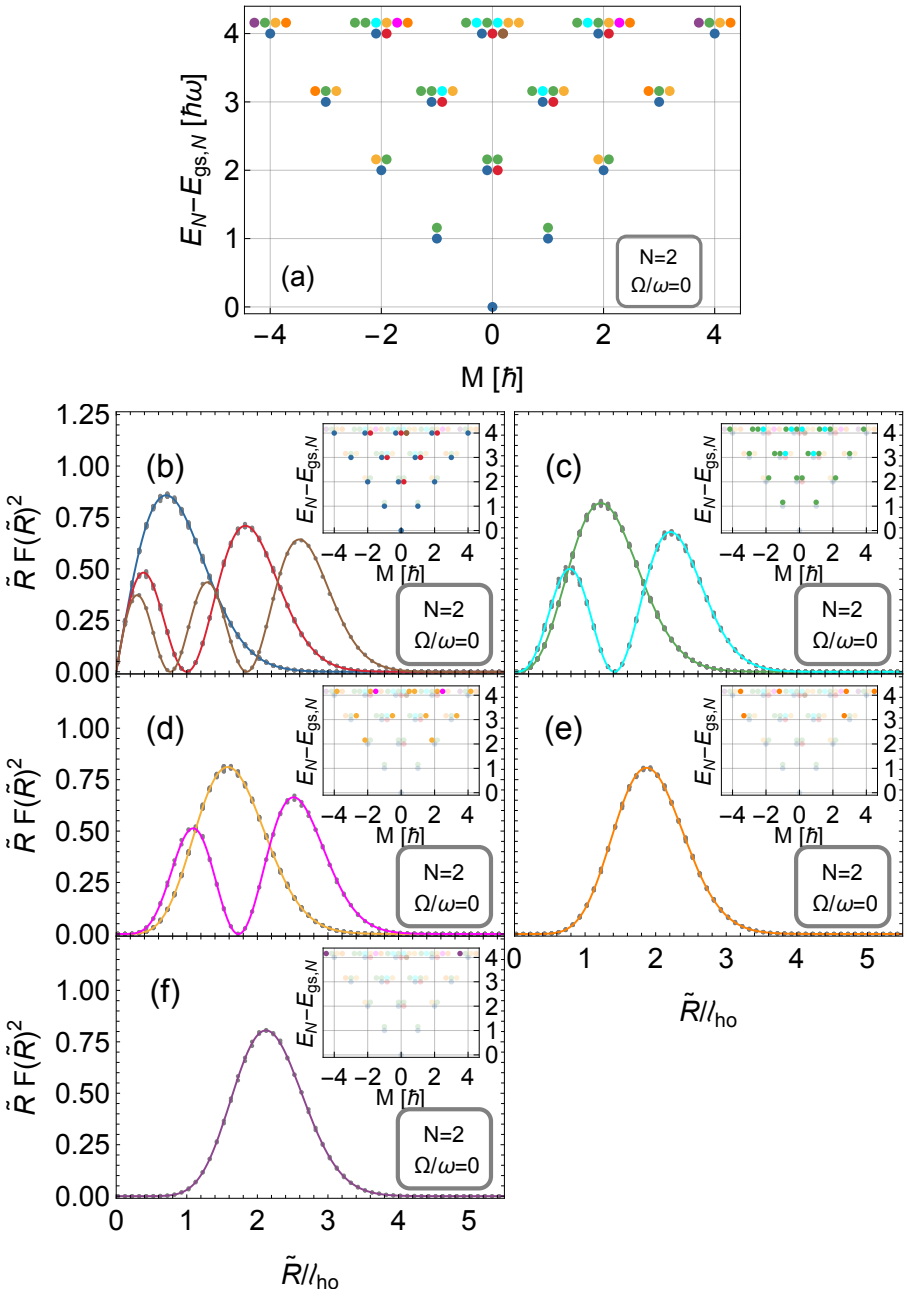

Figure 4.6: (a) Energy spectrum of the lowest 70 energy eigenstates for $N = 2$ and $\Omega/\omega = 0$ with a color coding that matches the hyperradial distribution. (b)-(f) Show gray points that are the results of Monte Carlo sampling and colored continuous lines are analytical predictions of the hyperradial distribution in Eq. (2.140). The insets show the same energy spectrum as in (a), but where the states matching the hyperradial distribution are highlighted. Multiple distributions in the same figure are shown when they share Casmir $\langle T \rangle$, but correspond to different numbers of internal breathing mode excitations a.

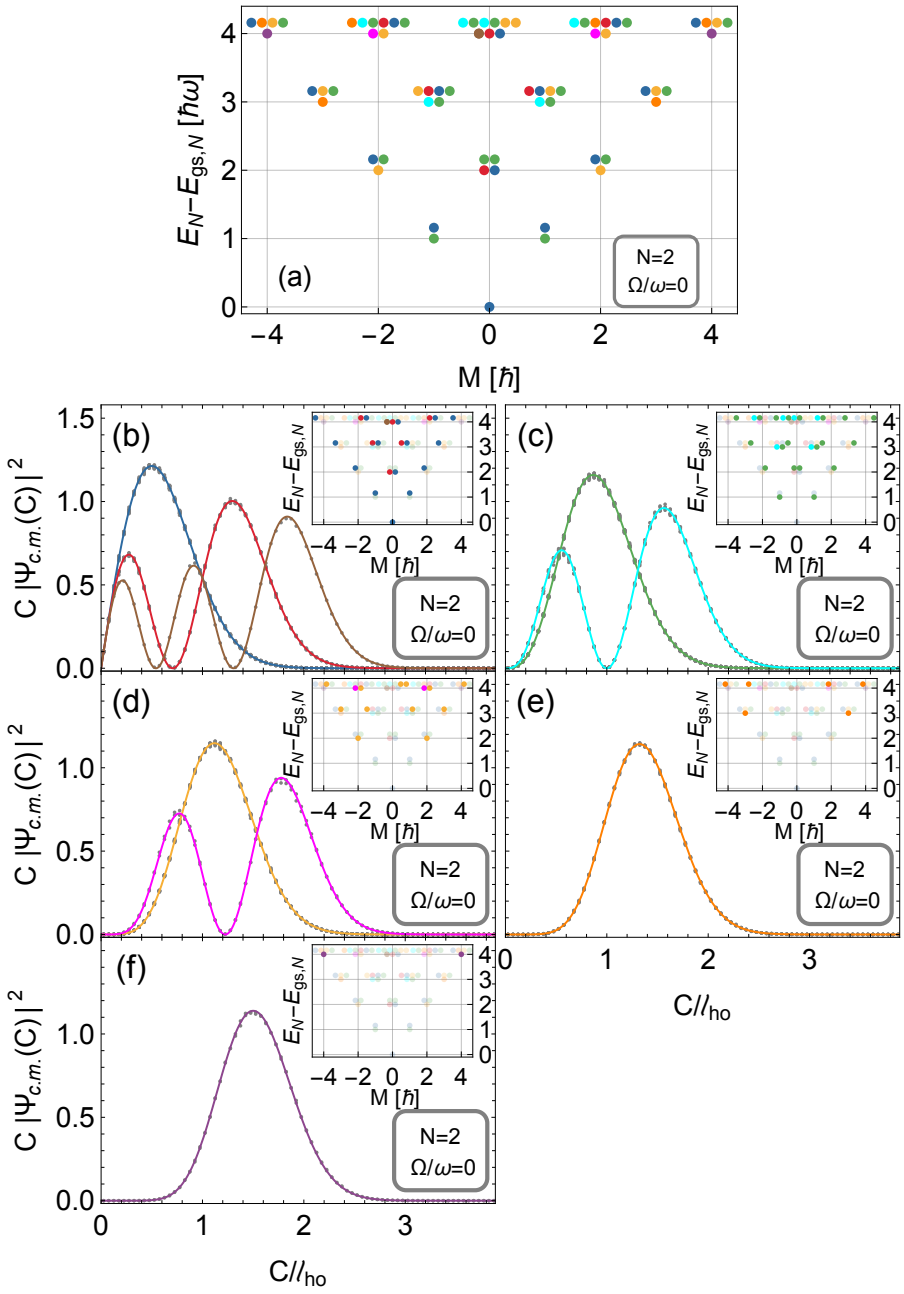

Figure 4.7: (a) Energy spectrum of the lowest 70 energy eigenstates for $N = 2$ and $\Omega/\omega = 0$ with a color coding that matches the center-of-mass distribution in Eq. (2.110). (b)-(h) Show gray points that are the results of Monte Carlo sampling and colored continuous lines are analytical predictions of the center-of-mass distribution in Eq. (2.110). The insets show the same energy spectrum as in (a), but where the states matching the center-of-mass distribution are highlighted. Multiple distributions are shown in the same figure when $|b - c|$ = constant. Note that all primary states and pure internal breathing mode excitations share the same center-of-mass distribution in blue.

4.3.2 $N = 6$

In Fig. 4.8, the results of sampling the center-of-mass distribution $\Psi_{\text{c.m.}}(C)$ in Eq. (2.110) with Monte Carlo simulations for $N = 6$ and no rotation $\Omega/\omega = 1/2$ are shown. Note that the center-of-mass distribution $\Psi_{\text{c.m.}}(C)$ of the lowest 115 energy eigenstates collapse onto just 6 different curves and the Monte Carlo simulations show excellent agreement with the analytical prediction in Eq. (2.110). The accuracy is not as high in comparison to Fig. 4.7 because fewer Monto Carlo steps were run (see section 3.3) due to more states and larger superpositions. Note that all states with $b = c = 0$, i.e. all primary states and pure internal breathing mode excitations share the same center-of-mass distribution. Furthermore, states where $\{\max(b, c), |b - c|\}$ are the same also share the same distribution.

The results of sampling the hyperradial distribution $F(\tilde{R})$ in Eq. (2.140) with Monte Carlo simulations for $N = 6$ particles and rotation $\Omega/\omega = 1/2$ are shown in Fig. 4.9. Again, note that the hyperradial distribution $F(\tilde{R})$ of the lowest 115 energy eigenstates collapse onto just 8 different curves, and the Monte Carlo simulations show excellent agreement with the analytical predictions of the nonrelativistic conformal symmetry, Eq. (2.140). States with an equal number of internal breathing mode excitations a derived from primary states at the same excitation level without rotation $E^{(0)}_{gs,\Omega=0} = E^{(0)}_{gs} + \Omega M_{gs}$ (i.e. same s, or $\langle T \rangle$, in Eq. (2.140)) share the same hyperradial distribution $F(\tilde{R})$.

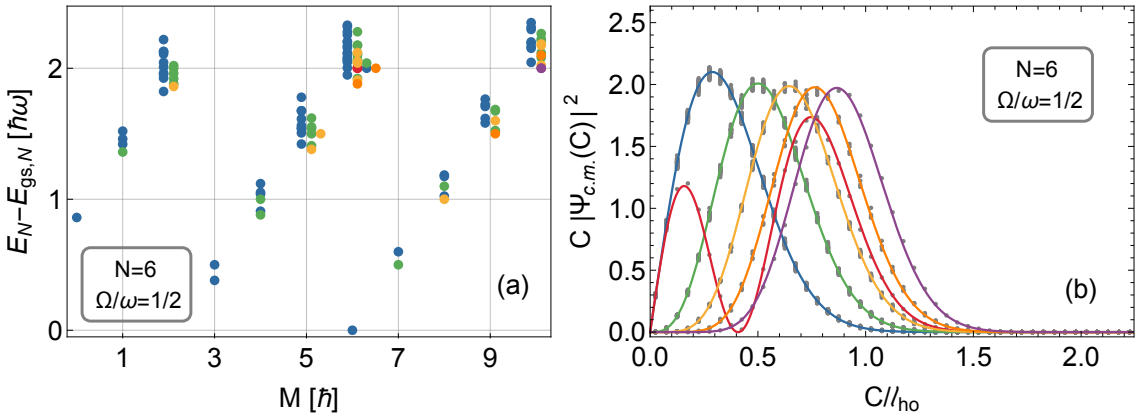

Figure 4.8: (a) Energy spectrum of the lowest 115 energy eigenstates for $N = 6$ and $\Omega/\omega = 1/2$ with a color coding that matches the center-of-mass distribution in Eq. (2.110). (b) The center-of-mass distribution, where gray points are the results of Monte Carlo sampling and colored continuous lines are analytical predictions. Note that all primary states and pure internal breathing mode excitations share the same center-of-mass distribution in blue.

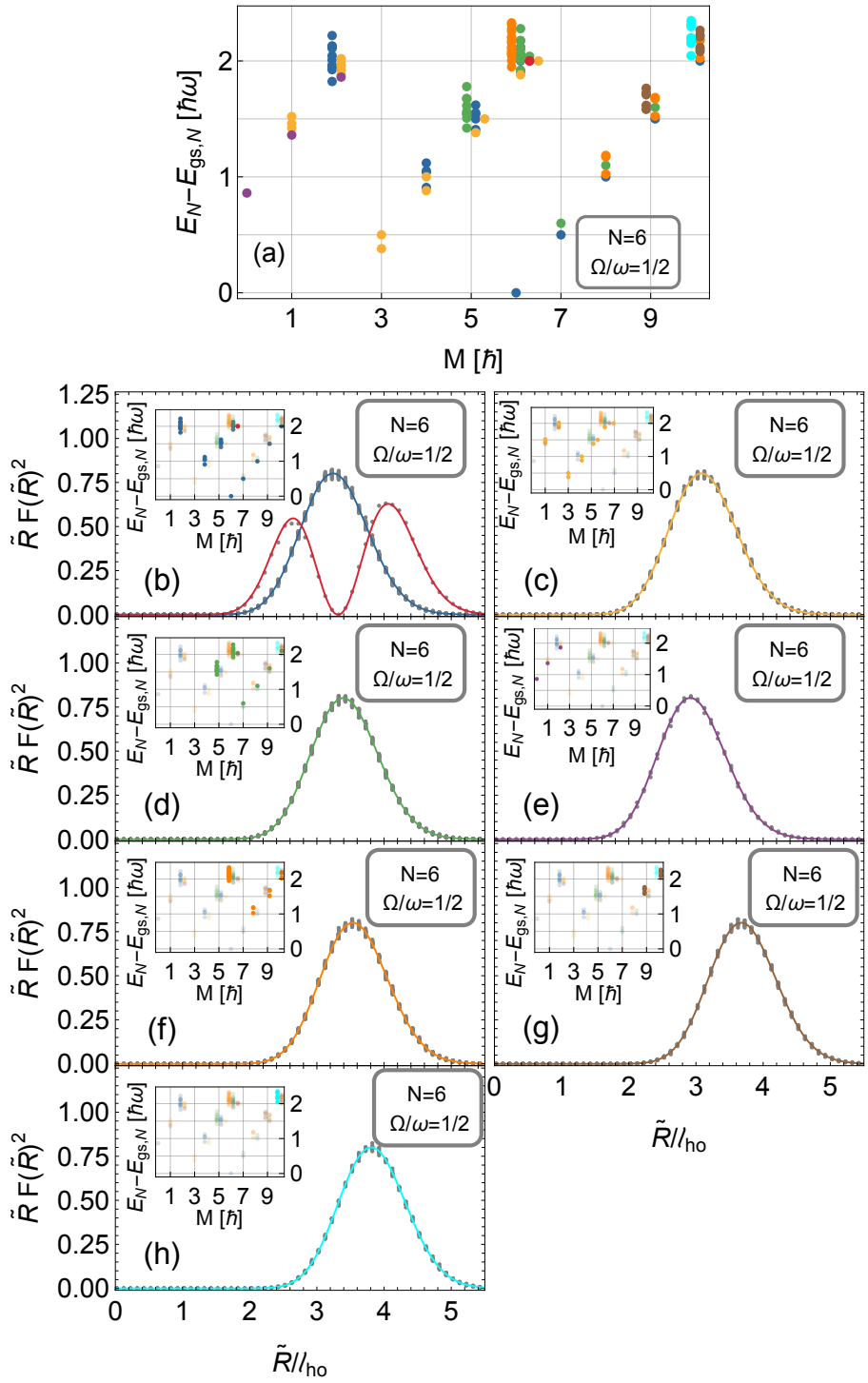

Figure 4.9: (a) Energy spectrum of the lowest 115 energy eigenstates for $N = 6$ and $\Omega/\omega = 1/2$ with a color coding that matches the hyperradial distribution in Eq. (2.140). (b)-(h) Hyperradial distribution, where gray points are the results of Monte Carlo sampling and colored continuous lines are analytical predictions. The insets show the same energy spectrum as in (a), but where the states matching the hyperradial distribution are highlighted. In (b), two distributions are shown because they belong to the same conformal tower, and they share Casimir $\langle T \rangle$, but correspond to different internal breathing mode excitations $a = 0$ (blue) or $a = 1$ (red).

4.4 Induced Transitions for $N = 2$

Here, the results of inducing transitions between states when perturbing the system in a way that should be experimentally accessible, as discussed in Sec. 2.7, are shown. For illustrative purposes, $N = 2$ particles is chosen. In Fig. 4.10, some ground state properties of $N = 2$ particles for two different rotation frequencies $\Omega = 0, 1/2$ are shown.

Then, in Sec. 4.4.1, the results of an anisotropic frequency perturbation are shown. In Sec. 4.4.2 we show the results of a trap center perturbation. In Sec. 4.4.3, the results of an isotropic trap frequency perturbation are shown. Last, the results of an interaction strength perturbation are shown in Sec. 4.4.4.

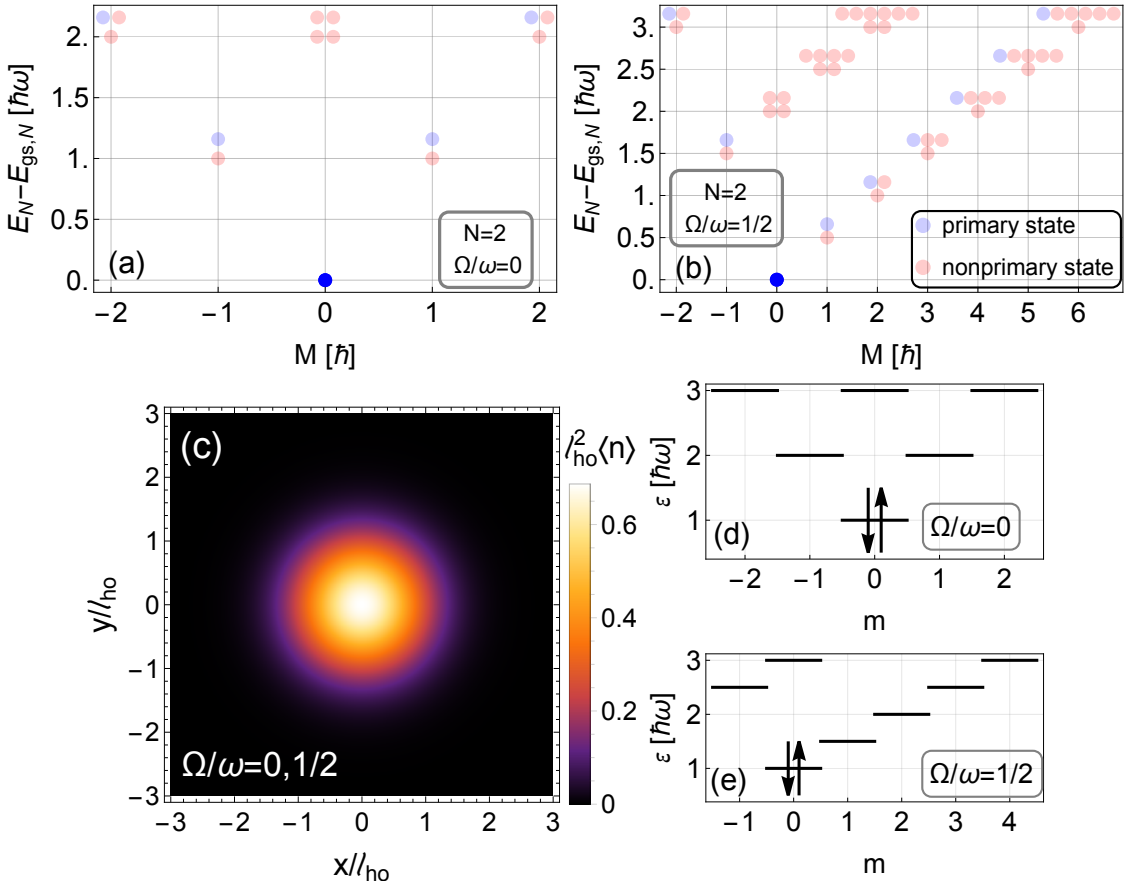

Figure 4.10: Excitation spectrum for $N = 2$ particles in (a) and (b) for $\Omega/\omega = 0$ and $\Omega/\omega = 1/2$ respectively. The ground state is highlighted to indicate that this is the state (c), (d), and (e) refer to. (c) Shows the ground state density which is the same for both rotation frequencies. (d), (e) Show the corresponding ground state occupancy of single-particle energy levels.

4.4.1 Anisotropic Frequency Perturbation

In this section, the results of perturbing the frequency anisotropically $\delta\omega_x$, as discussed in Sec. 2.7.1 are shown. In Fig. 4.11, the excitation spectrum with only

states that are connected to the ground state (see Fig. 4.10) is shown. The corresponding time evolution of the density of the resulting state is also shown. Note that the perturbation connects the ground state predominantly to itself, but also to center-of-mass excitations, internal breathing mode excitations, and different primary states.

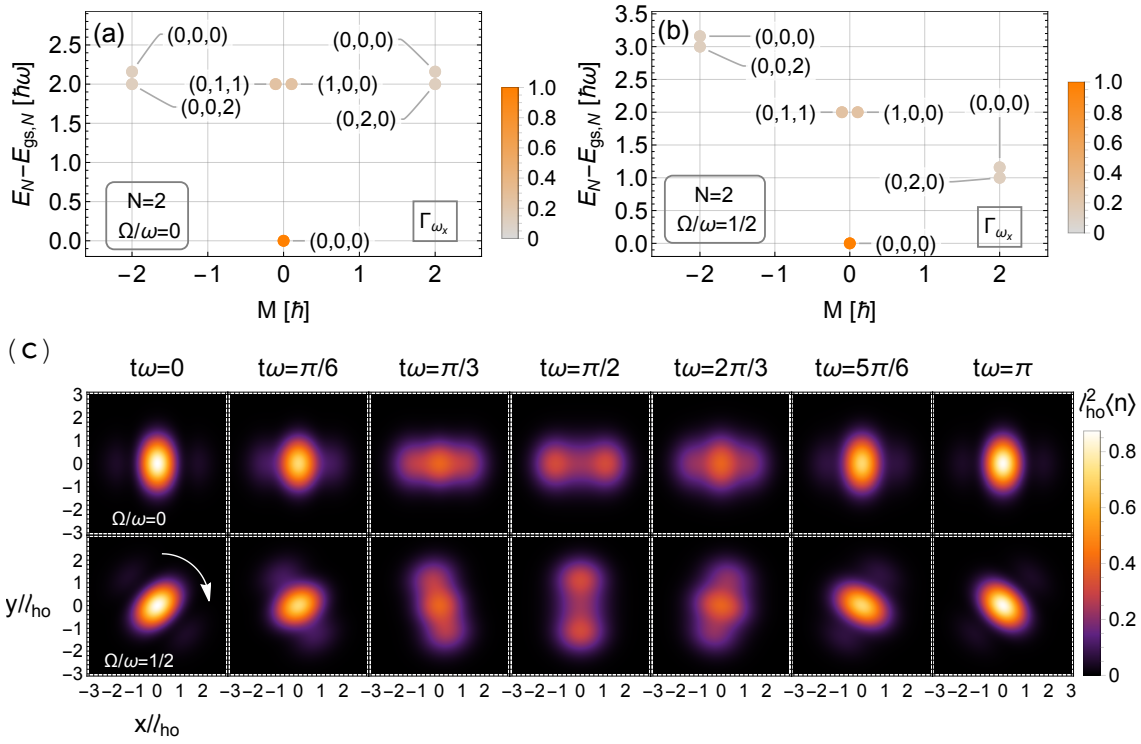

Figure 4.11: Excitation spectrum upon an anisotropic frequency perturbation $\delta\omega_x$ for $N = 2$ particles in (a) and (b) for $\Omega/\omega = 0$ and $\Omega/\omega = 1/2$ respectively. The color coding refers to the relative strength of the transition matrix elements of Γ_{ω_x} in Eq. (2.147) starting in the ground state. Only states with non-zero overlap are shown and overlapping points are moved horizontally. The numbers are (a, b, c), referring to the number of times a state has been acted on by $R^\dagger$ and $Q_\pm^\dagger$ according to Eq. (2.82). Note that these are all states the transition matrix Γ_{ω_x} can connect the ground state to (in Fig. 4.10). Furthermore, it connects to center-of-mass excitations, internal breathing mode excitations, and to other primary states. (c) Shows the corresponding time evolution of the density of the resulting state $|\Psi\rangle = \Gamma_{\omega_x}|gs\rangle$ for the two rotation frequencies $\Omega/\omega = 0$ (top) and $\Omega/\omega = 1/2$ (bottom). Note that for $\Omega/\omega = 1/2$, the density is rotating, which is indicated by the white arrow.

4.4.2 Trap Center Perturbation

This section shows the results of perturbing the trap center anisotropically δx_0, as discussed in Sec. 2.7.2. In Fig. 4.12, the excitation spectrum with only states that are connected to the ground state (see Fig. 4.10) is shown. The corresponding time evolution of the density of the resulting state is also shown. Note that the perturbation does not connect the ground state to itself, but only to center-of-mass

excitations within the same conformal tower (see Fig. (2.5)).

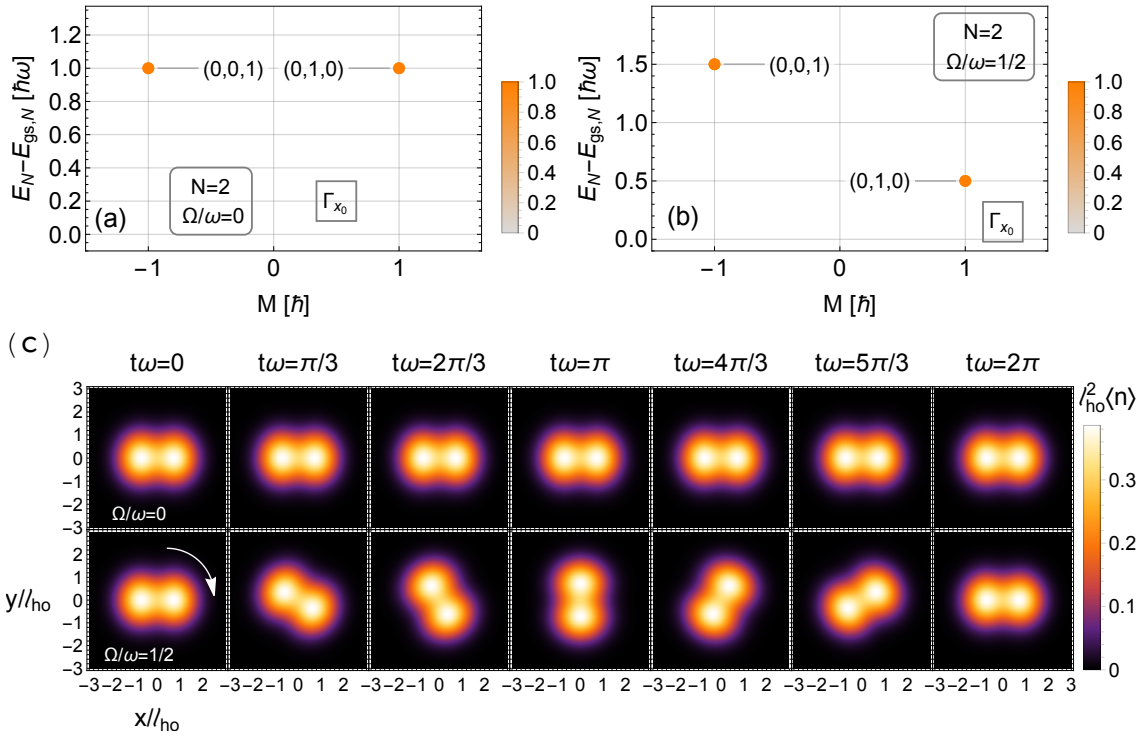

Figure 4.12: Excitation spectrum upon an anisotropic trap center perturbation δx_0 for $N = 2$ particles in (a) and (b) for $\Omega/\omega = 0$ and $\Omega/\omega = 1/2$ respectively. The color coding refers to the relative strength of the transition matrix elements of Γ_{x_0} in Eq. (2.147) starting in the ground state. Only states with non-zero overlap are shown. The numbers are (a, b, c), referring to the number of times a state has been acted on by $R^\dagger$ and $Q_\pm^\dagger$ according to Eq. (2.82). Note that these are all states the transition matrix Γ_{x_0} can connect the ground state to (in Fig. 4.10). Furthermore, it connects only to center-of-mass excitations within the same conformal tower. (c) Shows the corresponding time evolution of the density of the resulting state $|\Psi\rangle = \Gamma_{x_0}|gs\rangle$ for the two rotation frequencies $\Omega/\omega = 0$ (top) and $\Omega/\omega = 1/2$ (bottom). Note that for no rotation, the density is stationary, whereas, for $\Omega/\omega = 1/2$, the density is rotating indicated by the white arrow.

4.4.3 Isotropic Trap Frequency Perturbation

Here, we show the results of perturbing the frequency isotropically $\delta\omega$, as discussed in Sec. 2.7.3. In Fig. 4.13, the excitation spectrum with only states that are connected to the ground state (see Fig. 4.10) is shown. The corresponding time evolution of the density of the resulting state is also shown. Note that the perturbation connects the ground state predominantly to itself, but also to center-of-mass excitations and internal breathing mode excitations. However, all states connected belong to the same conformal tower (see Fig. 2.5).

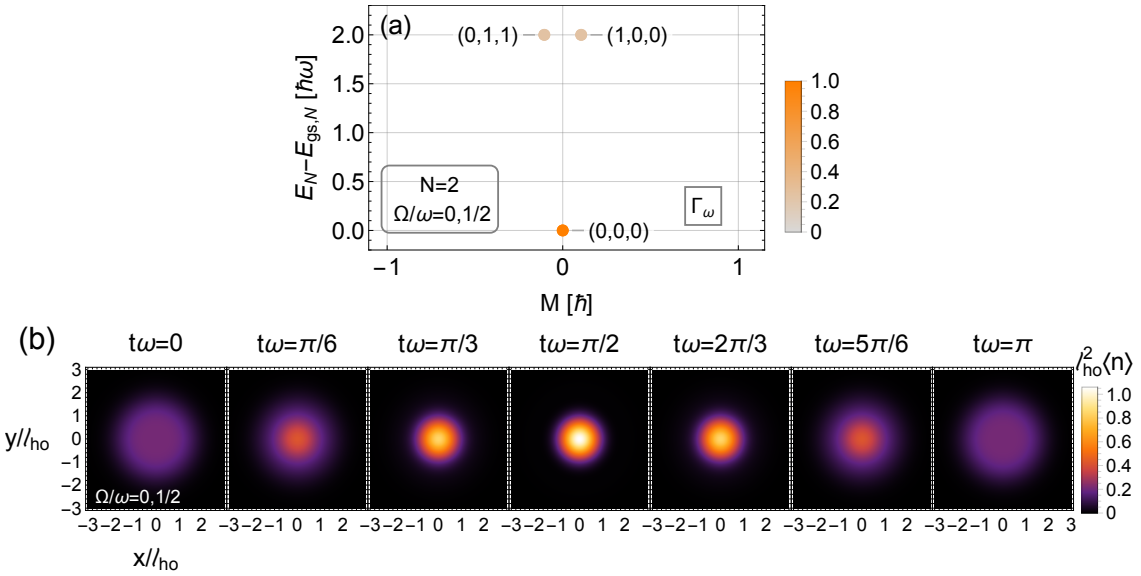

Figure 4.13: Excitation spectrum upon an isotropic frequency perturbation $\delta\omega$ for $N = 2$ particles in (a) and (b) for $\Omega/\omega = 0$ and $\Omega/\omega = 1/2$ respectively. The color coding refers to the relative strength of the transition matrix elements of Γ_ω in Eq. (2.147) starting in the ground state. Only states with non-zero overlap are shown and overlapping points are moved horizontally. The numbers are (a, b, c), referring to the number of times a state has been acted on by $R^\dagger$ and $Q^\dagger_\pm$ according to Eq. (2.82). Note that these are all states the transition matrix Γ_ω can connect the ground state to (in Fig. 4.10). Furthermore, it connects only to center-of-mass excitations and internal breathing modes within the same conformal tower. This is also the breathing mode created by the $L^\dagger$ operator in Eq. (2.61). (c) Show the corresponding time evolution of the density of the resulting state $|\Psi\rangle = \Gamma_\omega|gs\rangle$ for the two rotation frequencies $\Omega/\omega = 0$ and $\Omega/\omega = 1/2$.

4.4.4 Interaction Strength Perturbation

In this section, we show the results of perturbing the interaction strength δg, as discussed in Sec. 2.7.4. In Fig. 4.14, the excitation spectrum with only states that are connected to the ground state (see Fig. 4.10) is shown. The corresponding time evolution of the density of the resulting state is also shown. As discussed in Sec. 2.7.4, the perturbation connects the ground state to arbitrary excitation levels. Thus we introduce a cut-off energy $\hbar\omega_{cut}$ in order to illustrate the results. For $N = 2$, there are no new primary states at $M = 0$, meaning that only internal breathing modes, within the same conformal tower, can be excited. Note, however, that for $N > 2$, the transition matrix Γ_g can connect states between different primary states as well. Furthermore, it is interesting to note that the transition rate does not decay for higher excitation levels for $N = 2$. This is in contrast to any other particle number $N > 2$, for which the transition rate decay with higher energy.

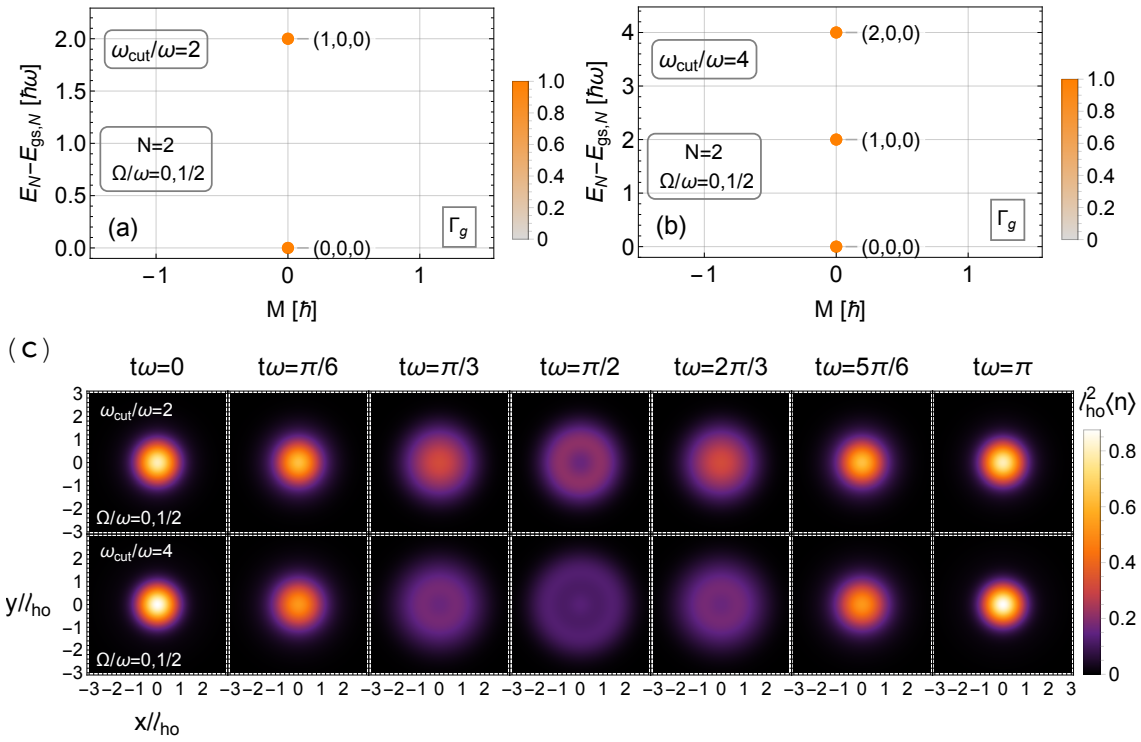

Figure 4.14: Excitation spectrum upon an interaction perturbation δg for $N = 2$ particles in (a) and (b) for cut-off frequencies $\omega_{cut}/\omega = 2$ and $\omega_{cut}/\omega = 4$, respectively. The color coding refers to the relative strength of the transition matrix elements of Γ_g in Eq. (2.147) starting in the ground state. Only states with non-zero overlap are shown. The numbers are (a, b, c), referring to the number of times a state has been acted on by $R^\dagger$ and $Q^\dagger_\pm$ according to Eq. (2.82). Note that there are no new primary states at $M = 0$ for $N = 2$ (see Fig. 4.10), which is why only the internal breathing mode excitation is excited. However, this is not the case in general for $N > 2$. That the transition matrix Γ_g can only excite internal breathing modes or primary states, is, in general, true, however. Another thing to note is that the transition rate does not decay for $N = 2$ at higher excitation levels. This is only true for $N = 2$. (c) Shows the corresponding time evolution of the density of the resulting state $|\Psi\rangle = \Gamma_\omega|gs\rangle$ for the two cut-off frequencies $\omega_{cut}/\omega = 2$ (c.f. to Fig 4.1) and $\omega_{cut}/\omega = 4$.

5
Conclusion

In summary, we have demonstrated that rotating two-dimensional mesoscopic Fermi gases at weak interactions possess a nonrelativistic conformal symmetry. Although much of the literature on interacting two-dimensional Fermi gases focuses on how the invariance is subtly broken by a quantum anomaly at strong interactions [20–28, 41]), it was argued in [29] and here that a conformal window exists at weak interactions. The symmetry predicts so-called conformal towers formed by primary states and their center-of-mass and breathing mode excitations, the latter having an excitation energy at exactly twice the harmonic oscillator energy. With degenerate many-body perturbation theory and exact diagonalization, a protocol to compute primary states and their conformal towers was developed. By studying the resulting energy spectrum, the conformal tower structure could be unraveled. From the diagonalization, the perturbative states were used together with Monte Carlo simulations to compute and confirm the hyperradial distribution of the many-body wave function predicted by the symmetry. The hyperradial distribution should be observable experimentally by sampling the many-body wave function with recently developed single-particle imaging techniques [12, 13], thus verifying the conformal symmetry on a microscopic level. To the best of the author's knowledge, the results of this thesis together with a previous work of the author [29] is the first time the conformal tower structure has been explicitly verified exactly.

The rotation has two effects on the system. First: it lowers the energy of single-particle energy eigenstates with angular momentum in the direction of rotation while raising the energy of states with angular momentum in the opposite direction. As the rotation frequency approaches the trapping frequency, the single-particle energy eigenstates are rearranged such that Landau levels are formed. Second: it rearranges the positions of primary states. This means that the ground state properties in general change as a function of rotation.

Furthermore, both internal breathing mode and center-of-mass excitations, the latter corresponding to stirring the gas either clockwise or anti-clockwise, were illustrated by computing the density of the superposition of states obtained by the diagonalization routine.

Last, different ways of perturbing the system such as to induce a transition between states were discussed. The conformal symmetry predicts that perturbing the trap center or the trap frequency isotropically can only connect states within the same conformal tower, and this was verified by the numerics. Furthermore, per-

turbing the interaction strength only affect the internal dynamics and only connects different primary states or internal breathing mode excitations. Perturbing the trap frequency anisotropically connects different primary states, breathing modes, or center-of-mass excitations.

Further exploring ground state properties as a function of rotation frequency for larger particle numbers is a possible extension for future research. Since the ground state is often prepared experimentally [11, 13, 38], a great motivation for future research is to propose a way to measure the angular momentum change of the ground state experimentally. For these purposes, computing the pair correlation function would be an interesting starting point.

Another interesting extension would be to compute the energy spectrum of an anisotropic trap $\omega_x \neq \omega_y$ to see what happens to the primary states when the conformal symmetry is broken. Intuitively, the conformal symmetry is broken because two length scales enter, one for each oscillator direction, which breaks scale invariance.

Bibliography

[1] M. Srednicki, *Quantum Field Theory*. Cambridge University Press, 2007.

[2] J. M. Ziman, *Principles of the Theory of Solids*, 2nd ed. Cambridge University Press, 1972.

[3] J. Cardy, *Scaling and renormalization in Statistical Physics*. Cambridge University Press, 2002.

[4] D. J. Amit and M. Martín-Mayor, *Field Theory, the Renormalization Group, and Critical Phenomena*. World Scientific, 2006.

[5] F. Werner and Y. Castin, "Unitary gas in an isotropic harmonic trap: Symmetry properties and applications," *Phys. Rev. A*, vol. 74, p. 053604, Nov 2006. [Online]. Available: https://link.aps.org/doi/10.1103/PhysRevA.74.053604

[6] Y. Castin and F. Werner, "The unitary gas and its symmetry properties," in *The BCS-BEC Crossover and the Unitary Fermi Gas*. Springer Berlin Heidelberg, oct 2011, pp. 127–191.

[7] M. J. H. Ku, A. T. Sommer, L. W. Cheuk, and M. W. Zwierlein, "Revealing the Superfluid Lambda Transition in the Universal Thermodynamics of a Unitary Fermi Gas," *Science*, vol. 335, no. 6068, p. 563, 2012.

[8] K. Van Houcke, F. Werner, E. Kozik, N. Prokof'ev, B. Svistunov, M. J. H. Ku, A. T. Sommer, L. W. Cheuk, A. Schirotzek, and M. W. Zwierlein, "Feynman diagrams versus Fermi-gas Feynman emulator," *Nature Physics*, vol. 8, no. 5, p. 366, 2012.

[9] D. T. Son, "Vanishing Bulk Viscosities and Conformal Invariance of the Unitary Fermi Gas," *Phys. Rev. Lett.*, vol. 98, p. 020604, Jan 2007.

[10] T. Schäfer and C. Chafin, "Scaling Flows and Dissipation in the Dilute Fermi Gas at Unitarity," in *The BCS–BEC Crossover and the Unitary Fermi Gas*, W. Zwerger, Ed. Springer-Verlag (Berlin), 2012.

[11] L. Bayha, M. Holten, R. Klemt, K. Subramanian, J. Bjerlin, S. M. Reimann, G. M. Bruun, P. M. Preiss, and S. Jochim, "Observing the emergence of a quantum phase transition shell by shell," *Nature*, vol. 587, pp. 583–587, 2020. [Online]. Available: https://doi.org/10.1038/s41586-020-2936-y

[12] M. Holten, L. Bayha, K. Subramanian, C. Heintze, P. M. Preiss, and S. Jochim, "Observation of pauli crystals," *Phys. Rev. Lett.*, vol. 126, p. 020401, Jan 2021. [Online]. Available: https://link.aps.org/doi/10.1103/PhysRevLett.126.020401

[13] M. Holten, L. Bayha, K. Subramanian, S. Brandstetter, C. Heintze, P. Lunt, P. M. Preiss, and S. Jochim, "Observation of Cooper pairs in a mesoscopic two-dimensional Fermi gas," *Nature*, vol. 606, pp. 287–291, 2022. [Online]. Available: https://doi.org/10.1038/s41586-022-04678-1

[14] I. Bloch, J. Dalibard, and W. Zwerger, "Many-body physics with ultracold gases," *Rev. Mod. Phys.*, vol. 80, pp. 885–964, Jul 2008. [Online]. Available: https://link.aps.org/doi/10.1103/RevModPhys.80.885

[15] D. Son and M. Wingate, "General coordinate invariance and conformal invariance in nonrelativistic physics: Unitary fermi gas," *Annals of Physics*, vol. 321, no. 1, pp. 197–224, jan 2006. [Online]. Available: https://doi.org/10.1016%2Fj.aop.2005.11.001

[16] T. Mehen, I. W. Stewart, and M. B. Wise, "Conformal invariance for non-relativistic field theory," *Physics Letters B*, vol. 474, no. 1-2, pp. 145–152, feb 2000. [Online]. Available: https://doi.org/10.1016%2Fs0370-2693%2800%2900006-x

[17] Y. Nishida and D. T. Son, "Nonrelativistic conformal field theories," *Physical Review D*, vol. 76, no. 8, oct 2007. [Online]. Available: https://doi.org/10.1103%2Fphysrevd.76.086004

[18] J. Hofmann, "Quantum anomaly, universal relations, and breathing mode of a two-dimensional fermi gas," *Phys. Rev. Lett.*, vol. 108, p. 185303, May 2012. [Online]. Available: https://link.aps.org/doi/10.1103/PhysRevLett.108.185303

[19] M. Olshanii, H. Perrin, and V. Lorent, "Example of a quantum anomaly in the physics of ultracold gases," *Phys. Rev. Lett.*, vol. 105, p. 095302, Aug 2010. [Online]. Available: https://link.aps.org/doi/10.1103/PhysRevLett.105.095302

[20] E. Vogt, M. Feld, B. Fröhlich, D. Pertot, M. Koschorreck, and M. Köhl, "Scale invariance and viscosity of a two-dimensional fermi gas," *Phys. Rev. Lett.*, vol. 108, p. 070404, Feb 2012. [Online]. Available: https://link.aps.org/doi/10.1103/PhysRevLett.108.070404

[21] C. Gao and Z. Yu, "Breathing mode of two-dimensional atomic fermi gases in harmonic traps," *Phys. Rev. A*, vol. 86, p. 043609, Oct 2012. [Online]. Available: https://link.aps.org/doi/10.1103/PhysRevA.86.043609

[22] C. Chafin and T. Schäfer, "Scale breaking and fluid dynamics in a dilute two-dimensional fermi gas," *Phys. Rev. A*, vol. 88, p. 043636, Oct 2013. [Online]. Available: https://link.aps.org/doi/10.1103/PhysRevA.88.043636

[23] T. Peppler, P. Dyke, M. Zamorano, I. Herrera, S. Hoinka, and C. J. Vale, "Quantum anomaly and 2d-3d crossover in strongly interacting fermi

gases," *Phys. Rev. Lett.*, vol. 121, p. 120402, Sep 2018. [Online]. Available: https://link.aps.org/doi/10.1103/PhysRevLett.121.120402

[24] J. E. Drut, J. R. McKenney, W. S. Daza, C. L. Lin, and C. R. Ordóñez, "Quantum anomaly and thermodynamics of one-dimensional fermions with three-body interactions," *Phys. Rev. Lett.*, vol. 120, p. 243002, Jun 2018. [Online]. Available: https://link.aps.org/doi/10.1103/PhysRevLett.120.243002

[25] B. C. Mulkerin, X.-J. Liu, and H. Hu, "Collective modes of a two-dimensional fermi gas at finite temperature," *Phys. Rev. A*, vol. 97, p. 053612, May 2018. [Online]. Available: https://link.aps.org/doi/10.1103/PhysRevA.97.053612

[26] W. Daza, J. E. Drut, C. Lin, and C. Ordóñez, "Virial expansion for the tan contact and beth-uhlenbeck formula from two-dimensional so(2,1) anomalies," *Phys. Rev. A*, vol. 97, p. 033630, Mar 2018. [Online]. Available: https://link.aps.org/doi/10.1103/PhysRevA.97.033630

[27] H. Hu, B. C. Mulkerin, U. Toniolo, L. He, and X.-J. Liu, "Reduced quantum anomaly in a quasi-two-dimensional fermi superfluid: Significance of the confinement-induced effective range of interactions," *Phys. Rev. Lett.*, vol. 122, p. 070401, Feb 2019. [Online]. Available: https://link.aps.org/doi/10.1103/PhysRevLett.122.070401

[28] X. Y. Yin, H. Hu, and X.-J. Liu, "Few-body perspective of a quantum anomaly in two-dimensional fermi gases," *Phys. Rev. Lett.*, vol. 124, p. 013401, Jan 2020. [Online]. Available: https://link.aps.org/doi/10.1103/PhysRevLett.124.013401

[29] V. Bekassy and J. Hofmann, "Nonrelativistic conformal invariance in mesoscopic two-dimensional Fermi gases," *Phys. Rev. Lett.*, vol. 128, p. 193401, May 2022. [Online]. Available: https://link.aps.org/doi/10.1103/PhysRevLett.128.193401

[30] J. Hofmann and W. Zwerger, "Universal relations for dipolar quantum gases," *Phys. Rev. Res.*, vol. 3, p. 013088, Jan 2021. [Online]. Available: https://link.aps.org/doi/10.1103/PhysRevResearch.3.013088

[31] A. Bergschneider, V. M. Klinkhamer, J. H. Becher, R. Klemt, G. Zürn, P. M. Preiss, and S. Jochim, "Spin-resolved single-atom imaging of ^{6}Li in free space," *Phys. Rev. A*, vol. 97, p. 063613, Jun 2018. [Online]. Available: https://link.aps.org/doi/10.1103/PhysRevA.97.063613

[32] J. J. Sakurai and J. Napolitano, *Modern Quantum Mechanics*, 2nd ed. Cambridge University Press, 2017.

[33] K. Schulten, "Notes on Quantum Mechanics," 2000. [Online]. Available: https://www.ks.uiuc.edu/Services/Class/PHYS481/lecture.html

[34] G. Zürn, "Few-fermion systems in one dimension." Ph.D. Dissertation, Heidelberg University, 2012. [Online]. Available: http://www.ub.uni-heidelberg.de/archiv/14496

[35] T. Busch, B.-G. Englert, K. Rzążewski, and M. Wilkens, "Two cold atoms in a harmonic trap," *Foundations of Physics*, vol. 28, p. 549–559, Apr 1998. [Online]. Available: https://doi.org/10.1023/A:1018705520999

[36] E. Tiesinga, B. J. Verhaar, and H. T. C. Stoof, "Threshold and resonance phenomena in ultracold ground-state collisions," *Phys. Rev. A*, vol. 47, pp. 4114–4122, May 1993. [Online]. Available: https://link.aps.org/doi/10.1103/PhysRevA.47.4114

[37] D. S. Petrov and G. V. Shlyapnikov, "Interatomic collisions in a tightly confined bose gas," *Phys. Rev. A*, vol. 64, p. 012706, Jun 2001. [Online]. Available: https://link.aps.org/doi/10.1103/PhysRevA.64.012706

[38] L. P. Pitaevskii and A. Rosch, "Breathing modes and hidden symmetry of trapped atoms in two dimensions," *Phys. Rev. A*, vol. 55, pp. R853–R856, Feb 1997. [Online]. Available: https://link.aps.org/doi/10.1103/PhysRevA.55.R853

[39] W. Kohn, "Cyclotron resonance and de haas-van alphen oscillations of an interacting electron gas," *Phys. Rev.*, vol. 123, pp. 1242–1244, Aug 1961. [Online]. Available: https://link.aps.org/doi/10.1103/PhysRev.123.1242

[40] S. Moroz, "Scale-invariant fermi gas in a time-dependent harmonic potential," *Phys. Rev. A*, vol. 86, p. 011601, Jul 2012. [Online]. Available: https://link.aps.org/doi/10.1103/PhysRevA.86.011601

[41] M. Holten, L. Bayha, A. C. Klein, P. A. Murthy, P. M. Preiss, and S. Jochim, "Anomalous breaking of scale invariance in a two-dimensional fermi gas," *Phys. Rev. Lett.*, vol. 121, p. 120401, Sep 2018. [Online]. Available: https://link.aps.org/doi/10.1103/PhysRevLett.121.120401

[42] O. M. Maragò, S. A. Hopkins, J. Arlt, E. Hodby, G. Hechenblaikner, and C. J. Foot, "Observation of the scissors mode and evidence for superfluidity of a trapped bose-einstein condensed gas," *Phys. Rev. Lett.*, vol. 84, pp. 2056–2059, Mar 2000. [Online]. Available: https://link.aps.org/doi/10.1103/PhysRevLett.84.2056

[43] D. Guéry-Odelin and S. Stringari, "Scissors mode and superfluidity of a trapped bose-einstein condensed gas," *Phys. Rev. Lett.*, vol. 83, pp. 4452–4455, Nov 1999. [Online]. Available: https://link.aps.org/doi/10.1103/PhysRevLett.83.4452

[44] E. Vogt, M. Feld, B. Fröhlich, D. Pertot, M. Koschorreck, and M. Köhl, "Scale invariance and viscosity of a two-dimensional fermi gas," *Phys. Rev. Lett.*, vol. 108, p. 070404, Feb 2012. [Online]. Available: https://link.aps.org/doi/10.1103/PhysRevLett.108.070404

A

Appendix: Matrix Elements

This section discusses matrix elements in occupation number representation.

A.1 Interaction Matrix Elements

Here, the matrix elements for the interaction operator

$$H^{(1)} = \sum_{i=1}^{N_\uparrow} \sum_{j=1}^{N_\downarrow} \delta^{(2)} \left(\mathbf{r}_{i\uparrow} - \mathbf{r}_{j\downarrow} \right) \tag{A.1}$$

is determined. In occupation number representation

$$H^{(1)} = g \sum_{i,j,k,l} w_{ijkl} c_{i\uparrow}^\dagger c_{j\downarrow}^\dagger c_{l\downarrow} c_{k\uparrow}, \tag{A.2}$$

with the two-particle matrix elements

$$\begin{aligned} w_{ijkl} &= \int d^2r \, \psi_i^*(\mathbf{r}) \psi_j^*(\mathbf{r}) \psi_k(\mathbf{r}) \psi_l(\mathbf{r}) \\ &= \int_0^{2\pi} d\varphi \, e^{i(m_k + m_l - m_i - m_j)} \int_0^\infty r dr \, \psi_i(r) \psi_j(r) \psi_k(r) \psi_l(r) \\ &= 2\pi \delta_{m_k + m_l, m_i + m_j} \int_0^\infty r dr \, \psi_i(r) \psi_j(r) \psi_k(r) \psi_l(r), \end{aligned} \tag{A.3}$$

where $\psi_s(\mathbf{r})$ is given in Eq. (2.7). It can be seen from the Kronecker delta that the interaction preserves angular momentum. The integral of the single-particle wave functions which involve Laguerre polynomials is solved numerically with Mathematica.

Furthermore, consider the many-body matrix elements $\langle \Psi(\mathcal{N}') | c_{i\uparrow}^\dagger c_{j\downarrow}^\dagger c_{l\downarrow} c_{k\uparrow} | \Psi(\mathcal{N}) \rangle$. There are four non-zero cases depending on the number of single-particle occupancies that differ.

- Case 1): $i \neq k, j \neq l$

$$\begin{aligned} \langle \Psi(\mathcal{N}') | c_{i\uparrow}^\dagger c_{j\downarrow}^\dagger c_{l\downarrow} c_{k\uparrow} | \Psi(\mathcal{N}) \rangle &= \left(c_{j\downarrow} c_{i\uparrow} | \Psi(\mathcal{N}') \rangle \right)^\dagger c_{l\downarrow} c_{k\uparrow} | \Psi(\mathcal{N}) \rangle \\ &= (-1)^{q_i' + q_j' + q_l + q_k} n_{i\uparrow}' n_{j\uparrow}' n_{l\downarrow} n_{k\downarrow} \\ &\quad \times \delta_{n_{i\uparrow}', n_{i\uparrow}+1} \delta_{n_{j\downarrow}', n_{j\downarrow}+1} \delta_{n_{l\downarrow}', n_{i\downarrow}-1} \delta_{n_{k\uparrow}', n_{k\uparrow}-1} \\ &\quad \times \prod_{\substack{s \\ s \neq i,k}} \delta_{n_{s\uparrow}', n_{s\uparrow}} \prod_{\substack{s \\ s, \neq j,l}} \delta_{n_{s\downarrow}', n_{s\downarrow}}, \end{aligned} \tag{A.4}$$

where Eq. (2.26) has been used repeatedly in going to the second line, and the Kronecker deltas (δ_{ij}) comes from the orthonormality in Eq. (2.21). From the Kronecker deltas, it can be seen that $\mathcal{N}', \mathcal{N}$ must differ by two occupancies, or exactly four occupation numbers $n_{i\uparrow}, n_{j\downarrow}, n_{l\downarrow}, n_{k\uparrow}$. Thus, the matrix elements for case 1) can be written as

$$\Psi(\mathcal{N}')|H^{(1)}|\Psi(\mathcal{N})\rangle = g(-1)^{q_i'+q_j'+q_l+q_k}(1-n_{i\uparrow})(1-n_{j\downarrow})n_{l\downarrow}n_{k\uparrow}w_{ijkl}. \tag{A.5}$$

- Case 2): $i \neq k, j = l$,

$$\begin{aligned}\langle\Psi(\mathcal{N}')|c_{i\uparrow}^\dagger c_{j\downarrow}^\dagger c_{j\downarrow}c_{k\uparrow}|\Psi(\mathcal{N})\rangle &= \langle\Psi(\mathcal{N}')|c_{i\uparrow}^\dagger c_{k\uparrow}c_{j\downarrow}^\dagger c_{j\downarrow}|\Psi(\mathcal{N})\rangle \\ &= n_{j\downarrow}\left(c_{i\uparrow}|\Psi(\mathcal{N}')\rangle\right)^\dagger c_{k\uparrow}|\Psi(\mathcal{N})\rangle \\ &= n_{j\downarrow}(-1)^{q_i'+q_k}n_{i\uparrow}'n_{k\downarrow}\delta_{n_{i\uparrow}',n_{i\uparrow}+1}\delta_{n_{k\uparrow}',n_{k\uparrow}-1} \\ &\quad\times\prod_{\substack{s\\ s\neq i,k}}\delta_{n_{s\uparrow}',n_{s\uparrow}}\prod_s\delta_{n_{s\downarrow}',n_{s\downarrow}},\end{aligned} \tag{A.6}$$

where the anti-commutation relations in Eq. (2.22) was used to move $c_{k\uparrow}$ in the first step, Eq. (2.27) was used to evaluate the number operator $c_{j\downarrow}^\dagger c_{j\downarrow}$ in the going to the second line, and Eq. (2.26), (2.21) in going to the last line. From the Kronecker deltas, it can be seen $\mathcal{N}', \mathcal{N}$ must differ by one spin up occupancy, or exactly two occupation numbers $n_{i\uparrow}, n_{k\uparrow}$. Thus the matrix elements for case 2) can be written as

$$\Psi(\mathcal{N}')|H^{(1)}|\Psi(\mathcal{N})\rangle = g\sum_j n_{j\downarrow}(-1)^{q_i'+q_k}(1-n_{i\uparrow})n_{k\uparrow}w_{ijkj}. \tag{A.7}$$

- Case 3): $i = k, j \neq l$ is identical to Case 2) but with $j \leftrightarrow i, l \leftrightarrow k$, i.e. exactly one spin down occupation differ

$$\Psi(\mathcal{N}')|H^{(1)}|\Psi(\mathcal{N})\rangle = g\sum_i n_{i\uparrow}(-1)^{q_j'+q_l}(1-n_{j\downarrow})n_{l\downarrow}w_{ijil}. \tag{A.8}$$

- Case 4): $i = k, j = l$

$$\langle\Psi(\mathcal{N}')|c_{i\uparrow}^\dagger c_{j\downarrow}^\dagger c_{j\downarrow}c_{i\uparrow}|\Psi(\mathcal{N})\rangle = \langle\Psi(\mathcal{N}')|c_{i\uparrow}^\dagger c_{i\uparrow}c_{j\downarrow}^\dagger c_{j\downarrow}|\Psi(\mathcal{N})\rangle = n_{i\uparrow}n_{j\downarrow}\prod_{s\sigma}\delta_{n_{s\sigma}'\sigma}\delta_{n_s\sigma} \tag{A.9}$$

where the anti-commutation relations in Eq. (2.22) was used to move $c_{i\uparrow}$ in the first step, Eq. (2.27) was used to evaluate the number operators $c_{j\downarrow}^\dagger c_{j\downarrow}, c_{i\uparrow}^\dagger c_{i\uparrow}$ and Eq. (2.21) to obtain the Kronecker deltas. Thus, we see from the Kronecker deltas that $\mathcal{N}' = \mathcal{N}$, i.e. the diagonal elements which become

$$\langle\Psi(\mathcal{N})|H^{(1)}|\Psi(\mathcal{N})\rangle = g\sum_{i,j} n_{i\uparrow}n_{j\downarrow}w_{ijij}. \tag{A.10}$$

The matrix elements are summarized below.

Cases	$\langle\Psi(\mathcal{N}')\lvert H^{(1)}\rvert\Psi(\mathcal{N})\rangle$	Occupancy differing
Case 1)	$g(-1)^{q_i'+q_j'+q_l+q_k}(1-n_{i\uparrow})(1-n_{j\downarrow})n_{l\downarrow}n_{k\uparrow}w_{ijkl}$	$i\neq k, j\neq l$
Case 2)	$g\sum_j n_{j\downarrow}(-1)^{q_i'+q_k}(1-n_{i\uparrow})n_{k\uparrow}w_{ijkj}$	$i\neq k$
Case 3)	$g\sum_i n_{i\uparrow}(-1)^{q_j'+q_l}(1-n_{j\downarrow})n_{l\downarrow}w_{ijil}$	$j\neq l$
Case 4)	$g\sum_{i,j} n_{i\uparrow}n_{j\downarrow}w_{ijij}$	None

Table A.1: Matrix elements for the interaction operator in Eq. (A.1). The overlap integrals w_{ijkl} are given in Eq. (A.3). The factors q_i, q_i' refer to the number of times the anti-commutation relations in (2.22) must be used in order to bring the creation operator $c^\dagger_{i(\uparrow/\downarrow)}$ to the first position in $|\Psi(\mathcal{N})\rangle$ and $|\Psi(\mathcal{N}')\rangle$ respectively.

A.2 Anisotropic Frequency Perturbation Matrix Elements

In this section, we state the results of the matrix elements of the single-particle operator in Eq. (2.151) of an anisotropic frequency perturbation discussed in Sec. 2.7.1. The results are stated below:

- $\Delta M = 0$:

$$\langle\psi_i|\gamma_{\omega_x}|\psi_j\rangle = (\hbar\delta\omega_x)\frac{\delta_{m_i m_j}}{2}\Big((2n_i+|m_i|+1)\delta_{n_i,n_j} - \sqrt{n_i(n_i+|m_i|)}\delta_{n_i-1,n_j} - \sqrt{(n_i+1)(n_i+|m_i|+1)}\delta_{n_i+1,n_j}\Big) \tag{A.11}$$

  Here, it can be noted that single-particle states that are connected are
  $(n_i,m_i)=(n_j,m_j)\rightarrow \Delta E_N^{(0)}=0$, or
  $(n_i,m_i)=(n_j\pm 1,m_j)\rightarrow \Delta E_N^{(0)}=\pm 2\hbar\omega$,
  where $E_N^{(0)}$ denote the non-interacting energy contribution in Eq. (2.33).
- $\Delta M = +2$: Now the matrix elements depend on the values of m_i.

  ■ $m_i \geq 2$:

$$\langle\psi_i|\gamma_{\omega_x}|\psi_j\rangle = (\hbar\delta\omega_x)\frac{\delta_{m_i-2,m_j}}{4}\Big(\sqrt{(n_i+|m_i|)(n_i+|m_i|-1)}\delta_{n_i,n_j} - 2\sqrt{(n_i+1)(n_i+|m_i|)}\delta_{n_i,n_j-1} + \sqrt{(n_i+2)(n_i+1)}\delta_{n_i,n_j-2}\Big), \tag{A.12}$$

  where we note that single-particle states that are connected are only
  $(n_i,m_i)=(n_j,m_j+2)\rightarrow \Delta E_N^{(0)}=2\hbar(\omega-\Omega)$, or
  $(n_i,m_i)=(n_j-1,m_j+2)\rightarrow \Delta E_N^{(0)}=-2\hbar\Omega$, or
  $(n_i,m_i)=(n_j-2,m_j+2)\rightarrow \Delta E_N^{(0)}=-2\hbar(\omega+\Omega)$.

- $m_i = 1$:

$$\langle\psi_i|\gamma_{\omega_x}|\psi_j\rangle = (\hbar\delta\omega_x)\frac{\delta_{m_i-2,m_j}}{4}\Big((2n_i+|m_i|+1)\delta_{n_i,n_j} - \sqrt{(n_i+1)(n_i+|m_i|+1)}\delta_{n_i,n_j-1}\delta_{n_i,n_j-1} - \sqrt{n_i(n_i+1)}\delta_{n_i,n_j+1}\Big), \tag{A.13}$$

where we this time note that single-particle states that are connected are only $(n_i, m_i = 1) = (n_j, m_j = -1) \to \Delta E_N^{(0)} = -2\hbar\Omega$, or
$(n_i, m_i = 1) = (n_j - 1, m_j = -1) \to \Delta E_N^{(0)} = -2\hbar(\omega + \Omega)$, or
$(n_i, m_i = 1) = (n_j + 1, m_j = -1) \to \Delta E_N^{(0)} = 2\hbar(\omega - \Omega)$.

- $m_i \leq 0$:

$$\langle\psi_i|\gamma_{\omega_x}|\psi_j\rangle = (\hbar\delta\omega_x)\frac{\delta_{m_i-2,m_j}}{4}\Big(\sqrt{(n_i+|m_i|+2)(n_i+|m_i|+1)}\delta_{n_i,n_j} - 2\sqrt{n_r(n_i+|m_i|+1)}\delta_{n_i,n_j+1} + \sqrt{n_i(n_i-1)}\delta_{n_i,n_i+2}\Big), \tag{A.14}$$

noting that single-particle states that are connected are only
$(n_i, m_i) = (n_j, m_j + 2) \to \Delta E_N^{(0)} = -2\hbar(\omega + \Omega)$, or
$(n_i, m_i) = (n_j + 1, m_j + 2) \to \Delta E_N^{(0)} = -2\hbar\Omega$, or
$(n_i, m_i) = (n_j + 2, m_j + 2) \to \Delta E_N^{(0)} = 2\hbar(\omega - \Omega)$.

- $\Delta M = -2$: Now the matrix elements again depend on the values of m_i.

- $m_i \leq -2$:

$$\langle\psi_i|\gamma_{\omega_x}|\psi_j\rangle = (\hbar\delta\omega_x)\frac{\delta_{m_i+2,m_j}}{4}\Big(\sqrt{(n_i+|m_i|)(n_i+|m_i|-1)}\delta_{n_i,n_j} - 2\sqrt{(n_i+1)(n_i+|m_i|)}\delta_{n_i,n_j-1} + \sqrt{(n_i+2)(n_i+1)}\delta_{n_i,n_j-2}\Big), \tag{A.15}$$

where we note that single-particle states that are connected are only
$(n_i, m_i) = (n_j, m_j - 2) \to \Delta E_N^{(0)} = 2\hbar(\omega + \Omega)$, or
$(n_i, m_i) = (n_j - 1, m_j - 2) \to \Delta E_N^{(0)} = 2\hbar\Omega$, or
$(n_i, m_i) = (n_j - 2, m_j - 2) \to \Delta E_N^{(0)} = -2\hbar(\omega - \Omega)$.

- $m_i = -1$:

$$\langle\psi_i|\gamma_{\omega_x}|\psi_j\rangle = (\hbar\delta\omega_x)\frac{\delta_{m_i+2,m_j}}{4}\Big((2n_i+|m_i|+1)\delta_{n_i,n_j} - \sqrt{(n_i+1)(n_i+|m_i|+1)}\delta_{n_i,n_j-1}\delta_{n_i,n_j-1} - \sqrt{n_i(n_i+1)}\delta_{n_i,n_j+1}\Big), \tag{A.16}$$

where we this time note that single-particle states that are connected are only
$(n_i, m_i = -1) = (n_j, m_j = 1) \rightarrow \Delta E_N^{(0)} = 2\hbar\Omega$, or
$(n_i, m_i = -1) = (n_j - 1, m_j = 1) \rightarrow \Delta E_N^{(0)} = -2\hbar(\omega - \Omega)$, or
$(n_i, m_i = -1) = (n_j + 1, m_j = 1) \rightarrow \Delta E_N^{(0)} = 2\hbar(\omega + \Omega)$.

- $m_i \geq 0$:

$$\langle\psi_i|\gamma_{\omega_x}|\psi_j\rangle = (\hbar\delta\omega_x)\frac{\delta_{m_i+2,m_j}}{4}\Big(\sqrt{(n_i + |m_i| + 2)(n_i + |m_i| + 1)}\delta_{n_i,n_j} - 2\sqrt{n_r(n_i + |m_i| + 1)}\delta_{n_i,n_j+1} + \sqrt{n_i(n_i - 1)}\delta_{n_i,n_i+2}\Big), \tag{A.17}$$

noting that single-particle states that are connected are only
$(n_i, m_i) = (n_j, m_j - 2) \rightarrow \Delta E_N^{(0)} = -2\hbar(\omega - \Omega)$, or
$(n_i, m_i) = (n_j + 1, m_j - 2) \rightarrow \Delta E_N^{(0)} = 2\hbar\Omega$, or
$(n_i, m_i) = (n_j + 2, m_j - 2) \rightarrow \Delta E_N^{(0)} = 2\hbar(\omega + \Omega)$.

To summarize, we see that an anisotropic perturbation Γ_{ω_x} in the trapping frequency $\delta\omega_x$ can only leave the angular momentum unchanged $\Delta M = 0$ or change it by $\Delta M = \pm 2$. If we consider a non-degenerate ground state, we can see that when Γ_{ω_x} leaves angular momentum unchanged, $\Delta M = 0$, it will only connect the ground state to either itself $\Delta E^{(0)} = 0$, or to states at the non-interacting excitation level $\Delta E_N^{(0)} = 2\hbar\omega$. Further, when Γ_{ω_x} changes angular momentum by $\Delta M = 2$, it connect the non-degenerate ground state to excitation level $\Delta E^{(0)} = 2\hbar(\omega - \Omega)$. Similarly, changing $\Delta M = -2$ connects to $\Delta E^{(0)} = 2\hbar(\omega + \Omega)$, but also to $\Delta E^{(0)} = 2\hbar\Omega$.

A.3 Trap Center Perturbation Matrix Elements

In this section, we state the results of the matrix elements of the single-particle operator in Eq. (2.154) of a trap center perturbation discussed in Sec. 2.7.2. The results are stated below:

- $\Delta M = 1$: the matrix elements depends on if $m_i > 0$ or $m_i \leq 0$
  - $m_i > 0$

$$\langle\psi_i|\gamma_{x_0}|\psi_j\rangle = \hbar\omega\frac{\delta x_0}{\ell_{ho}}\frac{\delta_{m_i-1,m_j}}{2}\Big(\sqrt{n_i + |m_i|}\delta_{n_i,n_j} - \sqrt{n_i + 1}\delta_{n_i,n_j-1}\Big), \tag{A.18}$$

where we note that single-particle states that are connected are
$(n_i, m_i) = (n_j, m_j + 1) \rightarrow \Delta E_N^{(0)} = \hbar(\omega - \Omega)$, or
$(n_i, m_i) = (n_j - 1, m_j) \rightarrow \Delta E_N^{(0)} = -\hbar(\omega + \Omega)$,
where $E_N^{(0)}$ denote the non-interacting energy contribution in Eq. (2.33).

  - $m_i \leq 0$

$$\langle\psi_i|\gamma_{x_0}|\psi_j\rangle = \hbar\omega\frac{\delta x_0}{\ell_{ho}}\frac{\delta_{m_i-1,m_j}}{2}\Big(\sqrt{n_i + |m_i| + 1}\delta_{n_i,n_j} - \sqrt{n_i}\delta_{n_i,n_j+1}\Big), \tag{A.19}$$

where the single-particle states that are connected are
$(n_i, m_i) = (n_j, m_j + 1) \rightarrow \Delta E_N^{(0)} = -\hbar(\omega + \Omega)$, or
$(n_i, m_i) = (n_j + 1, m_j) \rightarrow \Delta E_N^{(0)} = \hbar(\omega - \Omega)$.

- $\Delta M - 1$: the matrix elements depends on if $m_i \geq 0$ or $m_i < 0$
  - $m_i < 0$

$$\langle \psi_i | \gamma_{x_0} | \psi_j \rangle = \hbar\omega \frac{\delta x_0}{\ell_{ho}} \frac{\delta_{m_i+1,m_j}}{2} \left(\sqrt{n_i + |m_i|}\delta_{n_i,n_j} - \sqrt{n_i + 1}\delta_{n_i,n_j-1} \right), \tag{A.20}$$

where the single-particle states that are connected are
$(n_i, m_i) = (n_j, m_j - 1) \rightarrow \Delta E_N^{(0)} = \hbar(\omega + \Omega)$, or
$(n_i, m_i) = (n_j - 1, m_j - 1) \rightarrow \Delta E_N^{(0)} = -\hbar(\omega - \Omega)$,
where $E_N^{(0)}$ denote the non-interacting energy contribution in Eq. (2.33).

  - $m_i > 0$

$$\langle \psi_i | \gamma_{x_0} | \psi_j \rangle = \hbar\omega \frac{\delta x_0}{\ell_{ho}} \frac{\delta_{m_i+1,m_j}}{2} \left(\sqrt{n_i + |m_i| + 1}\delta_{n_i,n_j} - \sqrt{n_i}\delta_{n_i,n_j+1} \right), \tag{A.21}$$

where the single-particle states that are connected are
$(n_i, m_i) = (n_j, m_j + 1) \rightarrow \Delta E_N^{(0)} = -\hbar(\omega + \Omega)$, or
$(n_i, m_i) = (n_j + 1, m_j) \rightarrow \Delta E_N^{(0)} = \hbar(\omega - \Omega)$.

Hence, we see that the transition matrix Γ_{x_0} of a perturbation of the trap center δx_0 can only change angular momentum by one unit $\Delta M = \pm 1$. If we consider a ground state, we see that Γ_{x_0} only connects to states $\Delta E^{(0)} = 2\hbar(\omega \mp \Omega)$.

A.4 Center-of-Mass Operator Matrix Elements

In this section, the results of the matrix elements of the single-particle center-of-mass operators $Q_\pm$ in Eq. (2.70) are stated. The $Q_\pm$ operators in occupation number representation are

$$Q_\pm = \sum_\sigma \sum_{i,j} \langle \psi_i | q_\pm | \psi_j \rangle c_{i\sigma}^\dagger c_{j\sigma}, \tag{A.22}$$

with single-particle matrix elements

$$\langle \psi_i | q_\pm | \psi_j \rangle = \frac{1}{\sqrt{2}} \int_0^{2\pi} d\varphi \int r dr \, \psi_i^*(r, \varphi) e^{\mp i\varphi} \left(\mp \frac{1}{r} \frac{\partial}{\partial \varphi} - i \left(\frac{\partial}{\partial r} + r \right) \right) \psi_j(r, \varphi). \tag{A.23}$$

From the $e^{\mp i\varphi}$ factor it can be seen that Q_+ only connect states with $m_i = m_j - 1$ and Q_- only states with $m_i = m_j + 1$. Below follow the analytical results for the single-particle matrix elements of Q_+:

- $\Delta M = -1$: the matrix elements depends on if $m_i \geq 0$ of $m_i < 0$.
  - $m_i \geq 0$

$$\langle \psi_i | q_+ | \psi_j \rangle = -i\delta_{m_i+1,m_j} \delta_{n_i,n_j} \sqrt{2(n_i + |m_i| + 1)}, \tag{A.24}$$

where we note that single-particle states that are connected are $(n_i, m_i) = (n_j, m_j - 1) \rightarrow \Delta E_N^{(0)} = -\hbar(\omega - \Omega)$,
where $E_N^{(0)}$ denote the non-interacting energy contribution in Eq. (2.33).

- $m_i < 0$

$$\langle \psi_i | q_+ | \psi_j \rangle = i\delta_{m_i+1,m_j}\delta_{n_i+1,n_j}\sqrt{2(n_i+1)}, \tag{A.25}$$

where the single-particle states that are connected are $(n_i, m_i) = (n_j - 1, m_j - 1) \rightarrow \Delta E_N^{(0)} = -\hbar(\omega - \Omega)$.

For Q_-, we have:

- $\Delta M = +1$: the matrix elements depends on if $m_i > 0$ of $m_i \leq 0$.
  - $m_i > 0$

$$\langle \psi_i | q_- | \psi_j \rangle = i\delta_{m_i-1,m_j}\delta_{n_i+1,n_j}\sqrt{2(n_i+1)}, \tag{A.26}$$

where we note that single-particle states that are connected are $(n_i, m_i) = (n_j - 1, m_j + 1) \rightarrow \Delta E_N^{(0)} = -\hbar(\omega + \Omega)$,
where $E_N^{(0)}$ denote the non-interacting energy contribution in Eq. (2.33).

  - $m_i \leq 0$

$$\langle \psi_i | q_- | \psi_j \rangle = -i\delta_{m_i-1,m_j}\delta_{n_i,n_j}\sqrt{2(n_i+|m_i|+1)}, \tag{A.27}$$

where the single-particle states that are connected are $(n_i, m_i) = (n_j - 1, m_j + 1) \rightarrow \Delta E_N^{(0)} = -\hbar(\omega + \Omega)$.

A.5 Breathing Mode Operator Matrix Elements

Here, the results of the matrix elements of the breathing operator L in Eq. (2.61) are stated, which to leading order in perturbation theory is a single-particle operator. The L operator in occupation number representation is

$$L = \sum_\sigma \sum_{i,j} \langle \psi_i | l | \psi_j \rangle c_{i\sigma}^\dagger c_{j\sigma}, \tag{A.28}$$

with single-particle matrix elements

$$\langle \psi_i | l | \psi_j \rangle = (\epsilon_i + \Omega m_i)\frac{\delta_{i,j}}{\hbar\omega} + \int_0^{2\pi} d\varphi \int r dr\, \psi_i^*(r,\varphi)\left(-1 - r\frac{\partial}{\partial r} - \frac{r^2}{\ell_{ho}^2}\right)\psi_j(r,\varphi), \tag{A.29}$$

where ϵ_i are single-particle energies in Eq. (2.13). The analytical result for the matrix elements is given below

$$\langle \psi_i | l | \psi_j \rangle = \delta_{m_i,m_j}\delta_{n_i+1,n_j}\left(2\sqrt{(n_i+1)(n_i+|m_i|+1)}\right), \tag{A.30}$$

from which it can be seen that the single-particle states that are connected are $(n_i, m_i) = (n_j - 1, m_j) \rightarrow \Delta E_N^{(0)} = -2\hbar\omega$. This means that L conserves angular momentum.

DEPARTMENT OF SOME SUBJECT OR TECHNOLOGY
CHALMERS UNIVERSITY OF TECHNOLOGY
Gothenburg, Sweden
www.chalmers.se

CHALMERS
UNIVERSITY OF TECHNOLOGY